Physicochemical Interactions at Interfaces: Mass and Charge Transfer at Chemically Reacting Interfaces

by

John R. Lake

B.A., Bowdoin College (2012)
B.S., Columbia University (2012)
S.M., Massachusetts Institute of Technology (2019)

Submitted to the Department of Mechanical Engineering
in Partial Fulfillment of the Requirements for the Degree of

Doctor of Philosophy in Mechanical Engineering

at the

MASSACHUSETTS INSTITUTE OF TECHNOLOGY

February 2023

Author: ……...……
Department of Mechanical Engineering
November 4, 2022

Certified by: ……
Kripa K. Varanasi
Professor of Mechanical Engineering
Thesis Supervisor

Accepted by: ……
Nicolas G. Hadjiconstantinou
Professor of Mechanical Engineering
Chairman, Committee on Graduate Studies

THIS PAGE INTENTIONALLY LEFT BLANK

Physicochemical Interactions at Interfaces:
Mass and Charge Transfer at Chemically Reacting Interfaces

by

John R. Lake

Submitted to the Department of Mechanical Engineering
on November 4, 2022 in Partial Fulfillment of the
Requirements for the Degree of

Doctor of Philosophy in Mechanical Engineering

ABSTRACT

Aqueous multiphase interfaces which undergo chemical reactions are crucial interfacial regions for most of human technology and are relevant for many large-scale industrial activities. Using rationally designed surfaces to enhance aqueous physicochemical interactions at these critical interfaces provides a unique approach to alleviate limitations for many applications. From this perspective, the thesis presented here includes four distinct studies which interrogate interfaces undergoing a chemical reaction, with a focus on understanding the mass or charge transfer occurring at these interfaces to enable more effective transport during these chemical reactions. First, the impacts that microscale texture have for gas evolving electrochemical electrodes is investigated to highlight the unique design considerations that exist for gas evolving electrochemical electrodes that are distinctly different than non-gas evolving electrochemical systems. Next, the inactivation of active surfaces by adhered gas bubbles is investigated for gas evolving electrochemical systems. In many industrially relevant scenarios, the passivating effect that adhered bubbles have on a process are detrimental to its efficiency and overall function. The findings presented are contrary to the current prevailing understanding, bringing important implications for the design of these systems in the future. Next, when gas bubbles are intended to react in bulk aqueous solutions, their tendency to minimize their surface energy has interesting consequences, relevant for a host of transport, absorption, and mineralization processes. A new method for the absorption of gas bubbles in liquid absorbents is presented using carbon dioxide gas absorption by an alkaline absorbent as a model system with applications for sustainability. Finally, a study is presented looking at the transient impacts of gas depletion in the electroreduction of carbon dioxide into useful products to better inform how these systems can limit the impacts caused by poor mass transport of the reactant gas to their reacting electrodes. Taken together, these studies aim to demonstrate how fundamental interfacial engineering principles can be applied to enhance a variety of chemical processes involving multiphase aqueous reactions. As a consequence of the prevalence of these interfaces, the work has wide-ranging relevance, ranging from power generation and chemical conversion to global decarbonization.

Thesis Supervisor: Kripa K. Varanasi
Title: Professor of Mechanical Engineering

THIS PAGE INTENTIONALLY LEFT BLANK

Acknowledgements

I would like to thank my advisor, Professor Kripa Varanasi, for continuously motivating me on all of my research projects included in this thesis, as well as the additional projects we worked on together that is not included here. His intellectual curiosity and willingness to explore new and exciting ideas make him an inspirational leader and wonderful mentor. Without his guidance, this work would not have been possible. Kripa, I will miss the time brainstorming all the wonderful and crazy ideas for experiments and possible projects on the whiteboard in your office. You cultivate such a great environment of discovery and pushing into new areas of research in your lab, which has made my time there so unique and gave me the opportunity to explore such a wide variety of exciting and interesting topics while under your guidance. Thank you for being the sensitive and supporting adviser that you are, and here's to hoping that we will be able to work together in the future.

I would like to thank my thesis committee members Professor T. Alan Hatton and Professor Alan Grodzinsky for their guidance, support and time over the past few years as part of my thesis committee. I had the pleasure of taking my first course at MIT with Professor Grodzinsky and was able to work on a sponsored research project under Professor Hatton's leadership, both of which are experiences I learned greatly from and will not forget. Thank you to you both for being such wonderful mentors, teachers and researchers for students like myself to look up to and respect.

A special thanks to those who specifically helped with the work included in this thesis. Thanks to Alvaro Moreno Soto for his help with Chapter 2 and for leading the efforts for the work included in Chapter 5. Thanks to Simon Rufer and the entire University of Chicago/Globus Labs team (Aristana Scourtas, Marcus Schwarting, Jim James, Nathan Pruyne, Aadit Ambadkar, Ian Foster, and Ben Blaiszik) who led the efforts in development of the bubble detection algorithm included in Chapter 3. Finally, thanks to Victor Leon for leading numerical modeling efforts, Tal Jospeh for assistance with experimental data collection, and Sami Khan for his initial guidance and experiments on the project related to the work presented in Chapter 4.

Many thanks to my other lab mates in the Varanasi Research Group who are always willing to help and have given me immense advice and feedback. My time in the research group have been an absolute pleasure, much of which is due to working with such a great group of people.

I would also like to thank all my previous academic and research mentors along my path to graduate school. Especially, thank you to Professor Bin Chen who gave me my first introduction to engineering research in her lab and whose support and guidance ignited my passion for working in a lab environment. Her creativity, kindness and fun-loving spirit made working in her lab a wonderful introduction to research and led me on the path to eventually end up where I am today. Additionally, a special thank you to Professor Warren Ruder who took a chance in hiring me to work in his research group during my career change from the consulting world where I worked for years after my undergraduate studies. Without his guidance and support, I am sure I would not have ended up at MIT for graduate school.

Thank you also to MIT nano and MTL staff who support the cleanroom and fabrication facilities on campus which were used for making many of the samples used for the work in this thesis.

I would like to also thank the research sponsors who funded the work presented in this thesis and the sponsors who helped to fund my graduate studies through fellowship awards. Thanks to Shell for their financial support and guidance of the work presented in Chapter 2 and Chapter 5, with a special thanks to Flávia Cassiola for her support and guidance managing the programs throughout the years. Thanks to US Department of Energy's Advanced Research Projects Agency - Energy (arpa-e), for their financial support of the work presented in Chapter 3. Finally, thanks to the National Science Foundation through the Graduate Research Program Fellowship (GRFP) and to the Shell-MIT Energy Fellowship through the MITei Energy Fellows Program for their financial support of my graduate studies during my time at MIT.

My parents, John and Sandy, have provided me with opportunities and support that have made my education possible and my life filled with love. All my academic achievement is dedicated to them. My sister Sarah has been my lifelong friend and provides me with constant encouragement. As has become evident, I owe my success to my family and could not have finished my doctoral studies if it were not for their constant support, especially through the final months which were particularly challenging. Also, thanks to my more recently added parents-in-law, Nancy and Howard, who have become a source of love and support and who I am grateful every day to have in my life.

Finally, thank you to my wife, Allie, for her support of my academic pursuits. Getting to become engaged, married, and parents together throughout my graduate work made the journey the most wonderful years of my life so far, although difficult at certain points. I could not have succeeded if it were not for you being with me every step of the way. I owe my happiness to you.

To my daughter, Harper, whose smile brightens all my days

THIS PAGE INTENTIONALLY LEFT BLANK

Contents

THIS PAGE INTENTIONALLY LEFT BLANK

List of Figures

List of Tables

THIS PAGE INTENTIONALLY LEFT BLANK

1. Introduction

1.1. Overview and Thesis Structure

Interfaces are everywhere and of great importance for determining the nature of physicochemical interactions occurring between phases. Indeed, most industrially relevant systems involve various forms of heat and mass transfer between phases. However, just as the interactions between phases can be used advantageously manipulated, many detrimental interfacial interactions can be difficult to suppress and cause inefficiencies for many industrial processes. This thesis aims to investigate a variety of interfacial engineering approaches to better understand how we can further mitigate some of these inefficiencies and to apply them to a number of applications across disciplines and industries. Summarized in Figure 1-1, four distinct research areas will be focused on as part of the thesis presented here: (1) Impact of Bubbles on

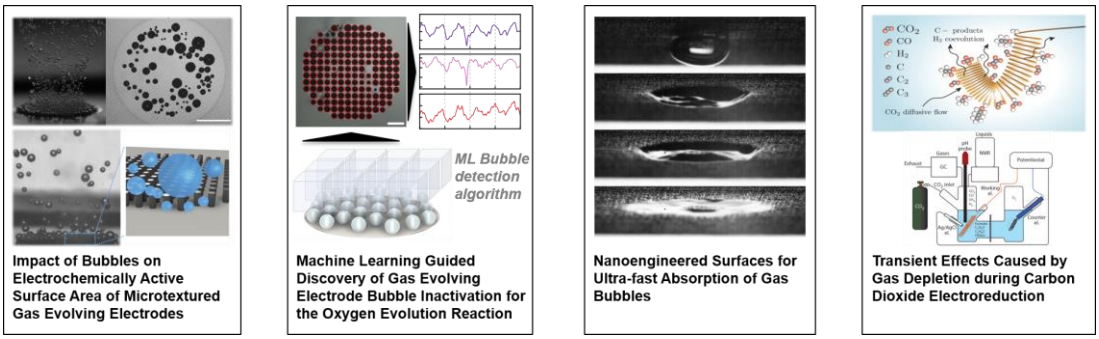

Figure 1-1. Graphical representation of the four chapters of this thesis related to, from left to right, (Chapter 2) Impacts of microtexture on the elecrochemically active surface area for gas evolvng electrodes, (Chapter 3) Understanding the degree of inactive caused by adhered bubbles on the surface of gas evolving electrodes during electrochemical reactions with the assistance of machine learning models for bubble detection, (Chapter 4) Surface enhanced direct injection of gas into nanotextured capture surfaces to enhance the chemical absorption of that gas in the surrounding liquid absorbent, and (Chapter 5) Studying and modeling the impacts of gas depletion around the electrode interface during the electroreduction of carbon dioxide to useful products.

Electrochemically Active Surface Area of Microtextured Gas Evolving Electrodes, (2) Machine Learning Guided Discovery of Gas Evolving Electrode Bubble Inactivation, (3) Nanoengineered

Surfaces for Ultra-fast Absorption of Gas Bubbles, and (4) Transient Effects Caused by Gas Depletion during Carbon Dioxide Electroreduction.

However, while being distinct, these four research topics can be categorized into an overarching thematic grouping due to their being focused on the interfacial mass and charge transport occurring at a chemically reacting interface. Further, there are three particular themes that can subcategorize certain subsets of these research topics further: (1) Electrochemical Bubble Impacts, (2) Bubble/Surface Interactions during a Chemical Reaction, and (3) Carbon Dioxide Mitigation and Storage Solutions.

Falling into the first thematic category are the studies presented in Chapter 2 and Chapter 3. Chapter 2 examines the impact that bubbles have on the active surface area of a microtextured electrode's surface. A common technique in electrochemical system design is to increase the specific surface area of the active material on the electrode's surface to allow for higher activity for an electrode of the same geometric area. However, when gas is rapidly evolved from the electrode's surface, for example during the hydrogen evolution reaction, there becomes an interesting tradeoff between whether that added active surface area from increasing the roughness of the electrode is being effectively utilized or whether the inactivating effects of bubbles negate those benefits. Chapter 3 extends this view to a more fundamental level to empirically investigate the nature of bubble inactivation of a gas evolving electrochemical electrode's surface. While decades of research exist that has laid a great foundation for our understanding of how bubbles inactive the electrode while they are adhered, little empirical evidence has been used to support the prevailing theory currently accepted, which guides the development and design of gas evolving electrochemical systems. In Chapter 3, aided by developed machine learning tools to accurately

and effectively detect adhered bubbles on the electrodes tested, we aim to examine whether these currently held assumptions can be validated experimentally.

The next thematic category of bubble/surface interactions where a chemical reaction is taking place also include both Chapter 2 and Chapter 3, but also now include the next chapter, Chapter 4. Chapter 4 focuses now instead on the thermochemical reaction of the absorption of gas bubbles into a readily reacting liquid absorbent surrounding that gas. The absorption of gas by a liquid absorbent is a commonly used chemical engineering unit operation for separations in a wide variety of industrial settings. Especially with today's focus for scientists and engineers to develop technologies that can aid in the mitigation of climate change, sustainable solutions around the absorption of carbon dioxide are especially important. As a result, the model system studied in Chapter 4 is the absorption of carbon dioxide using a moderately alkaline hydroxide solution to produce a carbonate mineral product. While absorber units today are highly optimized and extremely efficient, they are not well-suited for the small scale, modular types of absorbers which might become required to absorb carbon dioxide from distributed or diffuse sources in a net-negative carbon emissions, sustainable future. As a result, this chapter focuses on the introduction, characterization and demonstration of a newly developed method for using engineered surfaces to enhance the absorption of a gas in a liquid absorbent which is simple to implement and is well-suited to scaling down to small sizes while maintaining high performance.

Finally, the third thematic category of carbon dioxide mitigation and storage solutions also includes the work from Chapter 4, given the focus on carbon dioxide absorption, but also includes the final chapter, Chapter 5. This final chapter characterizes empirically and analytically the depletion effects that occur proximally to the electrode's surface during carbon dioxide's electroreduction into useful products, like ethanol, methanol or ethylene to name a few. The

availability for the reactant carbon dioxide gas to be readily available at the electrode's surface has important implications for the selectivity and achievable reaction rates that can be attained for these electrochemical systems for any electrocatalyst material that is being used. As a result, the mass transport issues that are investigated and modeled here are not solely relevant for the specific electrode materials or cell configuration tested, but generally an important consideration for any carbon dioxide electroreduction system.

To accomplish the stated goals of these four chapters, a broad range of experimental techniques will need to be used, as the work is interdisciplinary in scope. While the research areas and relevant applications may seem too wide-ranging to be solved by using similar interfacial engineering approaches, that is the goal of this work. By focusing on these research areas, this thesis aims to provide new modalities for improving the specific systems investigated here. However, the approaches and solutions planned are likely useful in a wide array of applications and for specific systems beyond those investigated here.

The thesis is organized into separate chapters for each of the four research topics summarized in Figure 1-1. Each chapter follows a similar structure, first introducing a summary of the concept to be explored and including a high-level summary of the work's results. Next, the topic and its motivations for real world applications are introduced, followed by the experimental summary for data collection and analysis, followed by a detailed summary of the results and conclusions for each work. Finally, the thesis ends with a summary of the most important contributions from each of the four research topic chapters and concluding remarks regarding proposed work to be conducted in the future to follow-on from the progress presented here.

1.2. Summary of Contributions

The contributions from this thesis are organized by each chapter, and the corresponding journal article that has been published, or the corresponding manuscripts that are in preparation for submission to be considered for publication in the near future:

Chapter 2:

- **Jack R. Lake**, Álvaro Moreno Soto, and Kripa K. Varanasi. Impact of Bubbles on Electrochemically Active Surface Area of Microtextured Gas-Evolving Electrodes. *Langmuir* 2022 38 (10), 3276-3283. DOI: 10.1021/acs.langmuir.2c00035

Chapter 3:

- **Jack R. Lake** †, Simon Rufer †, Aristana Scourtas, Marcus Schwarting, Jim James, Nathan Pruyne, Aadit Ambadkar, Ian Foster, Ben Blaiszik, Kripa K. Varanasi. Machine Learning Guided Discovery of Gas Evolving Electrode Bubble Inactivation for the Oxygen Evolution Reaction. (*In Preparation*)

Chapter 4:

- **Jack R. Lake** †, Victor Julio Leon †, Tal Joseph, Sami Khan, Kripa K. Varanasi. Ultra-fast Absorption of Carbon Dioxide Gas Bubbles using Nanoengineered Capture Surfaces. (*In Preparation*)

Chapter 5:

- Álvaro Moreno Soto, **Jack R. Lake**, and Kripa K. Varanasi. Transient Effects Caused by Gas Depletion during Carbon Dioxide Electroreduction. *Langmuir* 2022 38 (3), 1020-1033. DOI: 10.1021/acs.langmuir.1c02540

† *Authors contributed equally*

THIS PAGE INTENTIONALLY LEFT BLANK

2. Impact of Bubbles on Electrochemically Active Surface Area of Microtextured Gas Evolving Electrodes

2.1. Summary of Concept and Contributions

The adverse effects of electrochemical bubbles on the performance of gas-evolving electrodes have been extensively studied. However, the ways in which bubbles dynamically alter the electrochemically active surface area during bubble evolution is not well understood. Here, we study hydrogen evolution at industrially-relevant current densities by using controlled microtexture to examine this fundamental relationship. Surprisingly, the most densely microtextured electrodes have the lowest performance on an active surface area basis. Using high-speed imaging we show that the benefits of microtexture to release smaller bubbles more consistently is outweighed by the inactivation induced by bubbles growing within the denser microtexture, causing these performance limitations. Additionally, we show that the area beneath adhered bubbles is electrochemically active, contrary to currently held assumptions. Our study therefore has broad implications for electrode design to avoid ineffective use of precious catalyst materials, which is especially critical for porous electrodes and three-dimensional structures with high-specific surface areas.

2.2. Introduction

The adverse effects of electrochemical bubbles on the performance of gas-evolving electrodes have been extensively studied. However, the ways in which bubbles dynamically alter the electrochemically active surface area during bubble evolution is not well understood. Here, we study hydrogen evolution at industrially-relevant current densities by using controlled microtexture to examine this fundamental relationship. Surprisingly, the most densely microtextured electrodes have the lowest performance on an active surface area basis. Using high-speed imaging we show that the benefits of microtexture to release smaller bubbles more consistently is outweighed by the inactivation induced by bubbles growing within the denser microtexture, causing these performance limitations. Additionally, we show that the area beneath adhered bubbles is electrochemically active, contrary to currently held assumptions. Our study therefore has broad implications for electrode design to avoid ineffective use of precious catalyst materials, which is especially critical for porous electrodes and three-dimensional structures with high-specific surface areas.

Electrochemical gas-evolving electrodes (GEEs) are important for many industrial applications. As electrochemical bubbles nucleate, grow and eventually detach, they cause ohmic and activation losses when directly and indirectly inactivating active catalyst area, while also causing concentration variability proximal to the electrode surface. One of the largest GEE applications is the chlor-alkali process, used for chlorine gas production and accounting for approximately 2% of electricity usage in the United States annually[1]. Approximately 20% of total chlor-alkali cell voltage is attributable to bubbles[2]. Another widely researched GEE application is water electrolysis, which is the focus of experiments included here. Significant effort continues to focus on improving electrocatalyst materials for the hydrogen evolution reaction (HER)[3–5] and

oxygen evolution reaction (OER)[6,7] to improve reaction efficiency, in some cases with an explicit focus on advantageous bubble release[8,9]. However, the overpotentials caused by these intentionally generated bubbles are not inherently related to the electrocatalytic properties of the active material. Rather, they are an inevitable consequence for GEEs constructed from materials to which evolved bubbles will adhere.

The effects of electrochemical bubbles have been studied both theoretically and experimentally for decades[10–16]. Recent works have summarized current progress, along with methods for the mitigation of adhered bubbles on electrodes[2,17]. Studies range widely in their focus including the impacts of concentration overpotential[18], bubble nucleation away from the GEE active surface[19], bubble growth on hydrophobic electrodes[20] and isolated microstructures[21,22], bubble nucleation models[23], bubble manipulation via capillarity[24], and surface tension gradient-driven flows[25,26]. Active methods to enhance the departure of bubbles by using ultrasonic[27] and magnetic[28,29] fields have also been proposed. Finally, electrodes of various functional forms have been investigated. For example, a number of studies focus on gas evolution specifically for microelectrodes in a wide range of conditions[30–34], including different pH conditions, varying levels of surfactants, as well as in microgravity environments.

The impact that surface roughness and wettability have on GEE performance is particularly relevant. Prior work has modulated GEE wettability by hydrophobic modifier addition for micropatterned[35] and porous foams[36]. Additionally, studies using high aspect ratio microwires have shown to assist with bubble release for both water electrolysis and CO_2 electroreduction photoelectrochemical systems[37–39]. However, the fundamental link between increasing active surface area and electrochemically active surface area (ECSA)-normalized performance in the presence of bubble inactivation is relatively unknown. Assuming that the active catalyst will be

uniformly loaded on a GEE, there is an intrinsic and proportional link between its surface morphology and ECSA. In non-gas evolving electrochemical systems, advantages of high specific surface area materials have been widely demonstrated, as in batteries[40] or supercapacitors[41–43]. However, high specific area is likely not advantageous for gas-evolving systems to the same extent due to the inactivating effect of bubbles. The seemingly trivial connection between microscale roughness and ECSA has important consequences which would create a unique design space for surface engineering GEEs. The surface morphology of a GEE and its active catalyst loading tend to be intrinsically linked, especially for applications using porous, high surface area electrodes. Therefore, it is essential to ensure that bubble inactivation of the typically precious active material is minimized for any given GEE architecture to achieve maximum system performance. Here, we systematically study the impact that bubbles have on dynamically altering electrochemically active surface area during gas evolution microtextured electrodes. To do so, we vary the microtexture in a controlled way by changing the density of micropost arrays by systematically varying the spacing between adjacent posts. Additionally, microposts allow for the formation of a discontinuous contact line[44], thereby allowing for changes in bubble pinning on these microtextures. The high degree of control and repeatability offered by using this approach makes it an ideal way to understand the way that changing the microtexture of a GEE changes the ways that electrochemical bubbles impact GEE performance.

2.3. Experimental Methods

2.3.1. Measuring Impact of Adhered Electrochemical Bubbles

An electrochemical cell was fabricated for experiments to observe bubble evolution on working electrodes (Figure 2-1A). The model electrochemical reaction used throughout this work is Pt-catalyzed HER in an acidic electrolyte of 0.5M H_2SO_4 (see Appendix §7.1.2). A Pt catalyst was chosen as it is widely studied, well-characterized and stable, avoiding any complications that could arise from using a novel, less well-understood catalyst. A circular active Pt area 3 mm in diameter was patterned, surrounded by an inactive region of silicon nitride (Figure 2-1B). In all experiments, quiescent electrolyte in a horizontal cell was used. This allowed bubble/surface interactions to occur without externally-driven fluid flow, having most of the electrolyte flow resulting from the bubbles' motion. The velocities of typical bubbles released from the surface ranged between ~1 mm/s for the smallest bubbles just released from the electrode's surface and ~5 cm/s for larger bubbles which had risen roughly ~3 mm from the electrode's surface, as determined using high-speed imaging. The focus of this study is on current density operation between 100 and 400 mA/cm^2 on a geometric basis, in the range of current commercial alkaline water electrolyzer operation[45] where bubble effects are industrially significant. At this high activity, the lifetime of bubbles on the electrode surface before departing or interacting with neighboring bubbles can be on the order of milliseconds, requiring high-speed imaging techniques to properly characterize their dynamics. High-speed imaging from both a top-down and side profile were performed to analyze the dynamics of bubble/electrode interactions (Figure 2-1C).

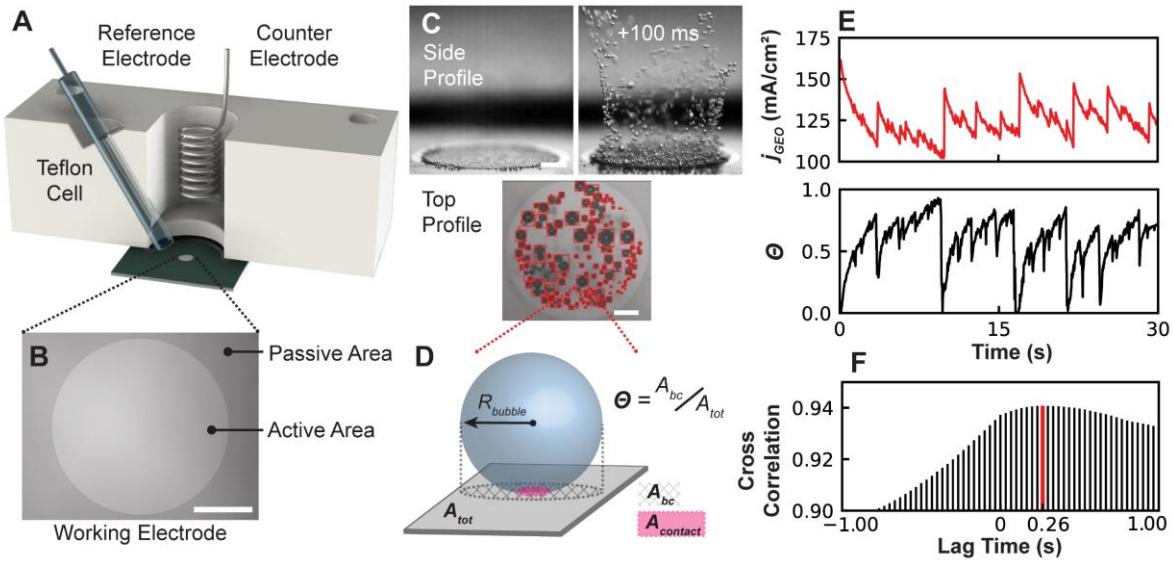

Figure 2-1. Experimental setup and the impact of adhered bubbles on gas-evolving electrodes. (A) Electrochemical setup used to probe impacts of adhered hydrogen bubbles on Pt electrode. (B) Microscope image of working electrode's active Pt area where the reaction occurs and inactivated surroundings where it does not. Scale bar is 1 mm. (C) Side and top profile imaging of bubble evolution of working electrode. Top shows high-speed side profile imaging of bubble evolution, bottom shows a processed image used to analyze metrics of adhered bubbles. Scale bars are 500 μm. (D) Adhered bubble on a surface defining the bubble coverage, Θ, as the fraction of area shadowed by adhered gas bubbles, A_{bc}, to the total surface area, A_{tot}. Also, the contact area where the bubble is in direct contact with the electrode is shown as $A_{contact}$. (E) Time series of the working electrode's current density and bubble coverage as a function of time. (F) Quantifying the similarity between current and bubble coverage signals, cross-correlation shows maximum correlation when the current signal lags the bubble coverage signal by 0.26 s. Sampling rate for this experiment matched to frame rate of image capture (30 fps).

2.4. Results and Discussion

The bubble coverage, θ, is a commonly used parameter for characterizing a GEE[46], defined as the ratio of the total shadowed area of an adhered bubble, the bubble coverage area A_{bc}, and the total area, A_{tot}, $\theta = {A_{bc}}/{A_{tot}}$ (Figure 2-1D). Using this setup, we measured the evolution of the bubble coverage while the working electrode was polarized. Figure 2-1E shows representative chronoamperometric data collected for a sample fabricated using a shadow mask for patterning the active area (see Appendix §7.1.3). From Figure 2-1E, it is visually apparent that as the bubble coverage increases due to a larger fraction of the surface being covered by adhered bubbles, the current density decreases. Eventually, when the bubble coverage drastically falls due to the departure of large bubbles from its surface, the current quickly recovers, and this process repeats over time. Thus, a causal relationship between adhered bubbles and the negative effects they cause for the current density of a GEE was demonstrated. Using cross-correlation analysis, we found that the measured bubble coverage and current signals are maximally correlated when the current lags the bubble coverage signal by 0.26 s, with a cross-correlation value of approximately 0.94 (Figure 2-1F). Cross-correlation analysis was performed in Python using the matplotlib[47] library's *xcorr()* function and normalizing both the current and bubble coverage signals and correlating after shifting the signals up to 1 second relative to one another over 30 discrete lag time steps in either direction. This result highlights that the measured current and bubble coverage are highly correlated, and that changes in the bubble coverage lag behind the current signal, by approximately 0.26 s. Physically, this makes sense, as the mass transport impact from the departure of a bubble will take some discrete amount of time to be realized at the electrode surface, as the bubble will disrupt the diffusion boundary layer in its vicinity and induce convective flows during its

departure. Given the clear link between bubble accumulation on the surface of electrodes and performance, we aimed next to systematically modulate ECSA by microtexturing the active Pt area with micropost arrays. We hypothesized that electrodes operating at industrially relevant current densities could become flooded at high microtexture densities, thus negating the intended benefit of the additional active surface area.

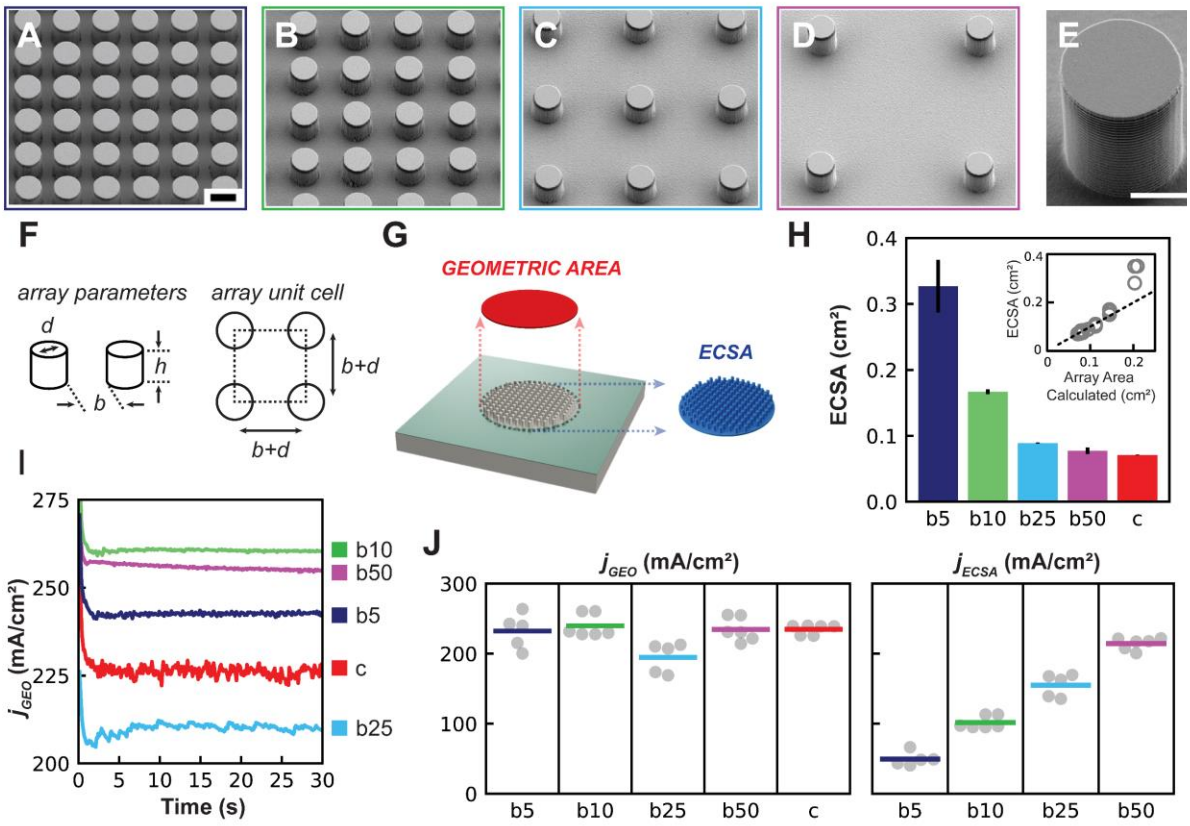

Figure 2-2. Systematic investigation of the impacts of microtexture on gas-evolving electrode performance. (A-D) SEM images of Pt-coated micropost arrays of 10 µm height and diameter, with spacing of 5, 10, 25, and 50 µm, labeled as 'b5', 'b10', 'b25', and 'b50' respectively. Scale bar is 10 µm. (E) SEM image of a single micropost. Scale bar is 5 µm. (F) Array parameter and unit cell schematic. (G) Graphical definitions of geometric and ECSA surface areas for current density determinations. (H) UPHD-derived ECSA measurements for b5, b10, b25, b50, and an untextured control, labeled 'c'. Error bars show standard deviation. Inset shows measured ECSA as a function of idealized array area calculation. (I) Chronoamperometry data for tested samples showing the current as a function of time. (J) Summary of chronoamperometry results for tested electrodes showing average geometric and ECSA normalized current densities for final 20 s of chronoamperometry trials. Each point represents an individual trial's average, while lines represent the average across all trials for a given array group. Chronoamperometry results shown for applied potential of 0.35 V vs. Ag/AgCl reference electrode.

2.4.1. Performance of Microtextured Pt Electrodes

To ensure a high degree of control of active surface area and geometry, Pt working electrodes were patterned using photolithography (see §0). Micropost arrays of regular spacings (Figure 2-2A-E) were used to control the microtexture, and thus ECSA, of fabricated electrodes. Using this approach, we initially set the micropost diameter, *d*, and height, *h*, to 10 μm, while varying the spacing between adjacent posts, *b*, to 5, 10, 25, and 50 μm, labeled as *b5*, *b10*, *b25* and *b50*, respectively. These array parameters are defined graphically in Figure 2-2F. Chronoamperometry was used to compare the average current densities for different electrodes at a constant applied potential. These current densities can be determined using either the geometric area of the electrode's projected area, or the ECSA Figure 2-2G). Underpotential hydrogen deposition (UPHD) was used to measure ECSA for all electrodes, (Figure 2-2H) (see §0). It is interesting to note that *b50*, *b25* and *b10* electrodes' areas align closely with the array surface area that can be simply calculated from the array parameter geometry. Only *b5* electrodes, which have the majority of their ECSA derived from the lateral sides of microposts, show a higher ECSA than predicted by the array surface area calculation. This can be rationalized by the fact that these lateral micropost sides have been roughened via the etching process, which adds more surface area than idealized by the array surface area calculation and can be accurately captured using UPHD measurements (see Appendix §7.1.2).

Chronoamperometric tests using an applied potential of 350 mV vs. Ag/AgCl were then conducted. There is no clear trend to favor higher geometric current densities for electrodes of larger ECSA (Figure 2-2I). If all electrodes performed with comparable ECSA-normalized current density, we would expect *b5* electrodes to output more than 4 times the geometric current density than the untextured control surface. Unexpectedly, the geometric current densities for all micropost

arrays and the untextured sample tended to be quite similar (Figure 2-2J). For example, although a *b5* electrode has an ECSA more than four times that of the smooth control, the average geometric current densities for both electrodes differ by less than 2% different. ECSA-normalized current densities precipitously fall away from the control surface as the microarray spacing decreases (Figure 2-2J). While the ECSA measured in the absence of bubbles using UPHD is significantly larger than the control for *b5* or *b10* electrodes, this result suggests that a larger relative portion of these higher ECSA electrodes is being inactivated by bubbles. As more microtexture is packed into a given geometric electrode area, evolved bubbles dynamically alter the active area available to react, limiting performance. To further rationalize these findings, we next investigated how bubbles interacted with the different electrodes in these tests.

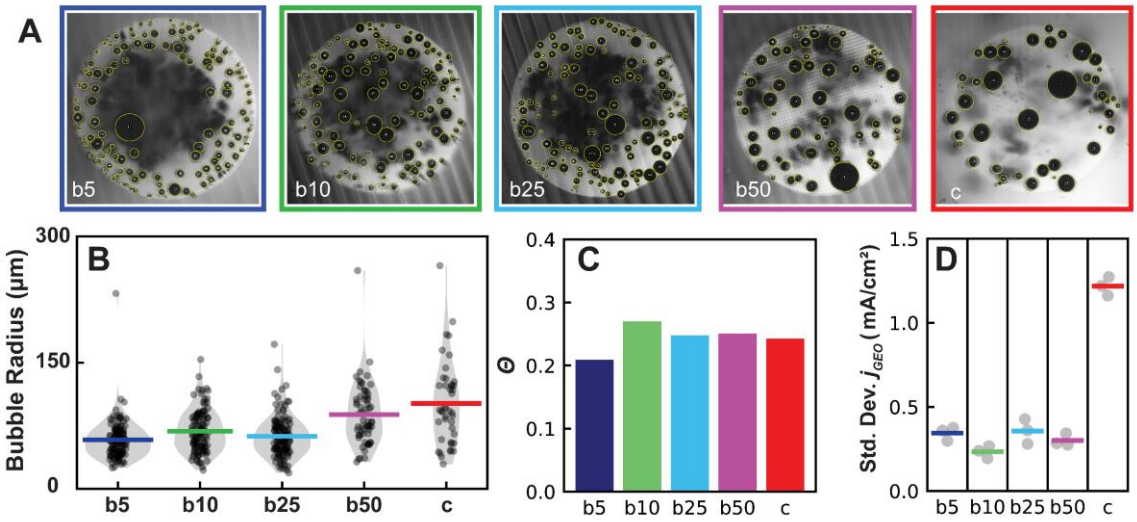

Figure 2-3. Bubble size and coverage analysis using high speed imaging. (A) High speed images acquired at 500 fps for each electrode tested. (B) Bubble sizes analyzed for the images shown in A. Individual bubbles are shown by each marker, approximated distributions shown in gray, and colored lines show the average bubble size. (C) Bubble coverages analyzed for the images shown in A. (D) Variation in current from the mean shown as the mean standard deviation of the geometric current densities for each microarray group. Data shown from chronoamperometry experiments using an applied potential of 0.35 V vs. Ag/AgCl reference electrode.

High-speed imaging from a top view was then utilized to measure bubble size and coverage metrics for the microarray electrodes and untextured control. As shown visually in Figure 2-3A, moving from the untextured control to the more densely microtextured electrodes, we see that the distribution of the number and size of bubbles shift noticeably. First, electrode-adhered bubbles decreased in size on average by almost a factor of 2 for b5, b10 and b25 microtextured samples relative to the control (Figure 2-3B). Although the distribution of bubbles is much more highly concentrated around the mean for the *b5*, *b10* and *b25* microtextured electrodes, a larger number of smaller bubbles persisted at any given time, causing bubble coverage to remain relatively similar for all the electrodes tested, remaining between 0.21 and 0.27 Figure 2-3C). Finally, while bubble coverage remained similar, the more effective shedding of smaller bubbles from microtextured electrodes provided the benefit of minimizing fluctuations of current on the electrode's surface caused by the growth and departure of large adhered bubbles (Figure 2-3D). Both the nature of the contact line for an individual bubble and its interactions with neighboring bubbles will influence its departure. As a result, the combined effect of constraining the contact line to the tops of posts, and promoting coalescence between neighboring bubbles allows for the moderately and highly microtextured *b5*, *b10* and *b25* electrodes to release smaller bubbles more consistently than the untextured control and sparsely textured *b50* electrodes. Taken together, we show that both improved bubble release and more stable current signals are achieved using microtextured array electrodes. However, from an ECSA-normalized standpoint, the higher catalyst loading for these samples is not as effectively utilized as is the case for the untextured control electrode.

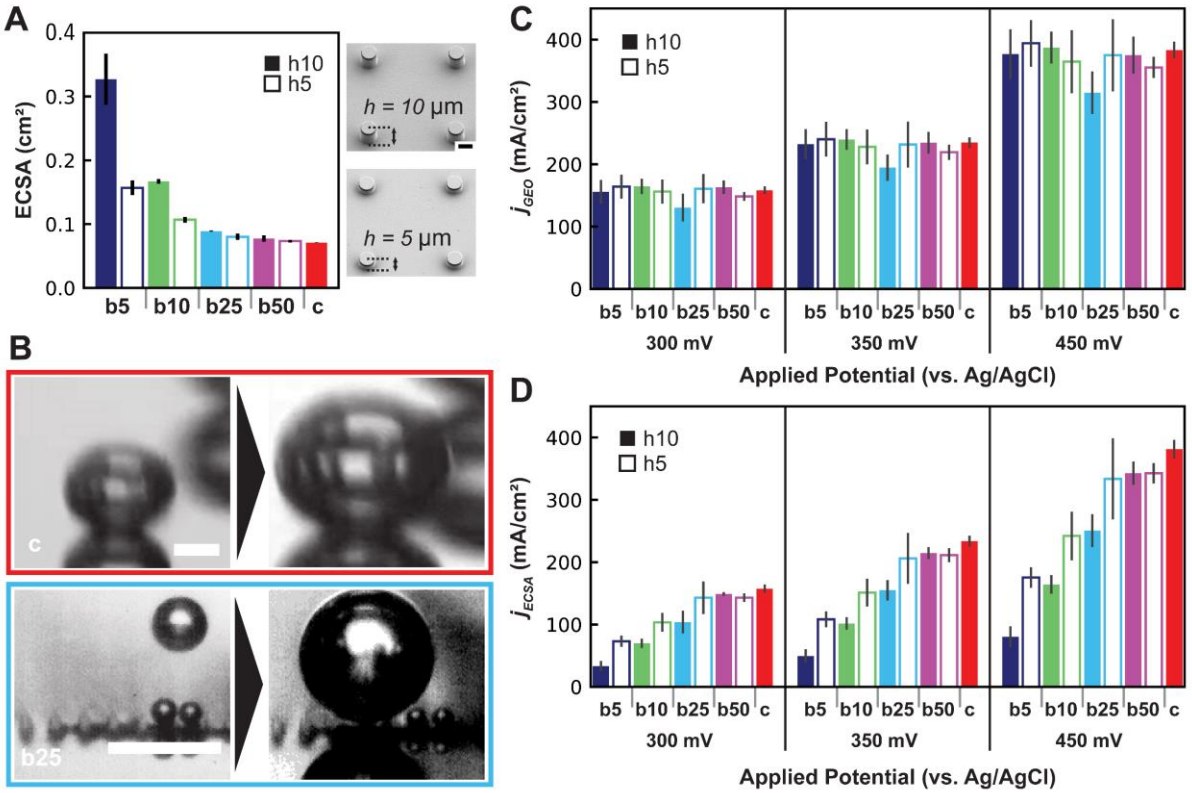

Figure 2-4. Investigation of improving highly microtextured electrode performance by decreasing the microarray height. (A) ECSA summary showing the decrease in ECSA for the micropost arrays of shorter height for all spacings. At right, SEM images of previously analyzed microposts of *h*=10 µm and half-height arrays now of *h*=5 µm. (B) Side-profile images showing bubbles on the untextured control surface (top) and on a b25 microtextured sample (bottom) at two time points. Scale bars are 100 µm. (C) Geometric and (D) ECSA-normalized current density comparisons with side-by-side comparisons of posts of both heights at different applied potentials. Error bars show standard deviation.

2.4.2. Improving ECSA-normalized Performance

We next tested the hypothesis that ECSA-normalized performance could be recovered for microtextured surfaces by decreasing their roughness. To test this, we fabricated additional microarray samples, but now with half the height of previous samples, setting the height *h* to 5 μm instead of 10 μm. From an active area perspective, the differences in *b50* and *b25* posts of the full and half-height microarrays will not be significant, as those samples have only a nominal increase of roughly 5% and 25% in ECSA relative to an untextured surface, respectively. However, the differences in ECSA for the *b5* and *b10* microposts of full and half-height are more significant. In fact, for *b5* full height microarrays the majority of their ECSA is provided by the lateral, etched sides of the densely packed microposts. These geometric factors were confirmed by UPHD ECSA-measurements of the half-height microarray electrodes (Figure 2-4A). Surprisingly, upon repeating sets of chronoamperometry measurements, the geometrically-normalized current densities of half-height posts were quite similar, *if not slightly improved in some cases*, to their full height counterparts (Figure 2-4C). As a result, the average ECSA-normalized current densities for *b5*, *b10* and *b25* microarrays increased by approximately 119%, 48% and 35%, respectively (Figure 2-4D). Interestingly, these relative increases in ECSA-normalized current densities for half-height microarrays compared to full-height arrays were roughly equivalent across the three different applied potentials tested. This provides further evidence to suggest that a portion of active surface area was inactivated by the vigorous gas evolution for the full-height *b5*, *b10* and *b25* microarray samples. However, at sparse enough microtexture, confinement of gas and this inactivating effect was localized such that ECSA-normalized performance remained effectively equal, as shown by comparing full- and half-height *b50* electrodes in Figure 2-4D.

Although our untextured control surfaces performed with high ECSA-normalized current densities, the use of such electrodes is industrially impractical. Highly smooth electrodes, like those tested here, are not practical as an electrolyzer electrode material from a cost perspective and are difficult to manufacture and maintain. Generally, minimizing an electrode's physical size will lower the capital costs associated with its fabrication and installation, so maximizing the ECSA for a given geometric area is industrially advantageous. In our untextured electrode tests, these ultra-smooth surfaces create a low-hysteresis surface, as evident from the dynamics of their contact lines. Using high-speed imaging, we can visualize the distinct differences in the bubble/surface interactions and how the contact line evolves on a smooth electrode in comparison with a microtexture one (Figure 2-4B). For the control surface, adhered bubbles' contact lines are free to advance at a constant contact angle on the untextured Pt electrodes, as the contact line has no features or defects onto which to pin. The microtextured electrodes on the other hand exhibit distinctly different features due to their morphology. First, the etched microposts provide roughened surfaces for bubbles to preferentially nucleate. As these bubbles grow, their contact lines are pinned and constrained to the micropost tops (Figure 2-4B). Next, as coalescence appears to be the primary mode for the departure of small adhered bubbles, when bubbles pinned to adjacent microposts grow large enough such that they interact and coalesce, the freeing of energy as a result of lowering the pair of bubbles' surface energy is transferred to potential energy in the form of a 'jump.' This has been studied in the case of coalescing droplets on non-wetting surfaces[48–50] as well as in diffusively growing bubbles[51]. Here we observed this mode of bubble release in high-speed, showing that coalescence is an effective mode for small bubbles to detach from the electrode. Side profile images of bubble growth motivated the final analysis, which focused on interrogating the activity beneath adhered bubbles.

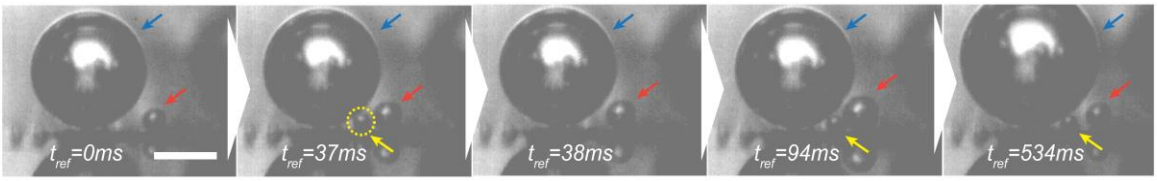

Figure 2-5. Timelapse images showing the evolution of a group of nucleation sites where bubbles grow on the microarray during the experiment. Yellow arrows designate a rapidly growing and coalescing bubble site (one such bubble circled in yellow in the second frame), directly underneath a large pinned bubble, designated by the blue arrow. Red arrows designate a moderate lifetime bubble site, less frequently undergoing coalescence with the large pinned bubble. Scale bar is 50 µm.

2.4.3. Activity of Electrodes Beneath Adhered Gas Bubbles

By imaging regions proximal to bubble nucleation sites, we were able to observe the interactions of bubbles evolving beneath other larger adhered bubbles on the electrode's surface (Figure 2-5). Coalescence can provide for enhanced bubble departure of neighboring, small bubbles of comparable size. However, in our study, we observed persistently adhered, larger bubbles which grew by coalescence through capturing smaller 'feeder' bubbles. In these situations, the asymmetry of bubble sizes changes how capillary waves propagate. The result is that smaller bubbles with larger Laplace pressures will merge into the larger bubble, consistent with prior work[51].

Bubble growth beneath larger adhered bubbles was imaged for multiple nucleation sites at high-speed and high-magnification. Figure 2-5 shows an evolution for a representative group of proximal nucleation sites on a *b25* microtextured electrode. We observed the evolution of an active bubble nucleation site beneath a large, persistently adhered bubble, labeled using colored arrows in Figure 2-5. Using scaling, we can estimate a characteristic timescale, t_{diff}, for hydrogen to diffuse beneath the bubble as $t_{diff} \sim \frac{R^2}{D}$, where R is the radius of the large, adhered bubble, shadowing the smaller rapidly nucleating bubble beneath, and D is the diffusivity of hydrogen gas in the electrolyte[52]. For this specific case, $R \approx 50\,\mu m$ and $D \approx 1x10^{-9}$ m^2/s. From this, we computed t_{diff} for hydrogen gas to diffuse this distance is on the order of 1 s. As demonstrated in Figure 2-5, bubbles grow on the small shadowed nucleation site to ~10 μm in radius over an average time ~52 ms. From this estimate, it is unlikely that the growth of these small bubbles can be solely attributed to diffusion from hydrogen gas generated away from beneath this large adhered bubble, as the growth occurs on a timescale more than an order of magnitude less than the diffusion

timescale in this case. Instead, the electrode beneath the large adhered bubble must be active enough to produce the hydrogen that is growing this small bubble rapidly and consistently in time. This finding provides new insights on activity proximal to an adhered bubble, and is contrary to current assumptions that the bubble coverage area has sufficiently low activity to accurately consider it inactivated[53]. As many bubble coverage related studies have used this assumption to define and characterize empirical relationships for a wide range of operating conditions[46,53–55], it is of interest to reexamine how this metric could be updated.

As a result, we propose an alternative measure of the dynamic ECSA that exists for a GEE during bubble evolution. We introduce the concept of a Bubble-induced Electrochemically Active Surface Area (BECSA) in the hopes that further research can elucidate a more rigorous quantification of this metric. Clearly, the area directly contacted by adhered bubbles is not capable of ion or electron transfer. However, it appears that the activity proximal to adhered gas bubbles is not well understood. Thus, the quantification and explicit definition of BECSA as a function of the adhered bubble parameters, and possibly other factors, warrants additional investigation. At present, we can constrain the BECSA definition to exist between the limits of the area inactivated by direct contact of gas and the bubble coverage area, as defined earlier in Figure 1D. While bubble coverage is a straightforward metric to measure and significant work exists based upon it, it is limited in its accuracy by assuming the area beneath a bubble is entirely inactive. This limitation will only become greater in the case of micro- or nanotextured GEEs, as bubbles can inactivate these GEEs to a greater relative degree than a smooth electrode as demonstrated in these experiments.

Beyond water electrolysis, the concept of BECSA is relevant for any gas-evolving reaction. From a sustainable energy perspective, investigations into this concept and efficient management

of evolved gas products will also be of critical importance for CO_2 electroreduction systems. An interesting design space emerges where microtexture might be used to attain the benefits observed of bubble release, while maintaining high BECSA-normalized performance. However, extremely porous GEEs will likely require additional gas management to mitigate inactivation of catalyst area using alternative approaches.

2.5. Conclusions

In summary, we have systematically studied the dynamic relationship between active area and ECSA-normalized performance by using microtextured Pt hydrogen-evolving electrodes. While pristinely smooth electrodes show high ECSA-normalized performance, the ability to release smaller bubbles, primarily by controlling nucleation site location and promoting coalescence-induced bubble release allows microtextured electrodes to avoid large current fluctuations and remain stable. Most interestingly, we found that a 2-fold reduction of microtexture height led to a 2-fold improvement in ECSA-normalized performance, indicative of inactivation of added active area by evolved bubbles. This finding can serve to improve GEE design by optimizing surface morphology to retain the benefits of microtexture, while avoiding ineffective use of additional active material that will become inactivated during bubble evolution. Finally, we provide empirical evidence that electrochemical activity below adhered hydrogen bubbles was not negligibly small, and contributed to the growth of shadowing larger bubbles. This suggests that certain widely held assumptions regarding this fact warrant revisiting from both an experimental and theoretical standpoint.

THIS PAGE INTENTIONALLY LEFT BLANK

3. Machine Learning Guided Discovery of Gas Evolving Electrode Bubble Inactivation

3.1. Summary of Concept and Contributions

While the adverse effects caused by electrochemical bubbles on the performance of gas-evolving electrodes has been extensively studied, studies on the degree adhered bubble caused inactivation is limited. Additionally, the ways in which bubbles dynamically inactivate electrochemically active surface area during bubble evolution has not been thoroughly experimentally validated. Here, we study the inactivation of electrodes caused by oxygen evolution while combining machine learning approaches to analyze bubble data and surface engineering to control the nature of bubbles' interactions with the electrode. In examining this fundamental relationship, the nature of bubble inactivation of an electrode's surface appears more dependent on the contact area of adhered bubbles, rather than their bubble coverage area as is currently believed. Using image-based bubble detection, we show that impacts of bubble coverage are quite small for surface engineered electrodes which promote high bubble coverage while maintaining low direct bubble contact. Additionally, we show that regular arrays of nanotextured nucleation promotion points can enable the release of consistently sized bubbles via coalescence induced departure. Our study therefore has important implications for gas evolving electrode design to primarily minimize contact, rather than focusing on the coverage of bubbles on an electrode's surface.

3.2. Introduction

Electrochemical gas-evolving electrode (GEE) design is relevant for many industrial applications where gas is evolved from an electrochemical reaction like the chlor-alkali process, used for chlorine gas production. Chlor-alkali production accounts for approximately 2% of annual electricity usage in the United States[1] with approximately 20% of the total chlor-alkali cell voltage being attributed to the negative impact of bubbles[2]. At any electrode's surface, bubbles will first nucleate once sufficient supersaturation has occurred locally and then continue to grow from diffusion of dissolved gas in the electrolyte to the bubble. Finally, an adhered bubble will detach, usually leaving behind a small nucleus of gas that can then begin to grow again, repeating this growth and departure cycle. These generated bubbles cause ohmic and activation losses while adhered as they can directly inactivate active catalyst area, cause losses from impeding mass transport and ionic conduction, and induce concentration variability near the electrode's surface. As a result, the impact that electrochemical bubbles can induce has been studied both theoretically and experimentally for decades[10–16].

A wide range of studies exist that investigate GEEs, including the impacts of concentration overpotential[18] and generated concentration gradients around bubbles[56], bubble nucleation models[23], and active methods to enhance the departure of bubbles by using ultrasonic[27] or magnetic[28,29] fields. Recent works have summarized current progress and methods for the study and mitigation of adhered bubbles on electrodes along with the formation of micro- and nanobubbles[2,17,57,58]. As a result of adhered bubbles' unique ability to negatively impact GEE performance, significant research has used surface engineering to advantageously alter the interactions between bubbles and electrochemical electrodes' surfaces. The surface engineering

approaches for these studies have either focused on altering electrode surface chemistry, surface roughness, or both to modulate a GEE's surface wettability[59]. For example, prior work has focused on the wettability impacts caused by altering the surface chemistry of nickel porous foams[60] and patterned hydrophobically modified electrodes[20] using PTFE, and others have altered electrode wettability by modulating the roughness of GEEs by using micropatterning[35]. In addition, other surface modification methods have been demonstrated to attempt to enhance performance of GEEs, such as promoting bubble nucleation away from the GEE active surface[19] and advantageous bubble manipulation via capillarity[24]. However, surface engineering has not yet been used to interrogate the degree to which bubble coverage of a GEE inactivates that electrode in a systematic manner. In this work, we aim to use surface engineering of a platinum oxygen evolving electrode to systematically control bubble/electrode interactions in an attempt to empirically validate the degree to which adhered bubbles inactivate GEE electrochemically active surface area (ECSA).

Among the many gas-evolving electrochemical reactions currently studied, there is currently a particular focus on discovering electrocatalyst materials for the oxygen evolution reaction (OER) to improve reaction kinetics and efficiency[6,7,61–65]. In addition, some studies have an explicit focus on advantageous bubble release to improve performance[8,9,66]. Optimizing the performance of OER electrocatalysts is of particular interest for sustainable energy development for water electrolysis in both acidic[61] and alkaline[67,68] aqueous environments as well as for solar water splitting[69,70] applications. As a result, machine learning based-approaches for materials discovery and performance prediction have shown recent promise to advance OER electrocatalysts[71–73]. However, machine learning has not yet been employed for the detection of bubbles from imaging data of GEEs during gas evolution, which has historically limited the ability to study the spatial and temporal impacts that bubbles have on the catalyst surface due to the difficulty of processing

imaging using traditional image segmentation methods. Currently, advanced machine vision techniques have not been applied to the study of electrochemical bubbles, despite its ability to be a powerful tool for investigation. Prior works have used traditional and less flexible methods for bubble detection including a combination of either manual annotation or a Hough Transform or similar detection of circular objects on binarized images to detect bubbles [74–78]. Furthermore, the use of machine learning models for the detection of bubbles in scientific research is currently limited to a small number of applications involving two phase flow, including the modeling and prediction of boiling heat transfer regimes[79–81], or in operational analysis of chemical engineering unit operations like fluidized beds[82] and floatation froth surfaces[83]. As a result of the limited demonstration of machine vision for adding value to experimental studies, there is a dearth of openly shared machine learning based bubble detection models and toolboxes published for researchers to use[84]. For this reason, we have developed a deep convolutional network for bubble detection for this study to aid in providing high fidelity and statistically powered bubble datasets to analyze the impacts of electrochemical bubbles.

Significant works have already been published over the past few decades providing a large resource for relationships between bubble coverage and a variety of electrochemical parameters like temperature and pressure[53]. However, the actual current density of GEEs that results as a function of the inactivation caused by adhered bubbles to its surface has not been sufficiently interrogated experimentally. Currently, the prevailing understanding is that the bubble coverage for a GEE is the best metric to determine the actual current density[53,85]. However, the rationale for inactivation is based from prior theoretical modeling[86], without significant empirical evidence to justify the assumptions made. Here, we combine surface engineering techniques and a machine learning bubble detection algorithm to systematically control and measure bubble/electrode

interactions to provide empirical evidence to suggest that the bubble coverage of GEEs is not entirely inactivated as is currently assumed. Instead, the evidence presented suggests that inactivation of the electrode is more likely confined to directly contacted bubble areas, rather than the conventional bubble coverage metric. By controlling the extent to which bubbles cover and contact GEEs' surfaces independently using surface engineering we are able to offer new evidence as to the nature of gas bubble inactivation for these systems. These new findings provide an alternative design framework by which to approach how GEEs should designed to limit active materials' inactivation during operation. By minimizing the direct contact of GEEs instead of the bubble coverage, new approaches for maximizing gas evolving electrochemical systems can emerge, which will be especially important for porous electrodes with high active material loadings that are prone to increased passivation by direct contact with generated gas bubbles.

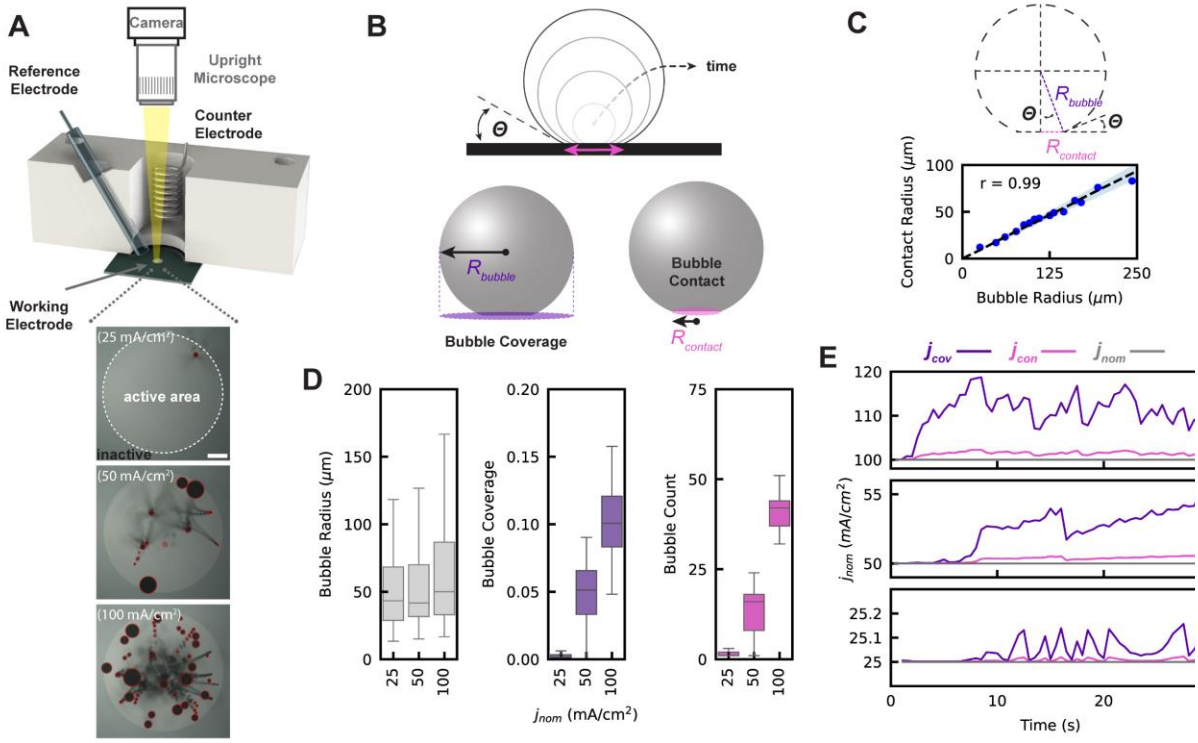

Figure 3-1. Experimental definitions and design for bubble detection measurements of OER on smooth Pt electrodes. (A) Experimental setup used to acquire images used for bubble detection and analysis. Representative images shown with red annotations for bubble's detected by ML algorithm. (B) Top shows a graphical schematic of an adhered bubble as its contact line is free to advance at a constant contact angle during growth on the electrode's surface. Below are graphical illustrations of the bubble coverage area and radius and bubble contact area and radius. (C) Top shows a schematic of the geometric relationship between bubble radius, contact radius, and contact angle. Below shows the measured contact radius as a function of the bubble radius for multiple growing adhered bubbles. Pearson correlation coefficient 'r' shows high agreement between the predicted values using the constant contact angle model where θ measurements were $22° \pm 2°$, in agreement with bubble contact measurements as shown by dotted line and shaded upper and lower bounds. (D) Boxplots describing the statistics of bubble radius, bubble coverage and bubble count for adhered bubbles imaged during experiments with smooth electrodes at multiple nominal current densities. (E) $\boldsymbol{j_{nom}}$ (gray trace), $\boldsymbol{j_{cov}}$ (purple trace), and $\boldsymbol{j_{con}}$ (pink trace) current density values using bubble detection data.

3.3. Experimental Methods

3.3.1. Adhered Electrochemical Bubbles on Smooth Electrodes

To measure the impacts that adhered gas bubbles have on GEEs, an electrochemical cell was fabricated for experiments to observe bubble evolution on working electrodes from a top-down perspective (Figure 3-1A, top). The model electrochemical reaction used throughout this work is Pt-catalyzed OER in an acidic electrolyte of 0.5M H_2SO_4 as similarly described in previously published work[87]. A Pt catalyst was chosen as it is widely studied, well-characterized and stable, avoiding any complications that could arise from using a novel, less well-understood catalyst. A circular active Pt working electrode of 3 mm in diameter was patterned, surrounded by an inactive region of silicon nitride (Figure 3-1A, bottom). The focus of this study is on current density operation between 25 and 100 mA/cm^2 on a geometric basis, approaching a range high enough to be of relevance for commercial electrochemical device operation, like for alkaline water electrolyzer operation[45] where bubble effects are industrially significant.

The nominal current density, j_{nom}, is defined as the total current passing through the working electrode, I_{tot}, divided by the working electrode's geometric area, A:

$$j_{nom} = \frac{I_{tot}}{A}$$

In this work, we will denote the relative bubble inactivation as ϕ, such that the actual current density for the working electrode during experiments is defined as:

$$j_{actual} = \frac{j_{nom}}{(1-\phi)}$$

As such, ϕ represents the fractional portion of the electrode area between 0 and 1 that is inactivated at a given time due to the presence of adhered bubbles. In prior works, the bubble coverage is proposed as defining ϕ. Here, we aim to determine whether or not this is an appropriate approximation by measuring the bubble coverage and electrochemical potential fluctuations for a number of current-controlled experiments under different degrees of both bubble coverage and bubble contact. As shown in Figure 3-1B, the bubble coverage is defined consistently with prior work[46] as the ratio of the shadowed area of adhered bubbles on the surface of the electrode to the electrode's total geometric surface area. The bubble coverage will be designed here as ψ rather than θ, which was used by previous authors[46], to avoid confusion with the more commonly referred to contact angle designation of the Greek letter theta in interfacial science. Also shown in Figure 3-1B, is the bubble contact, designated by φ, defined as the ratio of the directly contacted area of adhered bubbles on the surface of the electrode to the electrode's total geometric surface area. Using these definitions, two additional current densities can be defined based on either the bubble coverage, or the contact coverage as follows:

$$j_{cov} = \frac{j_{nom}}{(1-\psi)}$$

$$j_{con} = \frac{j_{nom}}{(1-\varphi)}$$

As was demonstrated in prior work[87], adhered gas bubbles which grow on extremely smooth surfaces as those used in this study do not experience pinning. As a result, adhered bubbles' contact line advances at a constant contact angle, θ, as they grow in size, as shown graphically in the top portion of Figure 3-1B. We can confirm this by imaging the dynamics of adhered bubbles' contact

lines on these smooth electrodes as a function of the bubble radius, which forms a linear relationship according to $R_{contact} = R_{bubble}\sin(\theta)$, as shown in Figure 3-1C. Using this relationship, we can now measure bubble coverage and infer the bubble contact indirectly, allowing us to dynamically track both the bubble coverage and bubble contact over time using our developed bubble detection algorithm.

Using this experimental setup, we next measured the evolution of the bubble coverage while the working electrode was controlled to maintain constant nominal current densities of 25, 50 and 100 mA/cm^2 over time. Using our bubble detection algorithm, we are able to capture and summarize relevant bubble metrics for the experiments, shown in Figure 3-1D, of the distributions of adhered bubble size, bubble coverage and number of adhered bubbles. We find that as the nominal current density is increased, the median and range of bubble size and bubble count both increase as well, leading to increased bubble coverage of the electrode at higher current densities. Finally, we can plot and compare the fluctuations in the bubble coverage-derived and bubble contact-derived current densities to compare to one another as shown in Figure 3-1E. Due to the larger range in bubble dynamics for higher current density, the fluctuations in both the bubble coverage derived and contact derived current densities deviate more and more from the nominal current density as it is increased. However, two difficulties emerged when using smooth electrodes for studying the impacts of bubble coverage. The first is that there is a set relationship between the bubble coverage and bubble contact which can only be altered by changing the contact angle of bubbles adhered to the working electrode. For smooth surfaces, this simply leaves the option to alter the chemistry of the active surface, which is beyond the scope of the efforts here. The second is that very small plumes of rapidly evolving and departing bubbles on the order of 10 microns in radius make it difficult for top-down imaging to accurately view the surface of the electrode below these plumes,

as bubbles rising through the field of view after departing, obfuscate the surface below. As a result, we opted to shift to using engineered surface morphologies of these smooth electrodes to include microscale ‘nanospots’ which have a nanoscale roughness to promote the preferential nucleation of adhered gas bubbles to particular locations on the working electrode. In doing so, we have a greater degree of control over bubble/electrode interactions to enable our developed machine learning bubble detection algorithm to work best, the details of which will be described next, prior to the results for the surface engineered electrodes.

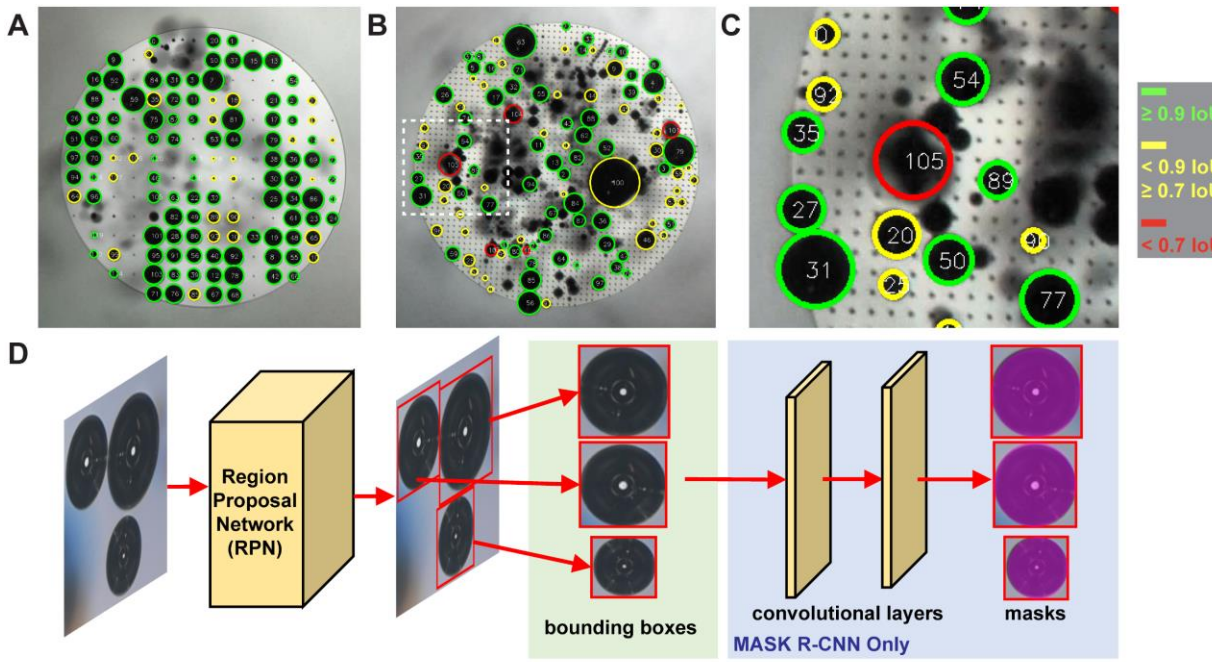

Figure 3-2. (A) Image of b200 grid-nucleated surface with oxygen bubble nucleation annotated with predictions and intersection over union (IoU) scores. Green denotes the highest IoU (≤ 0.9) while red denotes the lowest (< 0.7). Bubble predictions were generated using the Faster R-CNN V2 architecture. See Table X for overall mAP and IoU results per model architecture. (B) Image of b50 grid-nucleated surface with oxygen bubble nucleation, also annotated with predictions and IoU scores. (C) Subset of inset B) highlighting bubble predictions with various IoU scores. Note that Bubble 105, which has an IoU < 0.7, is a false positive detection of bubbles after they have detached from the surface. Only attached bubbles are considered valid predictions. Low-scoring predictions are frequently false positives or very tiny bubbles. (D) Diagram of the high-level ML architecture used for bubble identification. Note that the Mask R-CNN architecture has additional convolutional layers to produce the masks, while the Faster R-CNN does not.

3.3.2. Deep Learning for Bubble Detection

In order to draw insights about bubble nucleation, growth and departure for time series experiments, we utilized supervised ML neural network architectures to label individual bubbles across video frames. To carry out supervised ML, we manually labelled images taken from videos of GEE bubble evolution for both smooth and grid-nucleated surfaces. To enhance the relatively small set of manually labelled images, we used both classical data augmentation strategies such as blurring, sharpening, rotating, and cropping, as well as more custom methods including contrast limited adaptive histogram equalization (CLAHE)[88,89].

We trained both a Mask R-CNN[90] model as well as a Faster R-CNN[91] model, two network architectures that are now commonly used for object detection and tracking in numerous contexts and domains[92–94]. We employed the original versions (V1) as well as improved versions (V2) of both network architectures by work in Li et al.[95] A general diagrammatic representation of these architectures is shown in Figure 3-2D. The models were initialized with weights aggregated from the COCO dataset[96]. Models were first fine-tuned using images of bubble nucleation on smooth surfaces, then further tuned using a set of labeled images of bubble nucleation on grid-nucleated nanospot surfaces described in the next section. We also benchmarked our supervised methods against an implementation of circle Hough Transform, to serve as a classical computer vision baseline[97]. All tests were run on an NVIDIA A100 GPU, with 70% of annotated images used for training, 20% used for validation, and 10% used for testing.

We used hyperparameter optimization (HPO) to determine the optimal values for several network parameters, such as learning rate, number of training epochs, and batch size. The optimal parameters were found using Asynchronous Successive Halving Algorithm (ASHA)[98], and the result returning the highest mean average precision (mAP) score was used for later evaluation. The

performance of these models was evaluated based on both mAP and intersection over union (IoU) metrics. mAP scores measure the precision in the predictions of overall bubble detections, and IoU scores measure the overlap of the predicted bounding boxes with the ground truth bubble annotations (i.e. the ”tightness” of the match). Inference results were evaluated by two expert reviewers to determine the visual quality and practical utility of the bubble detections. Note that given a single class of objects (bubbles), the mAP score is equivalent to an average precision metric. Examples of segmented image frames are shown in Figure 3-2A,B,C and a table detailing model performance versus our benchmark is included in supplemental information (see Appendix §7.1.5).

Additional details regarding hand-labeling, computer vision methods, augmentation strategies, model architectures, model training, and evaluation can be found in the Supplemental Information (see Appendix §7.1.5).

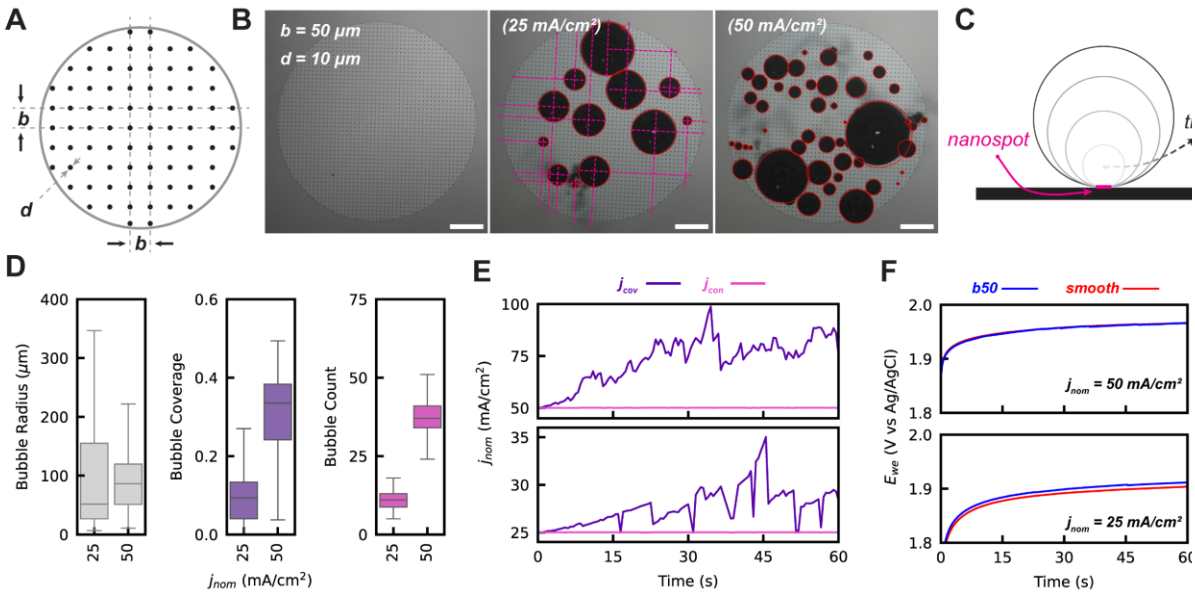

Figure 3-3. Surface engineering of electrode surfaces to include a regularly spaced grid of nucleation-promoting nanospots to enhance the bubble coverage while decoupling its relationship from the contact radius for adhered bubbles. (A) Graphic illustration of the design space for nucleation-promoting nanospots with a spacing ***b*** between adjacent nanospots of diameter ***d***. (B) Illustrative images of a nanospot patterned electrode with parameters ***b***=50 µm and ***d***=15 µm, operating at 25 mA/cm^2 and 50 mA/cm^2, as shown from left to right. (C) Graphic illustration showing how nanospots decouple the relationship between bubble radius and contact radius, as the contact line is pinned to the edge of the nanospot, limiting its ability to advance as on smooth surfaces. (D) Boxplots describing the statistics for the bubble radius, bubble coverage, and bubble count of adhered bubbles imaged during experiments with the b50 nanospot electrodes at multiple nominal current densities. (E) Coverage-derived, $\boldsymbol{j_{cov}}$, and contact derived, $\boldsymbol{j_{con}}$, actual current densities over time based on coverage and contact data. (F) The working electrode applied potential as a function of time during current-controlled experiments at the nominal current densities labeled for both the b50 nanospot patterned and smooth electrodes.

3.4. Results and Discussion

3.4.1. Nanospot Grid Patterned Electrodes to Control Adhered Bubbles

In an effort to maximize the bubble coverage while minimizing the bubble contact, surface engineering of regularly spaced nucleation-promoting nanospots was envisioned, as shown graphically in Figure 3-3A. The design parameters for these electrodes are the spacing between adjacent nanospots, designated by b, and the diameter of the nanospot itself, designated by d. The initially designed nanospot electrode used a spacing b = 50 μm and a diameter d = 10 μm. This resulted in a density of nanospots of approximately 27,842 nanospots/cm^2. At the low and moderate current densities tested of 25 and 50 mA/cm^2, we can demonstrate that bubbles indeed preferentially nucleate and grow almost exclusively at these nanospot locations, as shown in Figure 3-3B. The utility of using nanospots for investigating the impacts of adhered bubbles are primarily due to (1) their ability to spatially control the location of adhered bubbles by promoting nucleation at these nanotextures regions by lowering the free energy barrier to do so, and (2) to decouple the linear relationship between bubble coverage and bubble contact that is observed for smooth electrodes. This second benefit is shown graphically in Figure 3-3C, as an adhered bubble's contact line is effectively pinned to the extent of the nanospot, and the bubble radius continues to grow, as the contact area remains constant. By virtue of this approach, the bubble coverage can now be amplified to a greater extent as compared to the bubble contact, which is now solely a function of the number of bubbles adhered to the working electrode's surface, defined as $\varphi = NA_{nanospot}$ where N is the number of bubbles adhered to the electrode surface and $A_{nanospot}$ is the area of the extent of single nanospot. The high degree of control and repeatability offered by using this approach makes it an ideal way to understand the way that bubble coverage and contact are related to the dynamics of a GEEs electrochemical performance.

As shown in Figure 3-3D, the *b50* nanospot electrodes show an increase in the median bubble size but a decrease in the range of bubble sizes observed as the nominal current density is increased. This is due to the fact that at low current densities, only a small fraction of nanospots is occupied with a bubble at any given time. For example, the median count of adhered bubbles on the surface of the *b50* electrode at j_{nom} = 25 mA/cm^2 is 11 bubbles, while increasing the nominal current density to 50 mA/cm^2 causes this figure to more than triple to 37 bubbles. The higher number of bubbles adhered to the surface at a given time and larger bubble sizes due to increased pinning to the nanospots combine to allow the nanospot surfaces to maintain larger bubble coverages over time while having lower bubble contact as intended. As shown in Figure 3-3E, this promotion of bubble coverage allows for bubble coverage derived current densities to approach twice that of the contact derived current density, which remains effectively equivalent to the nominal current density applied due to contact remaining significantly below 1% throughout the experiments.

However, the *b50* nanogrid surface promotes too many bubbles to nucleate at the highest applied nominal current densities of 100 mA/cm^2, making it difficult to view the surface due to bubble obfuscation, as shown visually in Figure 2C where IoU scores for the bubble detection algorithm can drop below 0.7 due to this clouding of the surface with many rapidly departing bubbles. As a result, the bubble detection algorithm is not reliable for these conditions and other working electrodes configuration must be used for testing. To do this, the spacing parameter b needs to be increased to lower the density of nanospots to a degree at which a high occupancy of bubbles can be maintained on the majority of nanospots over time.

Finally, it is of particular interest to note that the applied potentials required to maintain equivalent nominal current densities are almost identical in both the smooth and *b50* nanospot electrode cases, as shown in Figure 3-3F. Even with the addition of the nanospots, the ECSA for

both the smooth control surfaces and these *b50* nanospot electrodes are within approximately 1% of one another, owing to the minimal surface fraction that is occupied by the nanospot patterns. As a result, the fact that applied potentials are so similar between smooth and the patterned *b50* electrode begin to support the hypothesis that bubble coverage is less inactivating relative to contact.

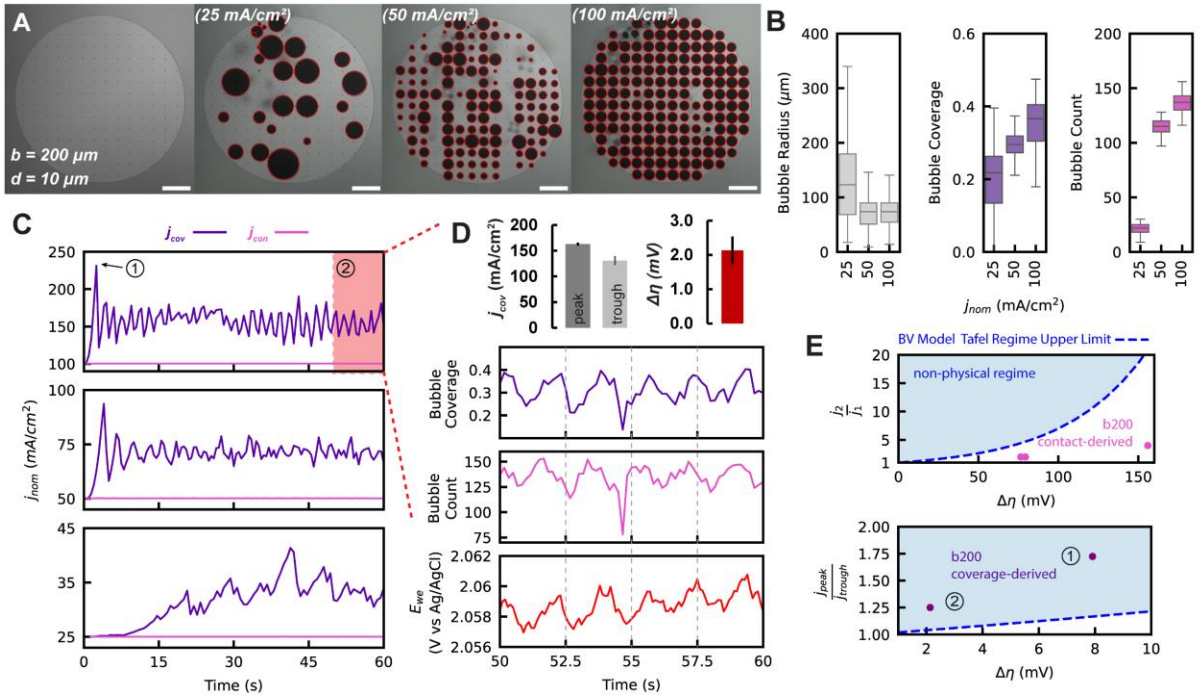

Figure 3-4. Optimizing the spacing of nucleation-promoting nanospot electrodes to limit bubble size of departing bubbles and maximize bubble coverage during operation for periodic oscillations in bubble coverage. (A) Illustrative images of a nanospot patterned electrode with parameters ***b***=200 µm and ***d***=10 µm, operating at 25 mA/cm^2, 50 mA/cm^2, and 100 mA/cm^2, as labeled from left to right. (B) Boxplots describing the statistics for the bubble radius, bubble coverage and bubble count of adhered bubbles imaged during experiments with b200 nanospot-patterned electrodes at multiple nominal current densities. (C) Coverage-derived, $\boldsymbol{j_{cov}}$, and contact derived, $\boldsymbol{j_{con}}$, current densities over time based on coverage and contact data. (D) Final ten seconds of 100 mA/cm^2 nominal current density experiment highlighted in C to show the periodic oscillations in working electrode potential $\boldsymbol{E_{we}}$ moving with the bubble coverage and bubble count. (E) Top shows the contact-derived currents compared to one another and their respective increase in applied overpotential required being below the upper limit model proposed. Bottom shows the coverage-derived fluctuations during our experiments as falling above the upper limit model proposed.

3.4.2. Optimizing Nucleation Grid Promoting Electrodes to Maximize Coverage

In order to lower the density of nanospots on the working electrode, a spacing parameter of ***b*** = 200 μm was used, lowering the number density of nanospots by an order of magnitude relative to the *b50* design to 2320 nanospots/cm^2. This *b200* nanospot electrode design was intended to enable regular release of bubbles of a maximum diameter that is approximately equivalent to the spacing size. This is due to the fact that at high occupancy of bubbles on nanospots, the primary mechanism by which most bubbles will depart becomes coalescence-induced departure. As bubbles encounter a neighboring bubble, coalescence will occur which will transfer surface energy to potential energy via a 'jump' in the resulting coalesced bubble, as has been previously studied[99].

As shown visually in Figure 3-4A, at moderate and high current densities of 50 and 100 mA/cm^2, there is a high degree of bubble occupancy on the *b200* electrodes. As shown in Figure 3-4B, the median bubble counts adhered to the electrode at a given time are between 100 and 150 for these conditions, relative to the total number of nanospots of 164 for the *b200* design, thus demonstrating that the majority of nanospots are occupied by bubbles most of the time during experiments. As a result, these electrodes are highly bubble covered, with bubble coverages ranging between approximately 0.2 and 0.6, as shown in Figure 3-4B. Additionally, the control of maximum bubble size of the nanospot electrode patterning is also demonstrated by the tightly controlled distributions of bubbles detected on the electrode's surface to being approximately sized by the parameter ***b***, as also shown in Figure 3-4B.

These electrodes periodically shed groups of bubbles via coalescence-induced departure, creating regular fluctuations in the bubble coverage which is especially pronounced at the highest nominal current density tested of 100 mA/cm^2. This is manifested in the bubble coverage-derived current density j_{cov} showing sustained and significant fluctuations throughout experiments, as

shown in Figure 3-4C. The oscillations become more relatively pronounced and frequent as the applied nominal current density is increased (Figure 3-4C). This allows for analysis of these periodic trends over time, which is highlighted for the final 10 seconds for the 100 mA/cm^2 b200 electrode case in Figure 3-4D. As is shown in this figure, the current fluctuates between local peaks and troughs in a highly temporally aligned manner with fluctuations in the measured potential of the working electrode, E_{we}. On average, these fluctuations in j_{cov} move between peaks of approximately 163 mA/cm^2 and troughs of approximately 131 mA/cm^2 regularly over the course of a few seconds, and correspond to a fluctuation in E_{we} of only approximately 2 mV, as shown in the upper portion of Figure 3-4D. These relative changes of approximately 25% in j_{cov} are unexpectedly large when looking at relatively small changes in the measured value of E_{we} of 2 mV, equivalent to relative fluctuations in the applied potential on the order of ~ 0.1%. As a result, we seek to propose physical arguments to justify that these small measured changes in E_{we} could not be responsible for such large changes in current density as would be required if a bubble-derived current density were most accurate.

3.4.3. Physical Arguments for Most Relevant Bubble Inactivation Metric

To obtain a physical upper limit for the actual current densities achievable for a given applied potential, the Butler-Volmer model in the upper limit of the Tafel Regime was used, as shown in the following equation:

$$j_{upper\ limit} = j_o \exp\left\{\frac{\alpha z F}{RT}\eta\right\}$$

where j_o is the exchange current density, α is the transfer coefficient, z is the valence of relevant electron transfer, F is Faraday's constant, R is the universal gas constant, T is the temperature, and η is the overpotential applied to the electrode,

In this way, this current density represents the upper limit of a current density that is achievable, as it only considers activation losses at the electrode, neglecting the relevant effects of mass transport or ohmic losses that also limit the current achievable for a real GEE, especially when operating at high reaction rates. By taking the ratio of $j_{upper\ limit}$ for multiple conditions for the same electrode, we can obtain a ratio that relates how a change in overpotential would cause relative increases in the actual current density if activation losses were the sole source of loss in the system, ignoring any mass transport effects, as shown in the following equation:

$$\frac{j_2}{j_1} = \exp\left\{\frac{\alpha z F}{RT}\Delta\eta\right\}$$

In this case, j_2 and j_1 represent the actual current densities for two different operating conditions of the electrode under test, and $\Delta\eta$ represents the difference in overpotential between those two conditions (i.e. $\Delta\eta = \eta_2 - \eta_1$). It is convenient to look at these relative changes, as it avoids the requirement to determine the absolute value of the exchange current density for the reaction, which can vary by orders of magnitude depending on the conditions of the reaction and materials used. Instead, we only require a reasonable value for the transfer coefficient, whose value is less variable and can be found in literature to be approximately 0.5 for Pt-catalyzer OER at high overpotentials[100].

Next, we can plot the measured changes in overpotential between the three different nominal current density operating conditions for our tests and compare them with the upper physical limit imposed by only considering Butler-Volmer kinetics as described. As shown in the upper plot of Figure 3-4E, the relative increases in contact-derived current densities between experiments given their difference in overpotential fall below this upper limit kinetic model, indicating that indeed there are likely significant losses due to mass transport and they are not operating in a purely

kinetically-limited regime. However, the bubble-coverage derived relative changes in current density consistently fall well above this upper given the corresponding small changes in overpotential during those fluctuations, as shown in the lower plot of Figure 3-4E.

As a result of these findings, we propose that the actual inactivation of the electrode's surface ϕ is most accurately approximated using the direct contact metric φ, rather than the bubble coverage metric ψ. From the measurements shown, it seems to be physically unlikely that bubble coverage is an accurate metric for determining the actual current density for a GEE. As a result, we suggest that the recently introduced bubble-induced electrochemically active surface area (BECSA)[87] be defined relative to its ECSA as $BECSA = ECSA * (1 - \varphi)$. We believe utilizing BECSA for the relevant area for actual current density determination provides a more accurate representation of the dynamic current densities of a GEE during operation.

3.5. Conclusions

In summary, we have systematically studied the dynamic relationship between bubble coverage and bubble contact during current-controlled experiments on both smooth and surface engineered Pt oxygen evolving electrodes. Additionally, a machine learning based bubble detection algorithm was developed to allow for statistically-powered dataset generation without the need for human intervention to annotate bubbles adhered on the electrode surface. This tool can become useful for the scientific community not only studying electrochemically generated bubbles, but for those studying other adhered bubbles as well. While pristinely smooth electrodes cause a bubble's radius and its contact to be linearly related to the contact angle formed at the electrode, surface engineered electrodes were shown as a useful way to decouple this relationship. Nucleation promoting nanospot arrays were demonstrated to both control where bubble nucleated spatially, and limited their contact to the nanospot area, allow for increasing the bubble coverage while maintaining a minimal bubble contact for electrodes under test. An optimized version of these nanospot engineered electrodes was demonstrated to produce a periodic bubble coverage signal as adhered bubbles of a controllable size were regularly released via coalescence induced departure with neighbors. When coupled with synchronized chronopotentiometry data, we were able to show that defining the bubble coverage as entirely inactivating of a GEE is not physically likely and is supported by physical modeling of an upper activation limited regime, which these values exceed. Finally, the bubble contact area, rather than the bubble coverage area is proposed as an improved approximation for the area that is inactivated by adhered bubbles and a definition for the corresponding BECSA is defined. As a result, an important new GEE design paradigm emerges that can focus primarily on minimizing the direct contact between adhered bubbles and an electrode, as opposed to the conventional bubble coverage metric. This new perspective brings

with it important implications for the fabrication of more highly efficient GEEs, emphasizing the importance of materials considerations and the surface engineering of those electrodes to minimize the inactivating effects caused by adhered bubbles.

4. Ultra-fast Absorption of Carbon Dioxide Gas Bubbles using Nanoengineered Capture Surfaces

4.1. Summary of Concept and Contributions

The effective reaction of gases with liquid absorbents is a critical part of many large-scale industrial processes. Specifically, when the gas phase within an absorber unit exists as discrete bubbles, as is the case for bubble column absorbers or gas sparging systems, the capability of these bubbles to effectively react relies on careful control the bubbles' properties and their flow. Here, we demonstrate the effectiveness of a novel mode for the absorption of gas into a liquid absorbent by using nanoengineered surfaces to spread bubbles into their texture and enhance the mass transport between the gas and liquid phases. By using this surface enhanced direct injection method for gas absorption, we are able to achieve 2 orders of magnitude improvement in reaction rates in comparison to captive bubbles in the absorption of carbon dioxide gas while using a moderately alkaline potassium hydroxide as an absorbent solution. While non-spreading bubbles' average reaction rates tend to decrease with bubble size, the surface enhanced absorption of spreading bubbles reverse this trend, enabling the most rapid absorption for the smallest bubbles. Additionally, non-spreading carbon dioxide bubbles are unable to be completely absorbed due to product aggregation at their interface, while spreading bubbles are able to avoid this regime by reacting on rapid timescales much faster than the aggregation process. Finally, we introduce this mode of surface enhanced direct injection as an absorption technique with advantageous scaling for small scale or distributed modular absorber designs in comparison to traditional, large scale absorber units used today throughout industry.

4.2. Introduction

Absorption of gas into aqueous media has a multitude of important industrial applications. The most common method for this is by using an absorber, which is a common chemical engineering unit operation for separations, which include common gas/liquid contactor varieties including packed tower, spray column and bubble column varieties, among others[101]. These absorption approaches aim to maximize the interaction between the gas and liquid phases to promote improved mass transport. These approaches, like using absorption towers, are especially common for the removal of potentially hazardous gases from being released into the atmosphere during industrial activities. For example, packed tower absorbers are used for a variety of chemical scrubber applications, like in NO_x removal[102] or in the absorption of carbon dioxide[103] or ammonia gases[104]. The details of operation for various modes of absorption units and their associated fundamentals and design parameters have been extensively described in many textbooks[105].

In certain types of reactive absorber units, like in bubble column type absorbers, the gas phase exists primarily as discrete bubbles rather than a bulk gas phase contacting thin films of liquid absorbent[101]. As a result, injection of bubbles directly into reactors that readily react with the surrounding liquid media is a common practice in a variety of industries to enhance mass transport between the gas and liquid phases. However, in certain applications, the formation of foams from the injection of bubbles can be disadvantageous and causes issues. For example, in the case of sparged gas to support the operation of bioreactors, foams can decrease reactor yield[106] and can even cause cell death when bubbles rupture[107,108]. The need to use spargers for aeration in fermenters and bioreactors is also of critical importance to the cultivation of bacteria and algae for a variety of bioreactor types, including photobioreactors and miniature bioreactors[109–111]. As a result, helping to mitigate the generation of foams using defoamer additives to limit these negative

impacts is a multi-billion-dollar market that continues to grow[112]. In addition, sparging gas for dissolution into liquid is a widespread and important processing step for activities in the food industry, like in the aeration of beverages[113], and as a pre-processing step in water treatment using injected bubbles to aid in removal of solid particulate and oils [114,115] as well as antifouling of membranes in submerged anaerobic membrane reactors (SAMBRs) for sewage treatment[116,117].

Due to the intense current focus for scientists and engineers around the world to enable technologies to mitigate climate change and provide sustainable energy solutions, the absorption of carbon dioxide, CO_2, has become a particularly important system to study due to carbon dioxide's central role in global climate change and future sustainability considerations. As a result, the model system studied in this work is the absorption of CO_2 gas in an alkaline aqueous solution of potassium hydroxide of moderate ionic strength. The absorption of CO_2 bubbles in various alkaline solutions has been extensively studied previously, which provides useful references for physical constants and prior experimental results with which to make comparisons[118–120]. Additionally, the capture[121,122], conversion[123] and storage/utilization[124] of carbon dioxide is a key challenge of the present, with a multitude of approaches being proposed. Traditional means of chemical absorption and physical adsorption are common routes for the separation of CO_2 from both dilute and higher concentration streams[125]. More recently, novel and promising electrochemical methods for carbon dioxide separations have also been demonstrated[126].

From a carbon storage perspective, CO_2 mineralization efforts span a wide range of methods and applications[127,128] including CO_2 mineralization using waste streams[129,130], saline sources like ocean water[131], and by injection of CO_2 into geologic formations[132]. For example, the mineralization of CO_2 in geological formations is currently done at relatively large scales as in Sleipner Field off the cost of Norway in the North Sea[133], with ~1 Mt of CO_2 injection annually,

as well as in newer pilot scale facilities like the CarbFix project in Iceland[134–136]. However, the processes associated with this type of underground storage occur over geological timescales, taking many years for the mineralization reaction to be completed to fix the carbon dioxide into a mineralized form. For example, recent results published by the CarbFix team report ~200 tonnes of CO_2 injected at depth was almost completely mineralized after approximately 2 years[137]. The wettability of the rock formations into which CO_2 is injected has critical implications in the permeability and mineralization dynamics, as well as the storage capacity when carbon is sequestered in this manner, like in deep saline aquifers[138]. However, the wettability of the any solid surface in contact with a gas targeted to be absorbed also has significant consequences in traditional absorbers as well, like packed tower absorbers. In these packed tower arrangements, the packing materials are typically coated to promote wetting of the liquid absorbent to create a continuous film, creating the interface which the target gas is absorbed on[101]. However, the work presented here is interested in engineering surfaces that demonstrate advantageous benefits for spreading CO_2 gas bubbles into their textures to promote enhanced absorption into an alkaline media that is less wetting to the surface that the gas. In this way, capillary forces can be used advantageously to spread the bubble to be absorbed and enhance the mass transport between the gas and liquid phases relative to a bubble rising in the liquid media as is the case in a bubble column type absorber.

To realize this end, engineered superhydrophobic surfaces will be developed to spread bubbles and improve mass transport by advantageous geometric manipulation of bubbles via capillary forces. Prior work has rigorously analyzed the dynamics of spreading air bubbles' fundamentals, but these bubbles did not readily react with the surrounding liquid media[139]. Additionally, work on bubble capture has utilized similar surfaces for the rapid spreading of

bubbles into capture surfaces for the prevention of foam accumulation at free interfaces for industrial applications[140]. Again, this study presents a method for the removal and mitigation of foam accumulation and does not investigate a readily reacting gas/liquid system. To the authors' knowledge, no work has yet been shared which studies spreading bubbles on nanoengineered surfaces with a bubble that rapidly reacts with the surrounding liquid media. Here, we present a system which enhances the reaction rates of CO_2 relative to plain bubble reaction rates by spreading the gas into nanoengineered capture surfaces. While the system presented here is motivated towards developing an absorber system which could be uniquely suited for small-scale and distributed CO_2 absorption applications for sustainability, the results are relevant for any gas/liquid absorption system and have general relevance for other chemical reactions for absorption.

4.3. Experimental Methods

To measure the reaction rates for captured bubbles on capture surfaces to serve as a baseline to quantify the evolution of the absorption of a gas bubble, a setup to image the captive bubbles from a side profile was developed (Figure 4-1A). Stainless steel dispensing needles were used to deliver single bubbles of pure CO_2 gas to the capture surface which was submerged in 0.1 M KOH. Additional information on the experimental setup and the single bubble delivery system are detailed in the supporting information (see Appendix §7.2.4 for additional experimental setup detail). After bubbles are rapidly deposited onto the capture surface, videos of the evolution of their absorption are collected and image processing is used to extract the volume evolution of the bubbles during their reaction with KOH throughout the experiments, as shown graphically in Figure 4-1B. (see Appendix §7.2.2 for additional image processing detail). Resulting data can then be analyzed to arrive at reaction rates for the CO_2 bubbles' absorption in the KOH solution.

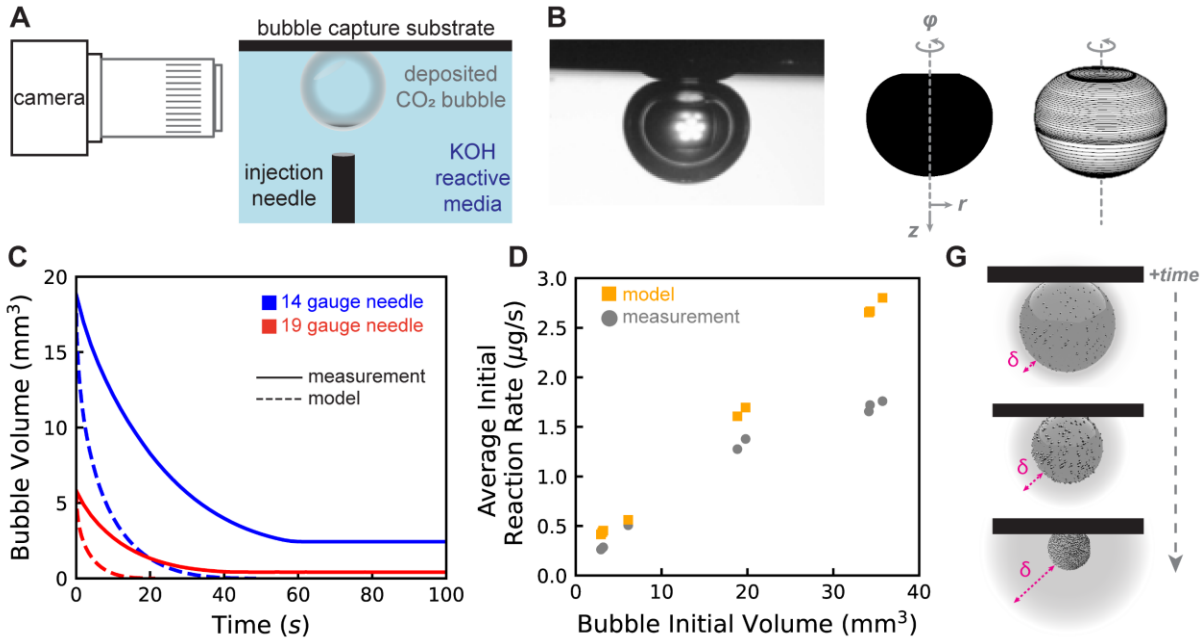

Figure 4-1. Experimental definitions and design for bubble detection measurements of OER on smooth Pt electrodes. (A) Experimental setup used to collect side-profile images of captured CO2 bubbles as they during absorption over time in 0.1 M KOH absorbate. (B) Illustrative image collected during data acquisition followed by binarization of the bubble image, which allows for rotating this 2D image around its approximate axis of symmetry to calculate the volume of the captured bubble as a function of time. (C) Plot showing the evolution of bubble volume due to absorption over time for two different sized captured CO_2 bubbles, delivered to the surface using two differently sized dispensing needles, in different colors. Solid lines represent directly measured results, while dotted lines represent predictions of the absorption of the bubble using the developed analytical model. (D) Plot showing the average initial rate observed over the first 20 seconds for the various bubble sizes tested, along with the corresponding predicted average rates for this same period as predicted by the model. (G) Graphical illustration of two phenomena occurring as time is elapsed for a captured bubble during experiments. First, the mass diffusion boundary evolves to grow over time as it is developed, denoted in pink by δ. Second, reacted particles that are formed at the interface accumulate over time until they cause the bubble absorption to effectively plateau and stop the reaction from continuing.

4.4. Results and Discussion

As shown in Figure 4-1C, the resulting data collected from the experiments shows two interesting features about the dissolution of captured bubbles on a hydrophilic capture surface where they remain relatively spherical in their shape throughout the absorption process. First, the reaction rates for bubbles drops off over time for both of the bubble sizes shown in Figure 4-1C of different sizes. Differently sized bubbles are achieved by changing the diameter of the dispensing needle used to deposit the bubble onto the capture surface. Second, after approximately 40 seconds for the smaller bubble shown by the red trace, and approximately 60 seconds for the larger bubble shown by the blue trace, the bubbles' absorption stops and the size of the bubbles plateaus as the bubble size remains constant and absorption is halted. Both of these features, namely the decrease of flux over time and the plateauing behavior have been reported previously and align with the observations made here[119,141–143]. The decrease in the flux at the bubble's interface is a result of the development of the diffusion boundary layer, depicted graphically in Figure 4-1E, as increasing in size over time, accordingly decreasing the flux. The plateauing behavior of bubbles is most likely due to the aggregation of reaction products at the interface, also shown graphically in Figure 4-1E. As the bubbles decrease in size, the interfacial area over which these particulates reside accordingly decreases, and eventually their presence effectively passivates the interface from continuing to react. For much higher concentrations of hydroxide solutions, it has been previously observed that a visible and solid shell will rapidly form around the CO_2 gas bubble, also stopping the reaction from continuing[119]. To capture the mass transport phenomena occurring for the idealized case of a spherical bubble of a certain volume being absorbed in a hydroxide solution, a numerical model was developed to compare against the experimental results captured for bubbles of various sizes deposited onto a smooth silicon substrate as an analog to a stagnant bubble being

absorbed in solution. The details of this reaction-diffusion model will be summarized in a subsequent section.

In Figure 4-1C, the dotted traces of different colors correspond to the model's prediction of the evolution of gas absorption for the bubbles tested. First, the model predicts higher rates throughout the course of a bubble's absorption due to the simplification that the spherical bubble that is modeled does not have the capture surface impeding KOH access and limiting some portion of the bubble's surface area, so this difference is expected. Second, the model predicts that bubbles are completely absorbed by the hydroxide solution, which is also expected as the secondary aggregation of reaction products on the interface is not included in the model. However, the primary aim of the numerical model developed here is to accurately predict the order of magnitude of reaction rates for the bubbles we are testing, as we aim to substantially decrease the timescale for these bubbles to be absorbed by engineering the capture surface to promote enhanced mass transport via spreading the gas into the superhydrophobic surface texture. For the larger bubble deposited in Figure 4-1C of approximately 18 mm^3 in initial volume, the predicted lifetime is approximately 45 seconds, while the smaller bubble of approximately 6 mm^3 in initial volume takes approximately 20 seconds to be completely absorbed. The explicit goal of this work is twofold: (1) decreasing the timescale of absorption for CO_2 bubbles like these to the order of milliseconds rather than tens of seconds and (2) enable the complete absorption of these gas bubbles to avoid the plateauing behavior shown for these initial experiments. Next, we discuss the numerical model that allows us to predict and compare with empirical results for the tested conditions for the remainder of experiments.

4.4.1. Modeling the Rate of CO_2 Bubble Absorption Numerically

A reaction-diffusion numerical model was developed to allow us to predict the associated reaction rates and timescales for complete absorption of CO_2 spherical bubbles suspended on the capture surface in KOH solution to compare with the relatively spherical bubbles deposited onto hydrophilic surfaces, like those shown in Figure 4-1. In addition, the model will also aid in predicting the fully spreading bubble case for comparison which will be demonstrated in a later section. As previously discussed, the numerical model developed is focused on the prediction of the order of magnitude of reaction rates rather than having much higher degrees of accuracy and is also a tool to predict what we should expect from a spreading bubble system from an order of magnitude perspective.

For the modeled system of chemical absorption we are studying, KOH and CO_2 undergo the following irreversible reaction, where k represents the reaction rate coefficient for the reaction:

$$KOH + CO_2 \xrightarrow{k} KHCO_3$$

The equations of conservation of mass for OH^- and CO_2 dictate the behavior of the system. We assume an immobile bubble boundary (the quasi-stationary assumption), eliminating the advective transport term of the conservation equations, and we are left with a reaction-diffusion system. As such, the system of two coupled partial differential equations solved numerically are:

$$\frac{\partial c_{CO_2}}{\partial t} = D_{CO_2}\nabla^2 c_{CO_2} - k c_{CO_2} c_{OH^-}$$

$$\frac{\partial c_{OH^-}}{\partial t} = D_{OH^-}\nabla^2 c_{OH^-} - k c_{CO_2} c_{OH^-}$$

where c_{CO_2} and c_{OH^-} are the concentrations of the carbon dioxide gas and hydroxide ions present in the system respectively, D_{CO_2} and D_{OH^-} are the diffusivities of carbon dioxide and hydroxide respectively, k is the reaction rate coefficient, and t is time. This system is then solved using the appropriate boundary and initial conditions which are summarized in Table 4-1.

The system is solved using the MATLAB *pdepe* function in spherical and planar geometries. From the computed concentration profiles at each timestep, we calculate the CO_2 flux [mol/m^2/s] at the surface and multiply by the surface area of the bubble to obtain a CO_2 bubble dissolution rate at each timestep [mol/s]. The bubble volume and surface area at each timestep is continuously calculated using the current amount of CO_2 left in the bubble using the ideal gas law.

Convergence of bubble dissolution time via spatial and temporal mesh refinement was confirmed for both spherical and planar geometry (see Appendix §7.2.3 for details). Numerical CO_2 fluxes at times 0.05 s and 10 s match published textbook values for the same times well[119] (see Appendix §7.2.3 for comparison). Additional details referenced previously can be found in the supporting information section regarding numerical modeling, including a table of physical constants and material properties used in the numerical model (see Appendix §7.2.3).

Table 4-1: Boundary and initial conditions used for numerical modeling, where $\mathcal{H}$ represents the Henry's Law constant for CO_2, c_{CO_2} and c_{OH^-} are the concentrations of the carbon dioxide gas and hydroxide ions present in the system respectively, t is the time variable, and r is the spatial radial variable for a spherical coordinate system. R represents the radius of the bubble and $c_{bulk,\,OH^-}$ represents the bulk concentration of hydroxide ions in the system, which is 0.1 M in our case.

Type	Condition
Boundary Conditions (4)	$c_{CO_2}(r = R) = \mathcal{H} P_{CO_2}$ $c_{OH^-}\,(r \rightarrow \infty) = c_{bulk,\,OH^-}$ $\frac{\partial c_{CO_2}}{\partial r}(r \rightarrow \infty) = 0$ $\frac{\partial c_{OH^-}}{\partial r}(r = R) = 0$
Initial Conditions (2)	$c_{CO_2}\,(r \geq R,\, t = 0) = 0$ $c_{OH^-}\,(r \geq R,\ \ t = 0) = c_{bulk,\,OH^-}$

4.4.2. Altering Surface Chemistry of Capture Surface to Enhance Absorption

By altering the surface chemistry of the bubble capture surface, we can change the wettability of the bubble on the capture surface, causing it to spread due to the hydrophobic nature of the PTFE (polytetrafluoroethylene), commonly referred to by its brand name Teflon, on the smooth surface. As shown in Figure 4-2A, the hydrophobic modification of a smooth surface with PTFE indeed causes the bubble to spread on the substrate. However, this manipulation of the geometry of the bubble is insufficient to noticeably impact the dynamics of the absorption of the bubble relative to that of a smooth hydrophilic surface, as shown in Figure 4-2B. As shown, the decrease in the volume of gas over time is almost identical for a smooth silicon and smooth Teflon surface for the first 25 seconds of absorption. In addition, both the smooth hydrophilic and smooth hydrophobic surfaces show the plateauing effect of the CO_2 bubble stopping its absorption and remaining static while not reacting with the surrounding media. This similarity between the reaction rates of bubbles of various sizes being deposited on smooth capture surfaces that are hydrophilic silicon or hydrophobic Teflon is summarized in Figure 4-2C. As shown, a similar trend is observed that larger bubbles show a larger average reaction rate due to their larger surface areas, relative to smaller bubbles which react more slowly due to their smaller surface areas. These data highlight the critical requirement of having a roughened surface in addition to a sufficiently hydrophobic surface chemistry to allow for complete spreading of a captured bubble, which has been reported previously in bubble capture studies[140]. This motivates us to design and test a variety of micro- and nanotextured capture surfaces to determine an applicable capture surface that can enable rapid and complete spreading of the deposited CO_2 bubble on its surface.

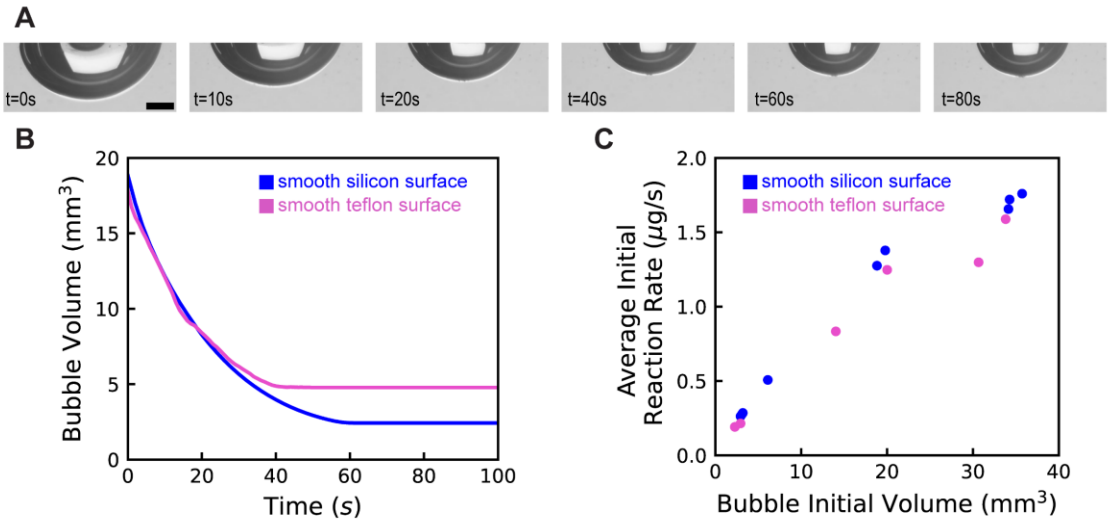

Figure 4-2. Investigation of the impact of surface chemistry on altering the absorption dynamics of CO_2 in KOH. (A) Time lapse images of a CO2 bubble deposited onto a smooth hydrophobic PTFE surface to enhance its surface area relative to its volume. (B) Plot showing the evolution of bubble volume due to absorption over time for two bubbles of equivalent volume placed on either a smooth silicon hydrophilic surface and a smooth PTFE hydrophilic surface, showing that effectively the same absorption dynamics are observed for the first approximately 25 seconds, and the plateauing behavior persists in both cases. (C) Plot showing the average initial rate observed over the first 20 seconds for the various bubble sizes tested for both a smooth silicon, hydrophilic, surface, and a smooth PTFE hydrophobic surface.

4.4.3. Nanoscale Superhydrophobic Surfaces to Rapidly Spread Gas Bubbles

It is well known that the addition of sufficient surface roughness to a surface with a hydrophobic surface chemistry can enable superhydrophobic surfaces with large equilibrium contact angles of 150º or more achieved in nature and in the lab[144]. Three different textured surfaces were fabricated for testing their abilities to spread bubbles rapidly and completely as they were captured on the surface. One surface with microscale roughness of a regularly spaced micropost array designated as "*b5*", a second with nanoscale roughness designated as "*ng*", and a third with hierarchical micro/nanoscale roughness designated as "*low-phi*", as shown in Figure 4-3A. All three of these surfaces were textured into silicon wafers and subsequently silanized to impart a hydrophobic surface chemistry for the three textured surfaces. The fabrication of these surfaces is outlined in more detail in the supporting information document (see Appendix §7.2.4). The equilibrium contact angles are shown for these three silanized textured surfaces along with an untextured, smooth silanized silicon substrate for comparison to emphasize the enhancement achieved via texturing.

Next, experiments were carried out for non-reactive bubbles spreading into these fabricated textures to compare their ability to readily spread bubbles without including the reactivity of the bubbles at this point. These results are summarized in series of time lapse photos taken from high-speed imagery of the capture and subsequent spreading of air bubbles in deionized water over the course of approximately 10 ms, shown in Figure 4-3C-E. In Figure 4-3C, it is shown that microscale texture alone from the *b5* texture, despite having a large equilibrium contact angle, is unable to completely spread the bubble. Instead, the bubble remains attached to the needle after the contact line is pinned to the surface and halts spreading approximately 8 ms after it is first captured by the surface. In contrast, both the purely nanoscale *ng* texture and the hierarchical

micro/nanoscale *low-phi* texture are able to achieve complete spreading, removing the air bubble from the needle and spreading the gas continuously at a higher speed than the microscale *b5* texture, as shown in Figure 4-3D and Figure 4-3E respectively.

A final test was performed to ensure that the thermodynamically stable 'plastron' layer of trapped air on the surface of these superhydrophobic capture surfaces is not required to enable these advantageous spreading dynamics. During experiments with reacting gas bubbles, we need to use negative pressure to actively remove this plastron layer from capture surfaces prior to testing to enable us to track the dissolution of the captured gas layer visually, which would not be feasible practically if there is already a trapped layer of air on the surface prior to the reacting gas injection. To accomplish this, we similarly tested the spreading of an air bubble surrounded by deionized water using the hierarchical *low-phi* capture surface, but this time with the plastron layer removed from the surface prior to the test. The dynamics of bubble capture and spreading are effectively equivalent for the low-phi surface with and without the plastron layer, as shown in Figure 4-3E, indicating that the presence of the plastron layer is not required to achieve the rapid and complete spreading that we plan to use to enhance absorption in a reactive bubble case.

From analyzing the images acquired during testing, we are able to track the contact line of the advancing front of the captured air bubbles to measure their velocity and compare the dynamics between samples. As shown in Figure 4-3B, all of the surfaces possessing nanoscale texture show very similar spreading dynamics, while the purely microtextured capture surface more slowly spreads the captured bubble which also is pinned before completely spreading. This underscores the requirement that nanoscale texture be present, which has been reported in prior work studying the capture of gas bubble with superhydrophobic surfaces[140]. Finally, from this data, we are able to estimate the timescales for spreading for the bubbles deduced from the velocity of the advancing

contact line during spreading. The microscale *b5* shows contact line instantaneous velocities up to 70 cm/s and an average contact line velocity of 17 cm/s ahead of being pinned. On the other hand, the *ng* and *low-phi* surfaces (with and without a plastron) show very similar spreading velocities to one another with instantaneous velocities of approximately 1.2 m/s and average velocities during the entire experiment of approximately 36 cm/s, approximately twice that of the microscale *b5* texture.

From these contact line velocities of the ng and low-phi surfaces, we can estimate the spreading timescale for these bubbles, which all lie somewhere between 1 and 10 ms. This agrees with a scaling argument balancing the hydrostatic pressure that drives the bubble into the texture against the inertia of the water that resists the spreading of the bubble. This balance causes the timescale for bubbles spreading in these cases to scale as $\tau_{spreading} \sim \frac{a^2}{(g\Omega)^{1/2}} \sim 10\ ms$ where a is the capillary length (for our case $a \approx 2.5$ mm for water), g is the gravitational constant, and Ω is the volume of the spreading bubble. This previously developed timescale agrees well with our observed experimental results and with previously reported contact line velocities of ~ 1 m/s for spreading air bubbles in water[139].

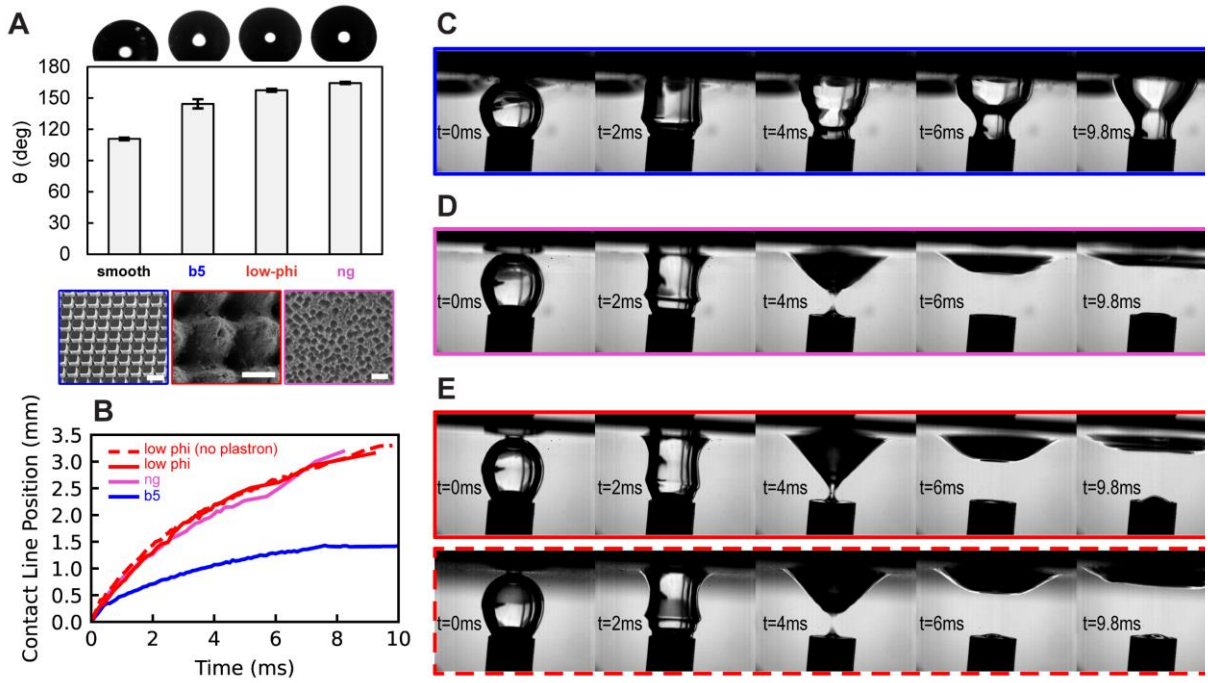

Figure 4-3. Realizing surface which rapidly and fully spread captured bubbles through their texture. (A) Top plot shows the contact angle measurements for the various capture surfaces tested using a droplet of water to measure the wetting properties relevant for the KOH solution. Bottom SEM micrographs shown for the three textured surfaces tested, b5 micropost surface in blue, low-phi laser ablated surface in red, and reactive ion etched "nanograss" nanotextured surface in pink. (B) Plot showing the contact line motion over time for an air bubble brought to the surface of the tested capture surface while surrounding in non-reacting deionized water, showing the necessity to have nanotexture to achieve rapid and full spreading, along with the fact that a trapped as layer is not required for this enhanced bubble capture to occur. (C-E) Time lapses of high-speed imaging photos showing the evolution of the contact line for the b5 micropost surface (C), the nanograss surface (D) and the low-phi surface (E). In (E), both a low-phi surface with (top) surrounded by solid red line, and without (bottom) surrounded by dashed red line.

4.4.4. Superhydrophobic Low-Phi Capture Surfaces for Rapid, Complete Absorption

Now that we have fabricated and characterized the capabilities for the nanoscale capture surfaces to successfully spread air bubbles, we next tested the capability for these surfaces to enhance the absorption of CO_2 bubbles surrounded by a 0.1 M KOH absorption solution. Given the similar performance for both *ng* and *low-phi*, the decision to use the hierarchical *low-phi* surface for absorption testing was due to its facile nature to fabricate via laser ablation and its ability to hold significantly more gas within its deeper, hierarchical texture in comparison to the purely nanoscale *ng* surfaces. An illustrative test captured using high-speed imaging is shown in Figure 4-4A. As shown, the CO_2 bubble is rapidly captured and fully spread over a timescale of ~10 ms. Throughout the spreading, the CO_2 bubble is being absorbed as it reacts with the hydroxide solution to form potassium bicarbonate. Critically, the timescale over which the bubble has been entirely absorbed has been decreased from ~10s of seconds for a similarly sized captive bubble case to plateau and cease absorption to ~100 ms for the spreading case for complete absorption. As a result, the average reaction rate for these bubbles is approximately 2 orders of magnitude larger than the average reaction rates for the first 20 seconds for the captive bubbles tested for all of the non-nanoscale capture surfaces, as summarized in Figure 4-4B. This increase in magnitude of average reaction rate is well-captured by the developed model, which predicts this 2 order of magnitude increase relative to the non-spreading bubble case, as shown in Figure 4-4C.

The first feature of spreading the CO_2 bubble in this way which enables this enhancement in absorption of CO_2 is the matching of the timescales of spreading of the bubble with the timescale of the reaction taking place. The timescale for the reaction can be derived from the bulk concentration of reactant in solution and the reaction rate coefficient $\tau_{rxn} \sim (c_{bulk,\,OH^-}\, k)^{-1} \approx$

1.7 ms. When this is compared with the timescale of spreading introduced in the previous section, we arrive at a modified Damköhler number, Da, for this situation, representing a dimensionless number comparing the timescale of the bubble spreading against the timescale for the reaction to occur.

$$Da = \frac{\tau_{spreading}}{\tau_{rxn}}$$

In our scenario, by matching the order of the timescales of spreading and reaction to be between 1 and 10 ms, the spreading bubble enables CO_2 to be continuously supplied to a new interface of reacting gas and liquid absorbent which minimizes and resets the diffusion boundary layer. Minimizing the extent to which a boundary layer is maintained enables the reaction to persist at the highest rates while the bubble is spreading. Secondly, the nature of the spreading itself increases the surface area per unit volume of gas available for reaction relative to the spherical bubble case, which maintains a surface which is closer to the minimal area per unit volume. As the shown in Figure 4-4A, this enlarged surface area for interaction is maintained relatively constant after the bubble has spread into the texture. This is advantageous relative to the case of a bubble shrinking during absorption, which has its surface area decrease as the square of the radius of the bubble. Finally, the rapid nature of complete reaction of the CO_2 with the hydroxide also enables the bubble to be completely absorbed and not present the plateauing behavior which persisted for all of the non-spreading cases tested. The aggregation of product formation at the surface of the bubble interface will occur on a timescale that is slower than the reaction itself, allowing the spreading bubble to react quickly enough to avoid product aggregation and be completely absorbed.

Finally, there is an interesting reversal in the overall trend in the average rates of reaction and the initial bubble size between the bubble and spreading bubble cases. For all the non-spreading bubble capture surfaces tested, there is a general trend for larger bubbles to be absorbed at a larger rate driven by their larger available area to react in comparison to smaller bubbles, as shown in Figure 4-4B. However, this tendency is reversed in the case of spreading bubble absorption as the bubbles with the highest rates tested tended to be the smallest. Since spreading has significantly enhanced the surface area of these smaller bubbles, the fact that there is a smaller volume of gas to react allows these bubbles to react quickly enough to minimize the impacts of diffusion boundary development relative to their larger spreading counterparts, allowing them to be absorbed extremely rapidly. For example, Figure 4-4D shows a bubble with a radius of approximately 500 μm, which can be absorbed rapidly over the course of only a few milliseconds, having successive bubbles repeatedly injected over time at this rate.

The conceptual embodiment of an application for surface enhanced direct injection of gas for absorption is shown graphically in Figure 4-4E. An array of small needles rapidly injecting gas bubbles into the capture surface, as shown in Figure 4-4E (left), spaced sufficiently apart such that neighboring needles' spreading bubbles do not interact to a significant degree. If we envision a small-scale absorber of this type with a 20 x 20 array of injection needles (400 total needles), a total size of approximately 10 cm x 10 cm x 2.5 cm would be required. When we normalize the average rate for this type of an absorber by the volume the reactor actually takes up, we arrive at a reactor volumetric average reaction rate of ~ 1 kg/s/m^3, as shown in Figure 4-4E (right). For a commercial reference, the absorption tower of one of the largest post-combustion carbon capture projects in the world, Peta Nova, was used. This absorption tower absorbs CO_2 from the exhaust of a co-located coal-fired power plant near Houston, Texas in the United States with a capacity of

1.6 Mt CO_2 annually[145]. As a result, Petra Nova's absorption tower represents the epitome of the advantages of scale that can be achieved when large-scale absorption towers are utilized for gas separations. However, it is generally difficult to scale down these types of technologies and they are therefore not well-suited for distributed or small-scale and modular absorption modes. Given the simple nature of the operation of the surface enhanced direct injection modality demonstrated here, we aimed to motivate some of the potential advantages of these types of systems for distributed and small-scale, modular operations. The same volumetrically normalized average reaction rate for Petra Nova is approximately 3 orders of magnitude lower than that for the surface enhance direct injection embodiment envisioned here.

Of course, this comparison is merely to motivate the advantageous nature of a surface enhanced direct injection methodology to enable high performance absorbers that would work well at a small scale, and is not a suggestion that these sorts of systems would replace existing large scale absorption tower system applications. In reality, the scenarios between the absorption demonstrated here using a pure CO_2 gas being absorbed by a moderately alkaline solution of KOH cannot be compared directly to the scenario at Petra Nova where a gas mixture is being treated with an amine-based absorber liquid at elevated temperature and pressure. However, it is worth highlighting the enhanced reaction rates achieved here using a relatively moderate alkalinity in having the KOH concentration of 0.1 M, which could be advantageous when compared with higher concentration absorber units which risk material corrosion and damage in much more alkaline environments, which require more strict material considerations. In the future, it will be of interest to extend the systems and tests demonstrated here to include multi-component gas mixtures, rather than a pure gas, to increase the application relevance to absorption units for industrial applications in separations and chemical scrubbing.

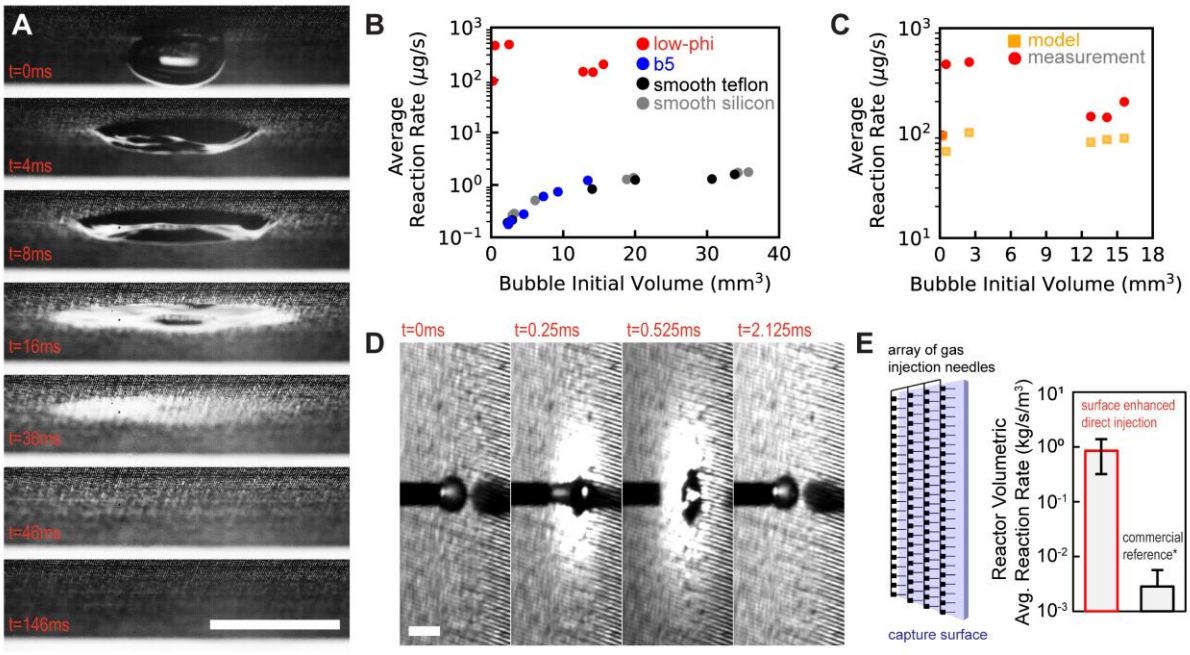

Figure 4-4. Ultra-fast absorption of carbon dioxide bubbles summarized using the low-phi capture surface to enhance reaction rates and allow for complete absorption. (A) Time lapse images take from high-speed imagery showing the capture and absorption of a CO2 bubble into the superaerophilic low-phi surface. Scale bar represents 5 mm. (B) Average reaction rates for all the various surfaces tested, showing a two order of magnitude improvement in the reaction rate for low-phi spreading bubble case in comparison with b5 micropost textured, smooth teflon, and smooth silicon capture surfaces. Note that average reaction rates shown for all surfaces other than low-phi represent the initial 20 s of absorption, as the tested bubbles plateaued in absorption following at some point after this time and were never completely absorbed like the low-phi case. (C) Average reaction rates shown for the low-phi spreading bubble case measurements in comparison to the predictions from the model, which are in good order of magnitude agreement to show the improvement relative to the non-spreading bubble case. (D) Time lapse, high-speed imaging of the smallest bubbles directly injected into a low-phi capture surface showing total absorption of ~1 ms for these small bubbles to motivate the embodiment of small-scale and modular high-performance absorption suing this surface enhanced direct injection mode of absorption. (E) Schematic description of an array of needles as shown in (D) to create a modular embodiment of the surface enhanced direct injection absorption system, left. At right, shows the volumetrically normalized reaction rates which take into account the size occupied by the absorption reactor for the envisioned small-scale surface enhanced direct injection absorber in comparison to a commercial reference, which here is shown as Petra Nova's absorption tower, which is a large-scale post-combustion carbon capture facility in Texas, USA.

4.5. Conclusions

In summary, we have experimentally demonstrated and numerically modelled the enhancement of CO_2 bubble absorption by using advantageous surface interactions to spread the bubble into nanoengineered superhydrophobic bubble capture surfaces. By doing so, we have increased average reaction rates for the CO_2 absorption process by more than 2 orders of magnitude in comparison to a non-spread bubble case. The critical importance of the presence of nanoscale surface roughness was demonstrated and surfaces capable of fully spreading CO_2 bubbles on a timescale commensurate with the absorption reaction timescale were shown. While non-spreading bubbles tend to show smaller reaction rates for smaller bubbles due to decreased surface area, spreading bubbles appear to invert this trend where the spreading smallest bubbles showed the largest average reaction rates for complete absorption due to their small volumes being spread to large surface areas. All spreading bubbles allowed for complete absorption of the gas to avoid the "plateauing" effect observed for all the non-spreading bubbles and blisters tested. Finally, direct injection of gas bubbles was envisioned as an advantageous method for absorption relative to large-scale absorption towers on a volumetric basis, which motivates this sort of motif for use in modular and distributed absorption applications, where centralized large-scale absorption methods cannot be practically or economically achievable.

5. Transient Effects Caused by Gas Depletion during Carbon Dioxide Electroreduction

5.1. Summary of Concept and Contributions

The novel use of carbon dioxide (CO_2) electroreduction to generate carbon-based products which do not contribute to the greenhouse effect has promoted the vision of carbon dioxide as a renewable feedstock for future clean fuel production. Depending on the material choice for the electrocatalysis, a certain variety of products is expected from the carbon dioxide reduction reaction (CO2RR). However, as the CO_2 concentration in areas close to the working electrode (relative to the diffusive boundary layer) decreases as it is being consumed and transformed into other products, the generation of H_2 is favored to the detriment of CO_2 electroreduction. Therefore, the extent to which H_2 is produced can be used as a metric to evaluate the efficiency of CO2RR. This article proposes a model that accounts for the modes in which aqueous gas depletion evolves over time and affects the long-term CO_2 electroreduction and the corresponding pH evolution near the electrode's surface. For the latter, two main contributions are distinguished: gas depletion due to CO_2 consumption and ion generation in areas close to the electrocatalyst surface. pH is then suggested as an accurate and indirect means to measure CO_2 concentration in a liquid electrolyte. We conclude that CO_2 depletion causes a strong decay in the electrochemical reaction efficiency. In the end, we discuss several methods which may delay the onset of the adverse effects caused by gas depletion, such as the utilization of pulsed electroreduction, cycling the applied current to electrodes on and off periodically.

5.2. Introduction

When the United Nations reconvened in 2015 for their latest meeting held in New York under the project "Sustainable Development Summit", the participant countries released the 2030 Agenda for Sustainable Development with a final target to reduce CO_2 emissions into the atmosphere[146]. Current lines of research not only focus on lowering those emissions[147–149] but intend to capture and/or store gaseous CO_2 underground,[150,151] dissolve it into ocean water[152] (with the associated controversial problem of acidification[153,154]), and/or convert it into other useful sustainable products[155–157].

Regarding the last approach, CO_2 can be converted by electroreduction into other carbon-based products, such as carbon monoxide (CO),[158,159] methane [160], formate[161], ethanol[162], propanol[163], and other valuable C_2 and C_3 products[164] such as n-propanol, acetaldehyde, and acetone. This conversion is known as carbon dioxide reduction reaction (CO2RR) and is a process which has been studied since the beginning of the 20th century[165] and has attracted renewed interest since the late 1980s[166].

The selectivity of products generated from CO2RR varies drastically depending on the chosen electrocatalyst's chemistry and structure. Indeed, there is a wide variety of metals which can be used in CO2RR, with some of them being very selective to liquid products (such as Pb[167,168], In[167,169], Hg[167,170], and Sn[171]) and some others to gaseous products (such as Au[172–174], Ag[174,175], and Zn[176,177]). However, the majority of electrocatalysts provide a range of both liquid and gaseous products. Among them, copper (Cu) is the most widely studied electrocatalyst material due to its accessibility, affordability and, most importantly, large variety of products which can be generated by CO2RR[178,179]. In the present study, we perform our experiments with the so-called "coinage

metals", i.e. Au, Ag, and Cu. This choice is primarily motivated by the vast research already available and their selectivity to produce CO (for Au and Ag) or various C-based gas and liquid products (for Cu).

Nonetheless, there is a drawback which is implicit to CO2RR and which affects the overall efficiency of the conversion process: the coevolution of H_2 from water electrolysis. While some electrocatalyst materials will have a higher propensity for H_2 formation (such as Pt[180,181] or Fe[182]), there is inevitably a certain partial current dedicated to split the aqueous electrolyte[183] in which CO_2 is dissolved for most metallic electrocatalysts, including Au, Ag, and Cu. How much current is invested into this unintended side-reaction depends on various factors, such as reactant concentration, pH, pressure, temperature, humidity, and purity of the working electrodes[179]. A summary of previously reported CO2RR performances for the particular coinage metal electrocatalysts focused on here is shown in Figure 5-1. Figure 5-1a-c clearly show that, depending on the specific conditions in which the experiments are conducted, the magnitude of partial current dedicated to effectively generate C-products (or equivalently, the Faradaic efficiency $F_{eff} = i_{partial}/i_{total}$, where $i_{partial}$ is the partial current dedicated to the generation of a specific product and i_{total} is the total current) can vary significantly. For these cases, the measurement of the H_2 coevolution provides a satisfactory means to qualify the efficiency of CO2RR. In this article, we focus on two major indicators of chemical efficiency: the CO_2 concentration close to the electrode[184] and the pH of the system[185]. Both effects are interconnected, since higher CO_2 concentrations imply lower bulk pH[186]. On the other hand, the production of ions during CO2RR results in a higher pH in areas close to the electrodes[187]. Those two effects combine to have a significant influence on the production of C-based products during CO2RR[179,185,188,189].

The problem related to mass transfer phenomena has been approached from several perspectives. As compared to flat electrodes, nano/microstructured materials have been proven to trap CO_2 gas within the surface topology to achieve locally higher reactant concentration and increase the reaction efficiency [159,190–195], as depicted in Figure 5-1a-c and in the sketches in Figure 5-1d,e. Most recently, solving this mass transport limitation has been primarily approached by using a novel electrode design: the gas diffusion electrode (GDE)[196,197]. This electrode architecture approaches the problem of reactant (gas) accessibility to the electrocatalyst by utilizing porous materials as electrodes[198,199] and allowing the gas to diffuse through their bodies and readily react at the three-phase interface with the electrolyte[190,200]; see Figure 5-1f. The novelty in its architecture resides in the evident drop in the thickness of the mass-transfer boundary layer near the electrode, from 60 to 160 μm for a typical H-cell to 0.01−10 μm for a flow cell[201]. GDEs have been reported to generate a wide variety of different products, and most importantly, the highest current densities j_{total} for CO2RR[196,198,200,202]. In early reports, the current density was particularly high as a result of using the projected surface area of the electrode to obtain the current density[196,203]. Recently, results report the current density using the electrochemically active surface area, which for a porous material is the total area that actually participates in the reaction[200,204]. In either case, current densities for GDEs are significantly higher than those for plain or nano-/microtextured electrodes. Together with the high production rates from CO2RR, GDEs are also extremely well-suited to lower the partial current dedicated to H_2 coevolution. Still, understanding and modeling how electrodes consume CO_2 around their surroundings and what are the direct consequences of such concentration depletion in the long-term reactions are critical for enabling CO2RR technologies to become commercially viable. This article aims to provide an analytical

framework for modeling how the reactant concentration is affected by the ongoing chemical reaction and the consequences gas depletion has on the chemical efficiency.

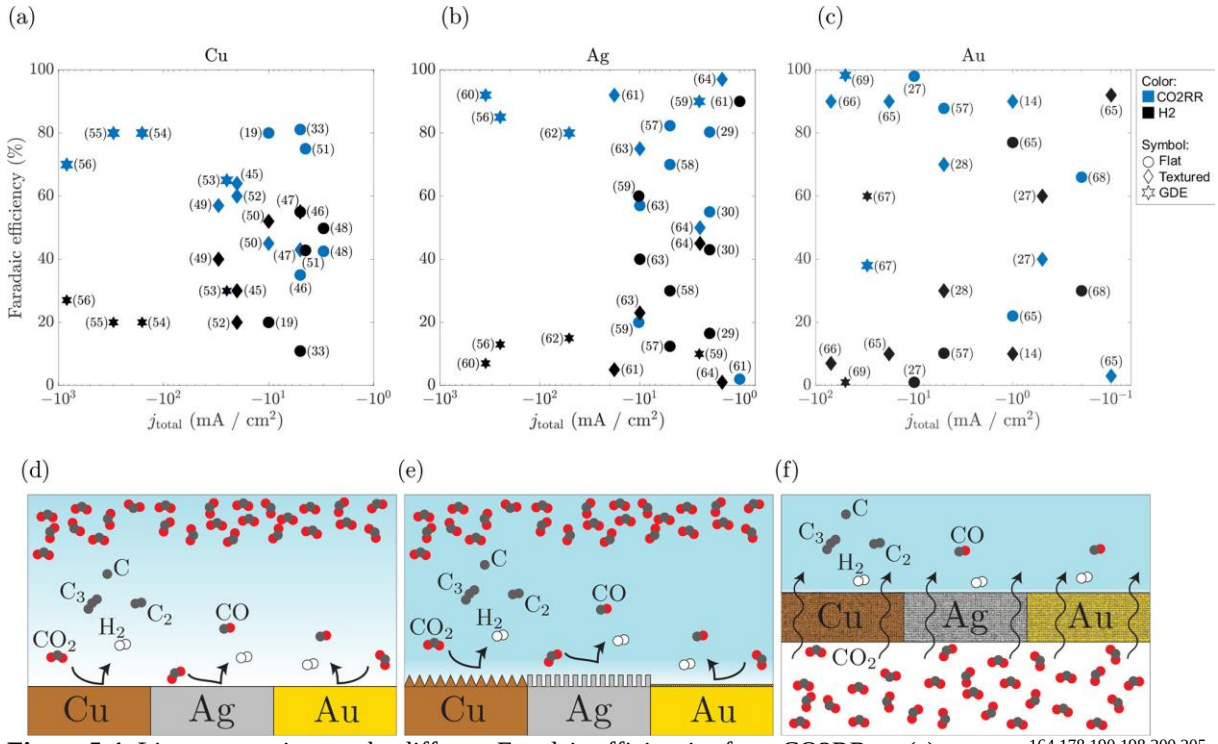

Figure 5-1. Literature review on the different Faradaic efficiencies from CO2RR on (a) copper, [164,178,190,198,200,205–213] (b) silver [174,175,191–193,200,214–218] and (c) gold electrodes [159,172,173,194,195,214,219–221] as a function of the total current density j_{total}. Blue symbols represent the Faradaic efficiency of C-based products on flat surfaces or foils (circles), nano-/microstructured surfaces (diamonds) or GDEs (stars). The matching black symbols represent the Faradaic efficiency of the H_2 co-evolution process. Take into consideration that, whereas Cu produces a wide variety of C-products, Ag and Au are very selective to CO. The data is very scattered, an indication of the sensitivity of the CO2RR process. Generally, nano-/microstructured electrodes show a better performance while maintaining the same order of magnitude for the current density. GDEs are the best approach to overcome the mass transfer limitations: they obtain the best performance with the highest current densities. (d-f) Sketches of the different ways in which CO_2 may be provided to (d) flat (circles in subplots (a-c)) and (e) nano-/microtextured (diamonds) surface electrodes, and (f) GDEs (stars). The gradient in blue color above the electrodes indicates the level of aqueous gas depletion within the electrolyte, which is significantly higher in the case of headspace delivery on flat samples (d) as compared to textured ones (e) or GDEs (f).

5.3. Experimental Methods

The experiments were carried out using a standard electrochemical setup consisting of an H-cell with two compartments separated by a Nafion membrane (Fuel Cell Store, refer to Appendix §7.3.1, for the activation and cleaning process), as shown in Figure 5-2. The cell had been previously cleaned in a piranha bath (one part of hydrogen peroxide, H_2O_2, and three parts of sulfuric acid, H_2SO_4) overnight and rinsed thoroughly with DI water to ensure it is free of contaminants. The decision to carry out experiments on this conventional architecture is justified because H-cells offer a simplified and controlled setup to test the mass transport depletion effects. Indeed, mass transport problems in these systems will be exaggerated relative to those for more modern GDE architectures, where depletion is remarkably compensated by gas diffusion through the surface of the electrode. This diffusion constraint within the H-cell facilitates the focus on a specific phenomenon which plays a major detrimental role on the performance of any electrolyzer. On the cathodic half of the cell, the working electrode was based on a copper, silver, or gold wire of radius r_e = 0.25 mm and 99.999% purity (Sigma-Aldrich), which was cut into a length of L = 15 cm and turned into a coil of ten spirals. The electrocatalysts were electrochemically polished/cleaned prior to each experiment to ensure optimal conditions for a proper electroreduction process and avoid limiting effects by the presence of oxides, nitrides, sulfides, or other possible isolating layers (see Appendix §7.3.2, for the preparation of electrocatalysts). A reference electrode was positioned at all times close to the working electrode. We chose an Ag/AgCl reference electrode (Pine Research Instrumentation) to perform our experiments. Its potential E as compared to a reversible hydrogen electrode (RHE) can be related by using the Nernst equation as follows[222–224]:

$$E_{RHE} = E_{Ag/AgCl} + E^0_{Ag/AgCl} + 0.0591 \times pH \quad (1)$$

where $E^0_{Ag/AgCl}$ = 0.1976 V is the reference potential vs Ag/AgCl at 25 °C. Unless indicated otherwise, every potential in this chapter, including the corresponding appendix for this chapter, will be referred to this Ag/AgCl electrode. On the anodic half of the H-cell, a Pt wire counter electrode completes the electric circuit. A 35 mL portion of 0.1 M KOH (pellets of ≥85% purity, Sigma-Aldrich) solution in DI water was utilized as electrolyte per half of the H-cell. This solution achieves high ion conductivity within the electrolyte while maintaining high CO_2 dissolution capacity (higher salt concentration provides higher ion transport to the detriment of the maximum CO_2 saturation concentration)[212]. Prior to every experiment, the electrolyte was saturated with pure CO_2 (Airgas) by bubbling the gas into the liquid for more than 30 min, and therefore, turning the final electrolyte solution into 0.1 M $KHCO_3$. To confirm the proper saturation level, a pH meter (HI 5222, Hanna Instruments) was used to actively measure the pH of the solution: from an initial pH ~ 13, a saturation level at standard conditions was reached when pH ~ 6.79[225].

During experiments, CO_2 is fed to the cathodic headspace at all times to keep a constant saturated CO_2 environment. Note that the electrolyte is not replaced at any time during experiments, limiting the replenishment of CO_2 in the electrolyte to the natural dissolution process that occurs at the free surface between the gas headspace and electrolyte. For the sake of studying the different parameters which may play a significant role in the long term CO2RR evolution, we performed chronopotentiometry (CP) and chronoamperometry (CA) experiments with a potentiostat (Bio-Logic SAS, model VSP 1851), applying a specific current and measuring the potential evolution or establishing a certain constant potential and letting the current freely evolve, respectively. pH measurements corresponding to those experiments were recorded by introducing the pH meter in areas far away from the working electrode, i.e. ≥5 cm away, and in its close vicinity (relative to the diffusive boundary layer), i.e. ≈1 cm from its surface. The gaseous products

obtained from CO2RR were measured every 14 min using a gas chromatographer (GC Agilent Technologies 7890B), which had been previously calibrated using a customized gas precision calibration mixture (Gasco and Shopcross). Liquid products were sampled into 700 μL NMR glass tubes and mixed with 35 μL 100 mM DMSO and 100 mM phenol in D_2O standard (for calibration purposes). The samples were analyzed by nuclear magnetic resonance (NMR instrumental Bruker 402), and the data was interpreted using the software MestReNova.

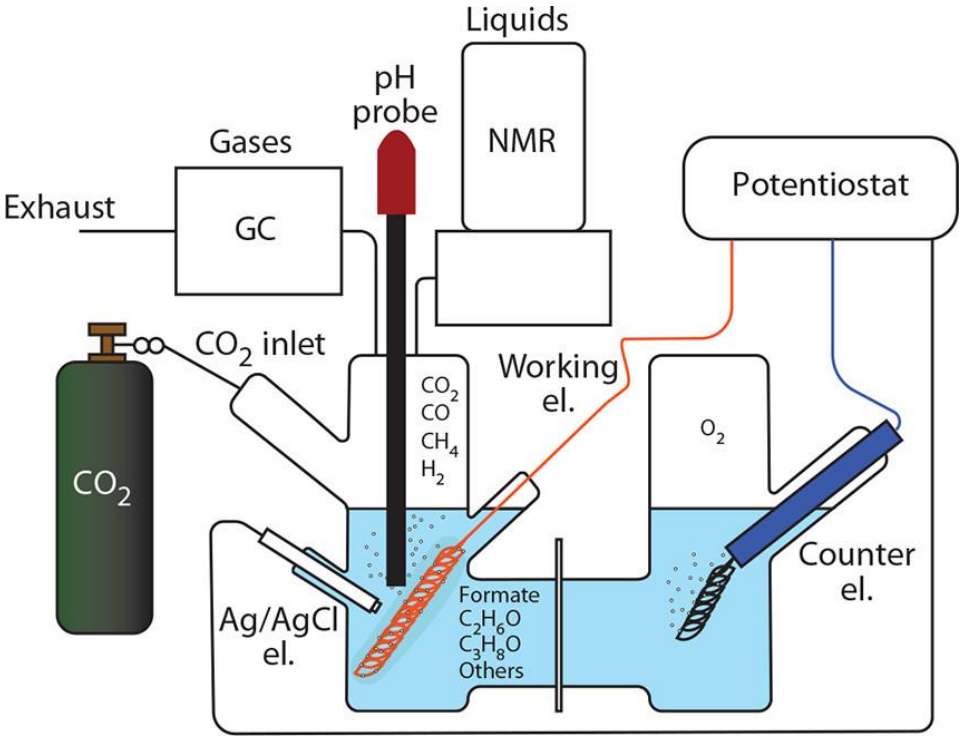

Figure 5-2. Scheme of the electrochemical setup. On the left side of the H-cell, a working electrode (orange) is immersed into an aqueous solution of 0.1 M KOH saturated with CO2 (i.e. 0.1 M KHCO3). An Ag/AgCl reference electrode (white) is positioned through a lateral opening in its close proximity. CO2 is fed to the cathodic headspace at all times during experiments and is used both to keep a constant saturated CO2 environment and to serve as flowing gas to bring the gaseous products into the gas chromatographer (GC). The liquids are collected and analyzed by nuclear magnetic resonance (NMR). A pH probe is located in the vicinity of the working electrode and measures pH at all times. On the right side of the Hcell, a Pt counter electrode (blue) is immersed to complete the electrical circuit. Both halves are separated by a Nafion membrane.

5.4. Results and Discussion

In the following, the results from our CO2RR experiments will be reported dedicating specific sections to the cases of Ag and Au electrocatalysts (selective to CO) and to the case of Cu electrodes (which generate a wide variety of components). Table 5-1 includes the standard equilibrium potentials to generate such products[166,179].

5.4.1. CO_2 Electroreduction on Ag and Au Electrocatalysts

As previously stated, CO2RR on Ag and Au electrodes is very selective to CO and is commonly accompanied by H_2 coevolution. Nonetheless, liquid products such as formate ($HCOO^-$) may also be generated, especially in the case of Ag. The maximum F_{eff} measured for such liquid products was always lower than 5%, which is in agreement with previous literature[214]. In addition, this F_{eff} was obtained within the first 10 min of reaction, decreasing drastically within the first half hour and practically disappearing within the first hour of experiments. Therefore, we can safely assume that our CO2RR experiments on Ag and Au primarily generated gaseous products, more specifically CO and H_2. Note that, provided that the electrocatalysts are in good condition, changing the electrolyte solution at the end of each experiment is enough to obtain reproducible results.

This simplification facilitates the interpretation of results since $F_{eff,CO} + F_{eff,H_2} \approx 1$, which is directly translated to $i_{partial,CO} + i_{partial,H_2} \approx i_{total}$. Partial current is readily associated with mass by Faraday's law of electrolysis[226]:

$$i = \frac{mFz}{Mt} = \frac{nFz}{t} \quad (5.2)$$

where m is the mass of the product, F = 96 485 C mol^{-1} is Faraday's constant, z is the valence of the reaction, M is the molecular weight of the product, n the corresponding number of moles, and t the reaction time. This way, we can directly write:

$$i_{partial,CO} = \frac{2m_{H_2}F}{M_{H_2}t} = \frac{2n_{H_2}F}{t} \quad (5.3a)$$

$$i_{partial,CO} = \frac{2m_{CO}F}{M_{CO}t} = \frac{2n_{CO}F}{t} \quad (5.3b)$$

Very conveniently, the valence for the CO and H_2 formation reaction is the same, z = 2. We can therefore report our results in a compact straightforward way: the ratio between the two partial currents, i.e. the ratio between the two Faradaic efficiencies:

$$\frac{F_{eff,CO}}{F_{eff,H_2}} = \frac{i_{partial,CO}}{i_{partial,H_2}} = \frac{n_{CO}}{n_{H_2}} \quad (5.4)$$

The ratio between the two molar quantities is a value that can be directly measured using the GC. We represent our experimental results depending on the total current density $j_{total} = i_{total}/A_e$ (where $A_e = 2\pi r_e L$ is the area of the working electrode) in Figure 5-3. There is a common trend to be appreciated for all the cases, independently of the applied current density or the material: the ratio between the Faradaic efficiencies of CO and H_2 decreases over time. In addition, higher j_{total} generally causes a faster decrease in the ratio. To facilitate the interpretation, we have defined that a "minimally viable CO2RR reaction" generates at least the same amount of CO and H_2 on a molar basis, i.e. $F_{eff,CO}/F_{eff,H_2} = 1$. A horizontal line indicating this threshold has been indicated in both plots in Figure 5-3.

There are nonetheless some particularities to the Ag and Au electrodes. For the former (Figure 5-3a), it seems that low total current density, i.e. j_{total} = −0.422 mA cm^{-2} , causes the overall

reaction to be very inefficient, as the ratio $F_{eff,CO}/F_{eff,H_2}$ is always below the minimally viable ratio of 1. A possible explanation may relate to the sensitivity of the electrode material. Referring to the cleaning process for Ag electrodes (see Appendix, §7.3.2), we note that to achieve a proper reaction, the Ag coil needs to be released from sulfides and oxides that may be deposited or created on its surface due to its exposition to the open air. Even though the electrode may be clean at the starting point of the reaction, the low current density applied (with a consequent low potential) may impede a proper electroreduction as long as there is a minimal amount of residual sulfides or oxides. This effect clearly disappears at higher current densities, since these can also contribute to the Ag cleaning process during the first minutes of reaction. This fact could explain why higher j_{total} achieve a higher Faradaic efficiency ratio at the start of the reaction. In addition, the point where the curves cross the defined "minimally viable threshold" seems to coincide at an approximate time of t ≈ 90 min. Looking closer into the figure, we find that this point occurs at slightly longer times for the cases with lower j_{total}.

The trends of $F_{eff,CO}/F_{eff,H_2}$ are distinctly different for the Au electrode, Figure 5-3b. As already mentioned in the Appendex (see Appendix, §7.3.2), Au is a very stable material which does not easily form oxides, nitrates, or sulfides that may be deposited on its surface. The cleaning procedure is significantly simpler and causes less stress on the material. Therefore, "minimally viable" results are obtained even at very low j_{total}. However, the highest ratio is achieved at intermediate j_{total} within the first 10 min of reaction. This fact is rapidly compensated for by a faster consumption of dissolved CO_2, i.e. faster depletion, at higher j_{total}. Thus, the threshold crossing point is found at longer times for lower j_{total}.

Indeed, there is a general behavior that can be distinguished for both Ag and Au: higher j_{total} causes a faster CO_2 consumption in areas close to the electrode in such a way that diffusion alone cannot counteract. As a result, the available CO_2 for CO2RR is diminished over time, remarkably affecting the long-term efficiency of the chemical reaction, which dedicates more and more current over time to dissociate water and form H_2 instead of CO2RR.

Table 5-1: Standard equilibrium potentials for all the reactions occurring during CO2RR. The potentialsare referred both to RHE (Reversible Hydrogen Electrode) and Ag/AgCl electrode for easiness in the direct interpretation of our results.

Product	**Reaction**	**Equilibrium potentials *E* (V) vs RHE**	**Equilibrium potentials *E* vs. Ag/AgCl and pH = 6.79**
Hydrogen	$2H^+ + 2e^- \rightarrow H_2$	0	-0.5989
Carbon monoxide	$CO_2 + 2H^+ + 2e^- \rightarrow CO(g) + H_2O$	-0.106	-0.7049
Formate	$CO_2 + H_2O + 2e^- \rightarrow HCOO^-(aq) + OH^-$	-1.078	-1.6769
Methanol	$CO_2 + 6H^+ + 6e^- \rightarrow CH_3OH(aq) + H_2O$	-0.030	-0.6289
Methane	$CO_2 + 8H^+ + 8e^- \rightarrow CH_4(g) + 2H_2O$	0.169	-0.4299
Acetate	$2CO_2 + 5H_2O + 8e^- \rightarrow CH_3COO^-(aq) + OH^-$	-0.360	-0.9589
Ethylene	$2CO_2 + 12H^+ + 12e^- \rightarrow CH_2CH_2(aq) + 4H_2O$	0.064	-0.5349
Acetaldehyde	$2CO_2 + 10H^+ + 10e^- \rightarrow CH_3COH(aq) + 3H_2O$	0.060	-0.5389
Ethanol	$2CO_2 + 12H^+ + 12e^- \rightarrow C_2H_5OH(aq) + 3H_2O$	0.084	-0.5149
Acetone	$3CO_2 + 16H^+ + 16e^- \rightarrow CH_3COCH_3(aq)\ 5H_2O$	0.090	-0.5089
1-Propanol	$3CO_2 + 18H^+ + 18e^- \rightarrow C_3H_7OH(aq) + 5H_2O$	0.100	-0.4989

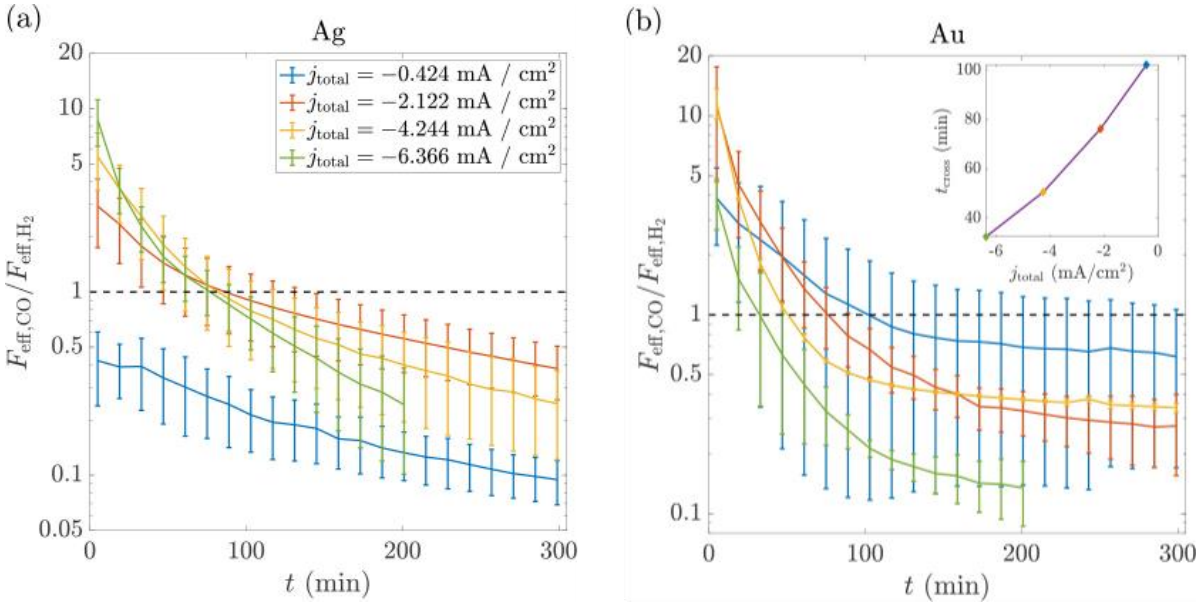

Figure 5-3. Ratio of the Faradaic efficiencies of CO and H_2 as a function of time for different total current densities for the cases of (a) silver and (b) gold working electrodes. Error bars correspond to the standard deviation across four independent experimental replicates. The color scheme is equivalent for the two plots. The horizontal black dashed line at unity indicates the threshold for a minimally viable CO2RR reaction. The inset in (b) shows the time it takes to cross that threshold as a function of the total current density j_{total} for the case of Au.

5.4.2. CO_2 Electroreduction on Cu Electrocatalysts

Cu is the most widely used material to perform CO2RR due to its accessibility and the large variety of liquid and gaseous products it can generate. However, this richness in production comes with a sensitivity of the electrocatalyst to many external factors (such as pH, temperature, pressure, and purity) which hinder the reproducibility of results if those parameters are slightly affected[179]. The cleaning and preparation process detailed in the Appendix (see Appendix, §7.3.2) is therefore of extreme importance prior to performing experiments. Again, provided that the electrocatalyst is in good condition (i.e., no presence of oxides), changing the electrolyte solution at the end of each experiment is enough to obtain reproducible results. It has been proven that the higher the concentration of CO2 in areas close to the electrode, the richer the number of products from CO2RR[194] and the higher the probability of such being high-carbon products (C_{2-3})[227]. For those to be accessible, both j_{total} and the potential E at which the reaction occurs need to be optimized for the products to be generated. The standard potential to perform CO2RR in an electrochemical H-cell using a Cu electrode has been reported to be ERHE = −1.1 V,[178] which is equivalent to EAg/AgCl = −1.7 V using Equation (5.1). After manually accounting for iR compensation, the applied potential at all times for all our chronoamperometry experiments was E = −1.72 V. According to Table 5-1, the selected potential is enough to allow for the production of high-carbon products. To guarantee that we fulfill the conditions to generate such a variety of products, we used potential control instead of current control as done in the previous subsection (in the cases of Ag and Au, the selectivity toward CO is so high that the energetic criteria to generate this gas was always achieved even in the cases with the lowest j_{total}). The results are reported in Figure 5-4 (the calculation of Faradaic efficiencies F_{eff} is explained in the Appendix, §7.3.3). Several findings can be extracted from Figure 5-4a. First, there is a clear tendency that has been already

reported from previous results: H_2 coevolution is favored over time due to CO_2 depletion in areas close to the electrode. Note that the stacked Faradaic efficiencies can be smaller or larger than the ideal mathematical value of unity. This is due to the different methodologies used to calculate the partial currents: gases are reported using the GC and liquids are treated with NMR. However, it is generally accepted that total additions up to ±20% above or below unity are admissible. Figure 5-4b indicates the evolution of the ratio between the Faradaic efficiencies of all C-products and H_2. Similarly, to the cases of Ag and Au, the reaction remains viable, i.e. over the previously defined threshold, for the first 100 min, after which H_2 coevolution governs the reactions and CO2RR is seriously compromised. In addition, gas depletion not only increases the coevolution of H_2, but also affects the generation of high-carbon products. As shown in Figure 5-4c-e, high carbon products, such as acetone, propanol, and ethanol, peak at approximately 20 min of reaction and then decrease as compared to other low-carbon ones, such as formate or CO. High-carbon gaseous molecules, such as ethylene, show a short time lag to the onset of production, reaching a maximum and then slowly decreasing over time. This trend toward lower carbon content as the reaction proceeds over time can be explained by the conventional higher equilibrium potentials to generate high carbons and the fact that the pH at the electrode is increasing over time (see next subsection). This last point implies that, as far as the electrode is concerned, a less cathodic potential is being applied according to Equation (5.1). In general, we can visualize a higher production of high-carbon products when the CO_2 concentration close to the electrode is at its maximum, decreasing drastically over time. This is shown in Figure 5-4e as C_2 and C_3 partial currents exceed those of C_1 and H_2 at the beginning of the reaction but rapidly invert as the long-term reaction continues.

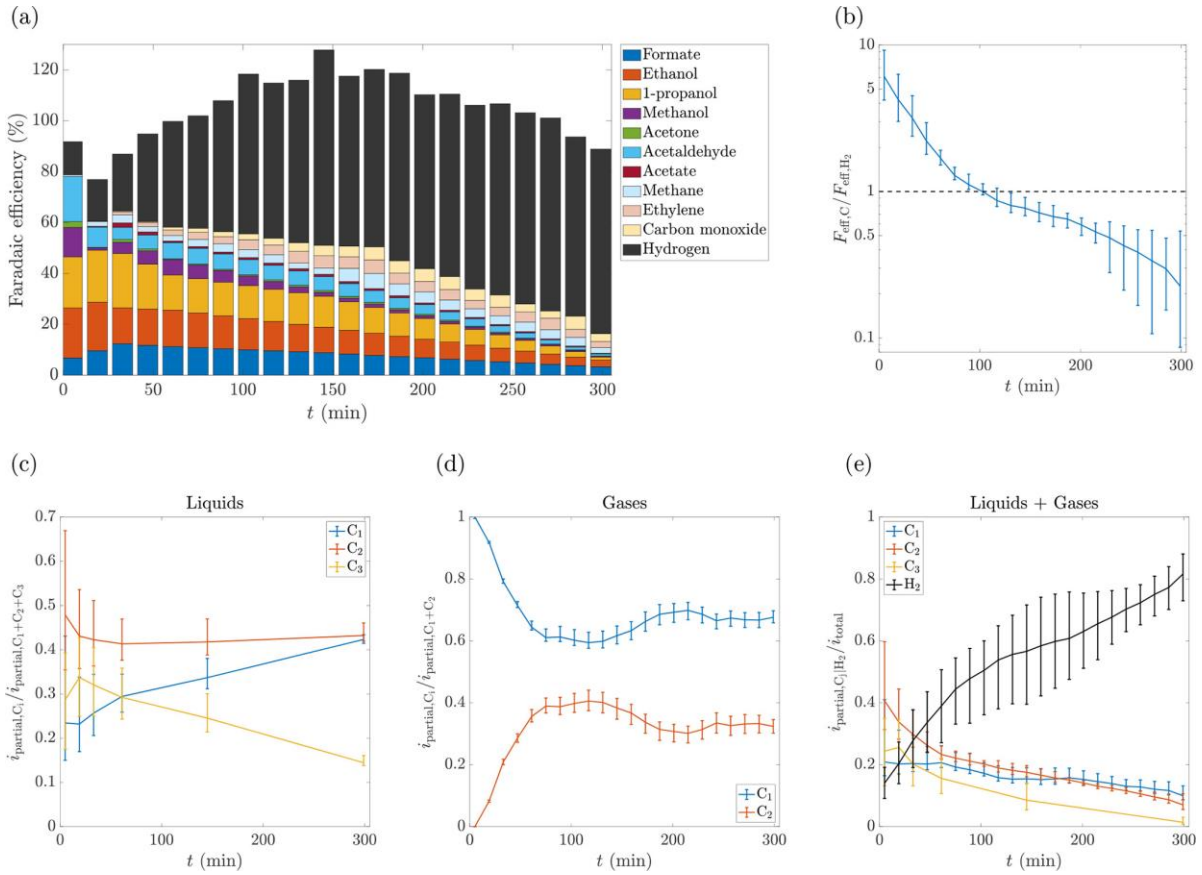

Figure 5-4. (a) Stacked bar plot of the Faradaic efficiencies of the different products obtained during CO2RR on Cu working electrodes. We highlight the contribution of H2 co-evolution in black color, to emphasize the detrimental effect that CO_2 depletion in areas close to the reacting sites causes on the overall chemical reaction efficiency over time. Note that results can add up to a total Fe > 1 due to the different methodologies in the calculation of liquid and gaseous products. (b) Ratio between the Faradaic efficiencies of the sum of C-products and H_2. The threshold for a 'minimally viable reaction' is indicated as a dashed black line and crossed after approximately 100 min of reaction time. (c, d) Proportion of C_1, C_2 and C_3 products relative to the total amount of carbon-based products generated during CO2RR in (c) liquid and (d) gaseous form. Over time the production of single-carbon products drastically increases to the detriment of high-carbon ones. (e) Total evolution in time of C_1, C_2, C_3 and H_2 products. The H_2 co-evolution benefits from the CO_2 depletion as the reaction carries on over long times, as opposed to carbon products, particularly high-carbon ones, which are dramatically affected and diminished. Error bars for plots (b) - (e) correspond to the standard deviation across four independent experimental replicates.

5.5. Mathematical Model for CO2 Concentration and Depletion

In this subsection, we report the mathematical analysis to understand how the concentration of CO_2 can be measured based on the fundamental chemical equations for equilibrium and the pH of the solution prior to experiments. We then develop a simplified model to account for the gas depletion in the areas surrounding the electrodes.

5.5.1. Equilibrium Model in the Presence of CO_2 in Moderate Aqueous Solutions of Moderate Ionic Strength

The equilibrium equations for the dissolution of CO_2 in water are reported in Table 5-2. By imposing ion neutrality in an equilibrium solution, i.e. $[HCO_3^-] + 2[CO_3^{-2}] + [OH^-] = [K^+] + [H^+]$, where brackets indicate molar concentration of ions, and ionic equilibrium based on the equations in Table 5-2 (see Appendix §7.3.4, for a detailed calculation procedure), an equation relating the proton concentration (or equivalently, pH) with CO2 concentration can be reached:

$$[H^+]^3 + [K^+][H^+]^2 - (K_1K_0P + K_w)[H^+] - 2K_2K_1K_0P \quad (5.5)$$

where pH = − log([H+]), $[K^+]$ = 0.1 M from a 0.1 M $KHCO_3$ solution (electrolyte), K_1, K_2, and K_w are the equilibrium constants defined in Table 2, and K_0P (being P the absolute pressure) equals the CO_2(aq) concentration by Henry's law[228,229]. Solving this equation for standard conditions, i.e. T = 293.15 K and P = 1 atm, we obtain pH = 6.79 at saturation and equilibrium concentrations $[CO_2(aq)]_{eq}$ = 0.0394 M $[HCO_3^-]_{eq}$ = 0.0999 M, $[CO_3^{-2}]_{eq} = 2.563 \times 10{-}5$ M, $[OH^-]_{eq} = 4.176 \times 10{-}8$ M, and $[H^+]_{eq} = 1.638 \times 10{-}7$ M. Nevertheless, during CO2RR, there are protons and ions which are released into the electrolyte to enable the recombination of the C atoms to form the different products, as following Table 5-1. For each proton and electron transferred, there is a hydroxide ion OH^- formed. Therefore, by the intrinsic mechanism of the reaction process, the solution becomes apparently more basic when the reaction is taking place. A small change in the

equilibrium equations triggers a compensating recombination mechanism which tends to bring the system back to equilibrium[230]. Figure 5-5 shows the equilibrium reconditioning for an increase in the concentration of hydroxide ions, ΔOH−, and for CO2 depletion caused by its consumption during CO2RR (for the calculation of these ionic equilibrium concentrations refer to Appendix, §7.3.5).

The two plots provide intrinsic behavior that is essential to understand the evolution of the chemical reaction. Figure 5-5a shows the variation of the ionic concentration in a carbonic acid solution, i.e. CO_2 aqueous solution, when a reaction takes place and there is a sudden increase in the hydroxide concentration. Those ions are produced at the cathode and consumed at the anode in alkaline electrolysis cells. Three main regions are to be defined [230]:

• $\Delta OH^- < 10^{-3}$: infinite buffer capacity. The solution is able to retain equilibrium even after a relatively large change in the concentration of OH^- occurs (keep in mind that the equilibrium concentration of OH^- is of the order of 10^{-5} M). Therefore, the ionic equilibrium concentration of each component remains stable and is not affected by the sudden increase in $[OH^-]$. This is the case of reactions with a very low current density.

• $\Delta OH^- > 10^{-1}$: zero buffer capacity. The electrolyte is not able to hold the massive number of ions produced and the system is not capable of retaining nor finding a new equilibrium state. That is indicated in Figure 5-5 by the curve of $[OH^-]$ matching the mathematical addition $[OH^-_{eq} + \Delta OH^-]$ (dashed black line). The maximum concentration of $CO_2(aq)$ is dramatically reduced and the pH increases to approximately 13, the theoretical value found in Equation (5.5) for a degassed solution. This situation is encountered when very high current densities are applied.

• $10^{-3} < \Delta OH- < 10^{-1}$: intermediate buffer capacity. The increase in $[OH^-]$ triggers the equilibrium mechanism, which reduces the total amount of hydroxide in the solution, but increases the concentration of carbonate $[CO_3^{-2}]$. The pH of the solution is affected while the maximum amount of $[CO_2(aq)]$ is impaired.

The evolution reported in Figure 5-5b however has a completely different trend: the consumption or reduction of the concentration of $[CO_2(aq)]$ does not generally affect the buffer capacity of the reaction. This is indicated by the curve corresponding to $[CO_2(aq)]$ always matching the mathematical addition $[CO_2(aq)_{eq} - \Delta CO_2]$ and by the steadiness of the remaining concentrations. Consequently, the solution retains the equilibrium properties unless a vary drastic change in the concentration occurs: when $\Delta CO_2 \approx \mathcal{O}([CO_2(aq)]_{eq})$, the system changes rapidly from an infinite buffer capacity to a zero buffer capacity. That variation causes pH and all related concentrations to dramatically vary (the asymptotes are indicated in both plot and inset in Figure 5-5b). However, an area where changes in the concentration of $CO_2(aq)$ result in finite variations in the concentrations of the other components in solution still exists and allows us to measure and quantify the level of depletion of the gas solution and its effects on the performance of the overall reaction.

Table 5-2: Equilibrium equations and equilibrium / dissociation constants for the dissolution of CO_2 in water. Equilibrium constants [231–234] are expressed in both *pK* and *K* form, having both units related by $K = 10^{-pK}$. The temperature *T* has unit of Kelvin.

Equilibrium equation	Equilibrium / dissociation constant
CO_2 (g) ↔ CO_2 (aq)	pK_0 = -2622.38 / T – 0.0178471 x T + 15.5873
CO_2 (aq) + H_2O ↔ H^+ + HCO_3^-	pK_1 = 3403.71 / T + 0.032786 x T – 14.8435
HCO_3^- ↔ H^+ + CO_3^{-2}	pK_2 = 2902.39 / T + 0.02379 x T – 6.4980
H_2O ↔ H^+ + OH^-	pK_1 = exp(148.9802 – 13847.26 / T – 23.6521 log(T))

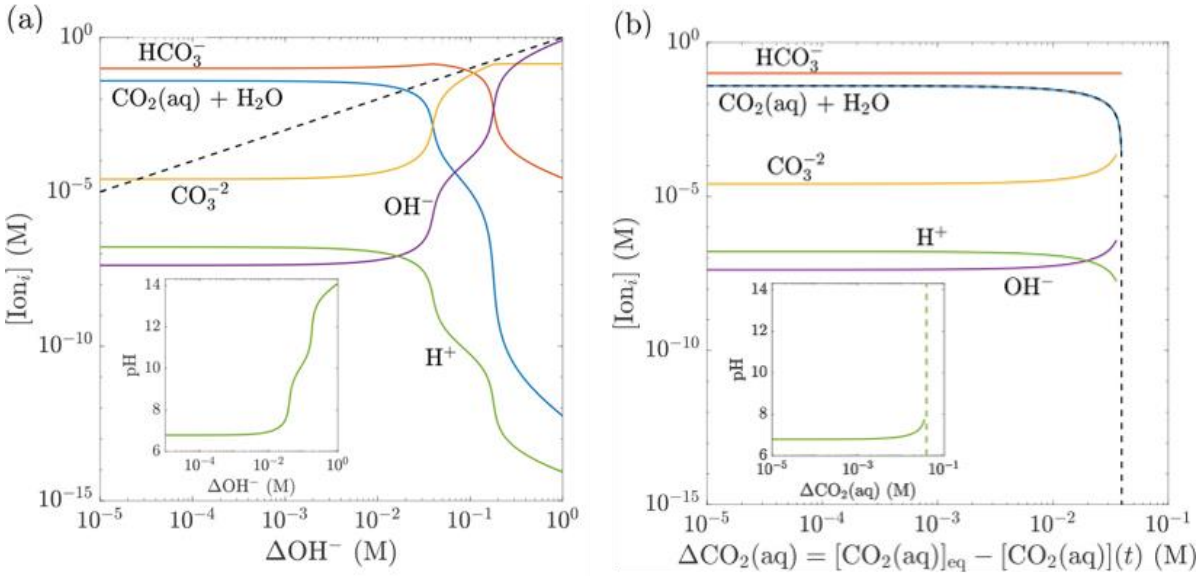

Figure 5-5. (a) Variation of the ionic concentration as a function of an increase in the concentration of hydroxide ions, ΔOH^-, caused by the transfer of protons and electrons during the chemical reaction. (b) Variation of the ionic concentration as a function of a decrease in CO_2 concentration in areas close to the electrode due to gas depletion as a result of CO2RR. In both (a) and (b), the dashed black line corresponds to the mathematical addition of ionic concentration of the variable product before equilibrium mechanisms are triggered, i.e. (a) [OH^- eq+ΔOH^-] and (b) [CO_2(aq)eq- ΔCO_2]. The inset in each plot shows the pH evolution according to the corresponding variable change.

5.5.2. Depletion Model Based on pH Measurements

All the experiments we analyze occur in the intermediate region for ΔOH^- (i.e., depending on the current density applied to the system, we detect more or less deviation from equilibrium) and in the small intermediate area which reports finite changes to the different ionic concentrations affected by the CO_2 consumption. Consequently, we are able to report changes in our system due to both ionic production of hydroxide ions as well as CO_2 depletion during CO2RR. Depletion models have already been addressed for bubble growth in supersaturated solutions[235,236]. For a system in which both ionic and mass transport are influential, the equation for diffusive mass concentration has a mass and an ionic transport component[200]. In this article, we are interested in the mass transport limitations, and therefore, we may neglect the ionic diffusion through the electrolyte to solve the diffusive mass equation. For a sufficiently small electrode submerged in a infinite bulk solution, the system can be simplified to a 3D problem in spherical coordinates in which the electrode is regarded as a mass sink[235]. In that case, the equation defining the problem reads:

$$\frac{\partial \Delta CO_2}{\partial t} = D\,\frac{1}{r^2}\frac{\partial}{\partial r}\left(r^2\,\frac{\partial \Delta CO_2}{\partial r}\right) \quad (5.6)$$

with boundary conditions

$$\Delta CO_2(t = 0, r) = 0 \quad (5.7a)$$

$$\Delta CO_2(t, r \to \infty) = 0 \quad (5.7b)$$

$$\lim_{\epsilon \to r_e} 2\pi\epsilon L D\,\frac{\partial \Delta CO_2}{\partial r}\Big|_{r\to\epsilon} = \dot{m} \quad (5.7c)$$

Here, *D* is the diffusion coefficient of CO_2 in the electrolyte,[237–239] *r* is the radial coordinate with origin the center of the electrocatalyst coil, and ṁ is the mass consumption rate defined using Faraday's law, Equation (5.2):

$$\dot{m} = \sum \dot{m}_i = \sum \frac{i_{partial,i} M_i}{F z_i} = \sum \frac{i_{total} F_{eff,i} M_i}{F z_i} = \frac{i_{total}}{F} \sum \frac{F_{eff,i} M_i}{z_i} \quad (5.8)$$

where subindex *i* stands for each of the products from CO2RR not including H_2 (which does not consume dissolved CO_2), i.e., for Cu, *i* refers to formate, ethanol, 1-propanol, methanol, acetone, acetaldehyde, acetate, methane, ethylene, and CO (as those included in Figure 5-4a and Table 5-1), whereas for Ag and Au, *i* only corresponds to CO. For convenience, note again that $i_{partial}$ and i_{total} correspond to the partial current dedicated to generate a certain product and the total applied current, correspondingly, *F* is Faraday's constant, F_{eff} is the Faradaic efficiency, *M* is the molecular weight, and *z* the valence of the reaction. By solving the partial differential equation under the indicated boundary conditions, we reach the following solution for CO_2 consumption (see Appendix, §7.3.6, for additional details):

$$\Delta CO_2 = -\frac{r_e}{2\pi L D r} \dot{m} \; erfc\left(\frac{r}{2\sqrt{Dt}}\right) \quad (5.9)$$

Notice again that re and L are the radius and length of the electrode wire used for experiments, respectively. In the following, we report the pH evolution during CO2RR for the three different electrocatalysts tested, Figure 5-6. Experimental measurements of pH are represented against the theoretical pH levels given ΔCO_2 as calculated following Equation (5.9), with *r* being the position of the pH meter referred to the electrode surface. Note that to transform this quantity according to the calculation given in the Appendix (§7.3.5) and represented in Figure 5-6b, a previous unit change needs to be done from kg m^{-3} (Equation 5.9) to M (input to systems of equations in the

Appendix, section §7.3.5). Figure 5-6a shows the pH evolution for the case of CO2RR using a Cu coil working electrode. For the Cu experiment, we use chronoamperometry and fix the potential at which the reaction occurs and let the current evolve (inset of the plot). When the reaction begins, the pH increases close to the working electrode due to two factors: the generation of hydroxide ions (which makes the solution more basic, i.e., higher pH) and the consumption of CO_2, i.e. CO_2 depletion. Note that far from the electrode (at distances further than 5 cm), the pH remains unaltered. The theoretical model is only adapted to predict the evolution of the aqueous gas concentration in areas close to the electrode (always within 1 cm from its surface, a distance of the length scale of the diffusive boundary layer, $\sim \sqrt{Dt}$. Given that the conductivity of the electrolyte solutions is higher than that of pure water[240] and that the permittivity is smaller,[241] the relaxation time after the reaction ceases is shorter than that of pure water (of the order of tens of nanoseconds[242]). Therefore, we can safely assume that after the reaction is stopped, the pH measurement does not include the contribution of hydroxide ions in the liquid. Therefore, when the reaction finishes and the pH measurement near the electrode drops to a certain value, that value matches the one corresponding to the actual concentration of CO_2 at that moment. During the reaction, the difference between the total pH curve and the model represents the contribution of hydroxide ions. That difference remains more or less similar at all times, but the contributions are different. At the beginning of the reaction, when the largest amount of C-products are being generated, the contribution to pH comes mostly from the generation of hydroxide ions to generate the desired products, with a small contribution due to gas depletion. As CO2RR continues, these relative contributions are inverted and gas depletion has a stronger influence than hydroxide generation (mainly caused by H_2 coevolution and a poor and inefficient CO_2 electroreduction). After the reaction stops and pH drops to the level associated with the CO_2 concentration at that

time, the experimental pH remains quasi-stable for a moment and starts to decrease in a very slow manner due to reactant compensation by diffusion. The concentration of CO_2(aq) over time during CO2RR is presented in Figure 5-6d. As expected, the highest Faradaic efficiencies for CO2RR products tend to occur early in the reaction, when the CO_2(aq) concentration is at its maximum. Indeed, the timing when [CO_2(aq)] begins to drastically decrease aligns with the onset of large amounts of H_2 being produced in Figure 5-4a and Figure 5-4b. For experiments on Ag and Au working electrodes, chronopotentiometry is used at different total applied current densities j_{total}, Figure 5-6b and Figure 5-6c. Again, the model captures the proper evolution of dissolved CO_2(aq), i.e. reactant availability to the electrode, as it can be discerned from the pH at the moment when the reaction stops. Again, after the reaction finishes, the experimentally measured pH keeps decreasing due to diffusion. Furthermore, the curves representing the higher current densities have both a larger pH throughout the reaction due to the higher production of hydroxide ions and a higher CO_2 consumption, i.e., the pH increases significantly faster for larger j_{total}. This fact is further justified by Figure 5-6e and f: the higher the j_{total}, the faster the CO_2 is consumed. The exception to this rule in Figure 5-6e corresponds to j_{total}= −0.424 mA cm^{-2} on an Ag electrode, which is likely caused by contamination of the electrocatalyst's surface. However, the trend seems to recover in the long run, and for larger periods of time than those represented in Figure 5-6e, the CO_2 consumption would be larger for higher j_{total}. There is a fair alignment between the timing in which the concentration curves begin to decrease and the timing in which the "minimally viable" threshold ratio in Figure 5-3 is crossed. Consequently, we can directly relate the indirectly measured reactant concentration in an area close to the working electrode and the efficiency of CO2RR.

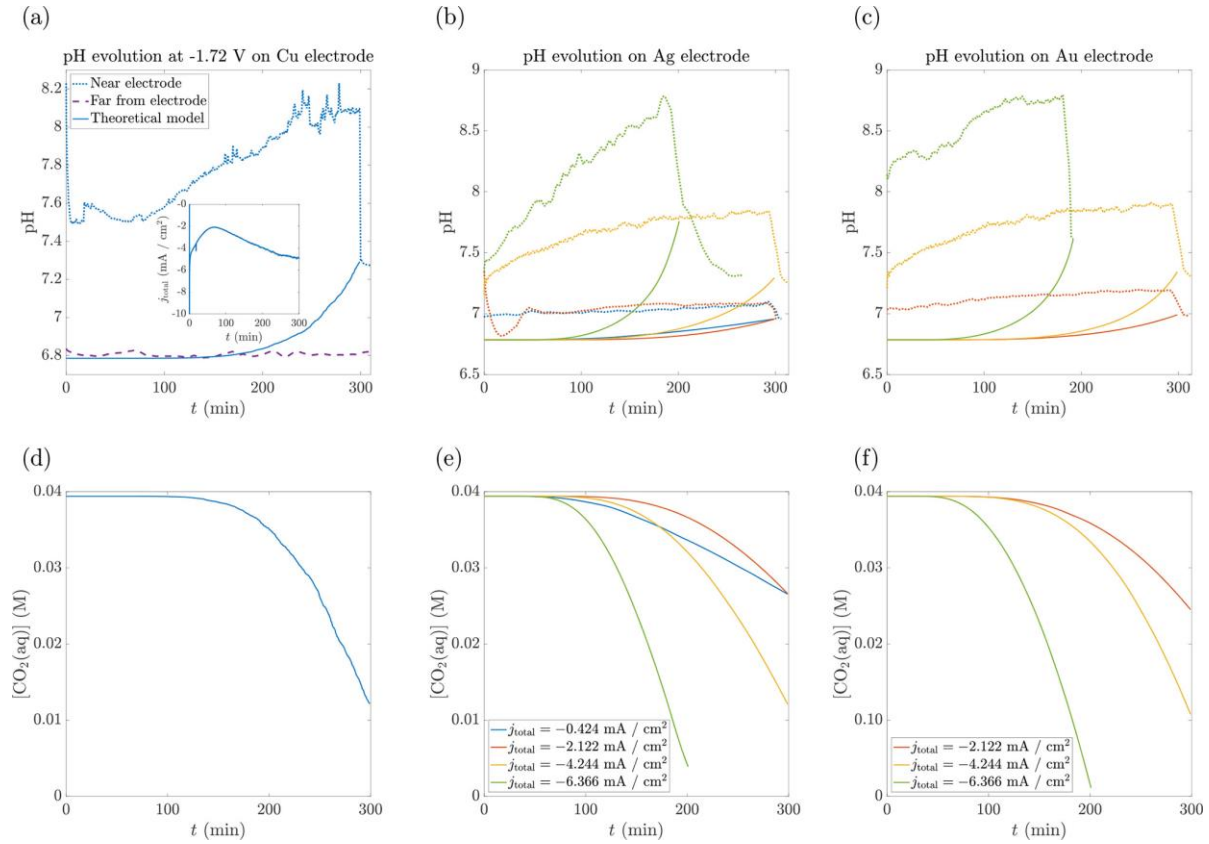

Figure 5-6. (a) pH measurements for CO2RR on a Cu coil working electrode at constant potential E = -1.72 V. The dotted line corresponds to the measurement in a distance within 1 cm from the electrode surface, whereas the solid line reports the theoretical solution given by Equation (5.9) and Figure 5-5b (see Appendix, §7.3.5 and 7.3.6, for complete derivation). The far field pH, represented by the purple dashed line, remains unaltered by the reaction. Inset: measured total current density j_{total} during CO2RR. (b, c) pH measurements (dotted lines) vs. theoretical model (solid lines) for CO2RR performed on Ag and Au electrodes, correspondingly. (d - f) Depletion mechanics, i.e. change in the concentration of dissolved CO2 in areas close to the electrode corresponding to plots (a - c), respectively. The depletion behavior is clearly dominated by the applied current: the higher the current, the faster the CO_2 is consumed and consequently, the stronger the depletion and the higher the pH.

5.6. Targeting Gas Depletion Effects by Pulsed CO2RR

As demonstrated in the previous section, the efficiency of a chemical reaction, in particular CO2RR, depends on the availability of reactant (CO_2) at the working electrode. In large standard cells where the electrolyte cannot be flown, replenished, or bubbled,[243] reactions take place in a continuous manner for a very long time. In those cases, the only way to compensate for the consumed aqueous gas is by diffusion within the bulk electrolyte. This is a very limiting method due to the slow diffusive properties of gases in typical aqueous electrolytes, as is the case for our experiments. In this section, we try to partially tackle the mass limiting inhibition by means of applying pulsed polarization of the working electrode in cycles[215,244,245]. CO2RR is programmed to occur during a certain period of time after which the applied potential to the working electrode is shut off, so that CO_2 can be replenished by diffusion. As a reference, we use an Au working electrode due to its high stability during CO2RR. Repeating cycles are designed using the time required for the GC to perform one full measurement, i.e., 14 min. Results are plotted in Figure 5-7. Figure 5-7a shows the ratio between the Faradaic efficiencies of CO and H_2, similarly to Figure 5-3. Here we can see how effectively the efficiency of the overall reaction is improved with the use of pulsed CO2RR as compared to a continuous reaction. Nonetheless, we can detect the effect of gas depletion within the cycles, due to the fact that diffusion is still a slow mass transfer mechanism which does not allow for a full replenishment of the consumed CO_2. Pulsed CO2RR with the same ratio of "on and off" time (i.e., the same time is given for the system to react and rest) behaves in a very similar manner. Still, longer absolute resting times prevent gas depletion more effectively, since more time allows diffusion to replenish more of the consumed CO_2 near the electrode. Finally, for the case in which the system is given double the time to rest than to react, diffusion is able to satisfactorily retain the system over the "minimally viable" threshold

throughout the 5 h long experiment. We would like to highlight that this duration is long enough to prove that gas depletion has a significant and detrimental effect on the chemical reaction efficiency, and pulsed CO2RR may delay the entrance into the “nonviable” regime. However, we anticipate that for extended or continuous testing for many days, the benefit of pulsed CO2RR may not be achievable due to extensive gas depletion. Consequently, pulsed curves may approach and eventually collapse onto the continuous CO2RR one. Figure 5-7b shows the corresponding pH measurements for the curves presented in Figure 5-7a. As expected, a continuous reaction has a higher overall pH due to a higher depletion level. After CO2RR is finished, the equilibrium pH attained (corresponding to the concentration of CO_2(aq) at that moment) is higher than for any other pulsed CO2RR case. However, all the pulsed CO2RR pH measurement curves reach a similar pH at the end of the reaction. This may be a result of the instrumental limitation to precisely detect pH changes due to small ΔCO2, as following Figure 5-5b. In this case, the pH meter fails to detect a slightly higher concentration for the cases with better overall efficiency. The power invested in the production of CO can indeed be improved by using a pulsed CO2RR technique such as that shown here, Figure 5-7c. To evaluate the benefits of this method, we compare the total power required to generate a kg of CO for each pulsed CO2RR scenario and for a continuous reaction. It becomes very evident that pulsed CO2RR in which the electrolyte is able to rest for a longer time, and therefore gas depletion can be recovered in a higher manner, improves CO production in terms of energy usage. For an ideal scenario in which the total current would be dedicated to the generation of CO in a continuous reaction of 5 h, a maximum power normalized production of 1.54 kg kW^{-1} would be obtained. In reality, such optimal results would never be achievable, but the application of resting loops does allow for an improvement in the energy efficiency of CO production. On the other hand, for the optimal scenario, a maximum production

rate of 0.125 3 g day^{-1} would be achieved. This highlights the primary disadvantage of using pulsed CO2RR as compared to a continuous reaction: although the energy required to produce CO can be reduced, the time required to generate it is increased due to the large relative amount of time that the reaction is not occurring due to the pulsed CO2RR approach. Therefore, the electrodes are not operational at least for half the time, meaning that less total product is produced per total reaction time.

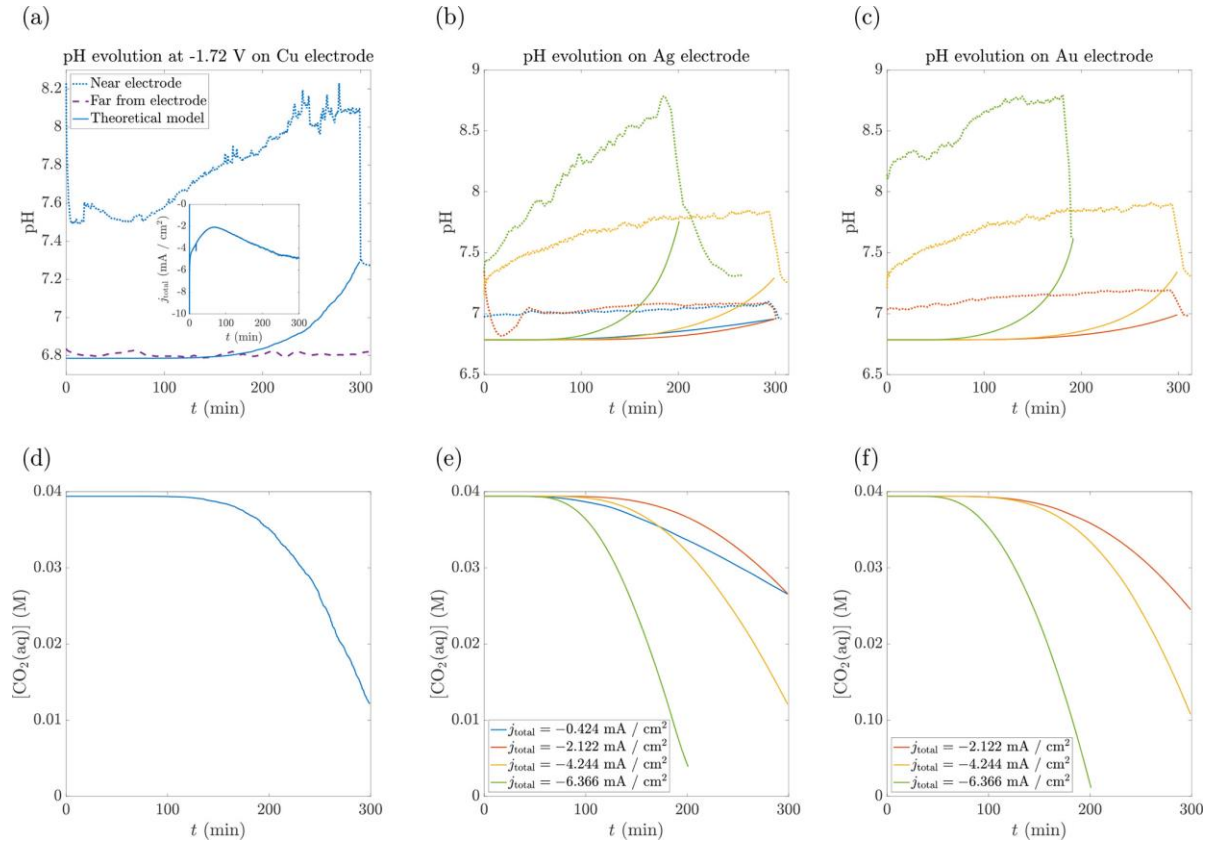

Figure 5-7. (a) Ratio of the Faradaic efficiencies of CO and H_2 when performed during pulsed CO2RR at j_{total} = -4.244 mA cm/m^2. Error bars correspond to the standard deviation across four independent experimental replicates. The horizontal dashed line indicates the established threshold to define a 'minimally viable' chemical reaction. As compared to a standard continuous experiment, pulsed CO2RR show improved performance for significantly longer times. (b) pH evolution measured during the pulsed CO2RR cycles plotted in the previous subfigure. (c) Power normalized production of each pulsed CO2RR measured as the total amount of CO produced per kW invested in the reaction (bars). In addition, the production rate in g per day is indicated with the green diamond symbol. The color palette is equivalent for the three plots.

5.7. Conclusions

There are undeniable arguments to relate the efficiency of CO2RR to the availability of CO_2 to the surface of the reacting electrode. The nature of this efficiency does depend on the properties of the selected materials, but more importantly, on the manner the electrodes are able to consume and transform the reactant into the different desired products. Therefore, Cu, Ag, and Au behave differently when performing CO2RR, according to their intrinsic properties. The variety of products is especially large for Cu electrocatalysts, whereas Ag and Au are very selective to CO. Nonetheless, some common trends have been found. First, and most importantly, is that gas depletion affects all chemical reactions when the available CO_2 is defined by a bulk concentration. In the absence of flow cells or GDEs that may be able to actively replace the consumed reactant, quiescent CO2RR cells require diffusion through a bulk electrolyte, and therefore, gas depletion limits the generation of C-products and enhances the onset of H_2 coevolution. An efficient reaction in a quiescent CO2RR cell can only be achieved within the first 2 h of reaction time, depending mostly on the applied j_{total}, i.e. the higher the j_{total}, the faster the depletion and the sooner CO2RR is not able to occur efficiently. For the Cu case in particular, gas depletion also affects the nature of the Cproducts that are generated; that is, whereas at the beginning of a reaction there is a major production of C_2 and C_3 components, this shifts toward C_1 as the CO2RR process continues over time. This originates from the generally higher equilibrium potentials to produce the higher C-contained molecules. The increase of gas depletion impairs the partial current applied to the generation of C-products, therefore the equilibrium potentials to generate higher C-products becomes less and less accessible. This fact may be decisive for the future design of flow cells, which should account for the highest peaks of production up to 20 min after the beginning of the reaction, Figure 5-4c-e. Second, pH has been proven as an accurate indirect method to estimate

the amount of CO_2 dissolved into the electrolyte and available for the reaction process. Based on the equilibrium equations and the diffusive mass transfer equation, we have developed a simplified model to track the evolution of the concentration of CO_2 in the areas surrounding the working electrode. However, two factors need to be accounted for during pH measurements: the release of hydroxide ions OH^- and the decrease of $[CO_2(aq)]$. Our model satisfactorily captures the $[CO_2(aq)]$ evolution in time by matching the pH level at the end of the reaction, corresponding to the actual measurement of aqueous gas concentration due to the vanishing of the contribution due to OH^- release. Again, we conclude that higher j_{total} causes a faster reactant consumption and depletion, a factor which is very detrimental to the overall reaction efficiency. Finally, we have demonstrated that we can improve the efficiency of a continuous reaction by programming pulsed CO2RR cycles in which we let the reaction occur for a certain period of time, after which we allow the system to rest and partially recover the CO_2 concentration in areas close to the electrode by diffusion. An improvement is measured for every pulsed CO2RR configuration in this article, especially for those in which the resting time is significantly higher than the reacting time. This point corroborates that whether CO2RR happens efficiently is intimately related to the way the reactant is fed to the electrode. We conclude that a critical bottleneck for CO2RR inefficiency is not only to be found in the design of the electrocatalyst but also in the design of the reactant feeding method as well. Therefore, the results and discussion presented in this article are not only applicable to the H-cell setups used in these experiments but to any electrolyzer architecture that involves mass transfer in a three-phase system (gas, liquid, and solid). A wide variety of architectures are already available using flow cells and employing GDEs to improve mass transport for CO2RR. We therefore anticipate the findings and methods demonstrated here to be useful beyond H-cells, for use with more industrially relevant electrode architectures, like GDEs. We

would like to emphasize that results presented in this work may not be directly translated to other electrolyzer configurations, where the stability of the catalysts or the way in which the reactant (gas) is fed may completely differ. Nonetheless, the importance of mass transport needs to be highlighted, since it is generically burdensome for realizing efficient CO2RR systems. Methods such as the pulsed CO2RR cycles shown here have been proven to be of use when performed with standard quiescent electrochemical cells. The application of such a process would depend on the final performance priorities: optimal power usage, where pulsed CO2RR can provide benefits, or production rate, for which continuous reactions are desirable but can be less efficient for long-term CO2RR. Similarly, we also anticipate these results to be of importance and relevance for other methods beyond pulsed CO2RR in the future.

6. Conclusions and Future Work

6.1. Thesis Summary

As described here, the thesis spans four distinct research areas, but maintains a central theme of using interfacial engineering to attempt to advantageously control the physicochemical interactions taking place at an interface undergoing a chemical reaction. The overall goal of the thesis is to present both fundamental analysis of the phenomena at play, but to also apply or envision this understanding in a practical manner for improving the performance of a specific system for a specific purpose. Additionally, the thesis also proposes other systems outside of those specifically studied here that could also benefit from the research presented.

Chapter 2 presents a study of the dynamic relationship between active area and ECSA-normalized performance using systematically microtextured gas-evolving electrodes. As part of this study, we demonstrated the ability to release smaller bubbles, primarily by controlling nucleation site location and promoting coalescence-induced bubble release, which allows microtextured electrodes to avoid large current fluctuations and more remain stable relative to smooth control surfaces. Additionally, we show that reducing the microtexture can lead to improvements in ECSA-normalized performance, demonstrating the inactivation of additional active area by adhered gas bubbles. These findings can help to inform future GEE designs by optimizing surface morphology to maximize the benefits of microtexture but also avoid ineffectively using active materials that can be inactivated during operation when gas is evolved.

Chapter 3 studies the dynamic relationship between bubble coverage and bubble contact on both smooth and surface engineered gas-evolving electrodes. This study was motivated by empirical evidence from Chapter 2's work showing electrochemical activity below adhered

hydrogen bubbles is not negligibly small. A machine learning based bubble detection algorithm was developed, providing a useful tool for the scientific community. Surface engineered "nanospot" electrodes were then demonstrated as a useful way to decouple the relationship between bubble contact and coverage that exists for untextured, smooth electrodes. These nucleation promoting nanospot arrays both control where bubbles persist spatially and minimize their contact with the active electrode surface. Using these nanospot engineered electrodes, periodic bubble coverage signals were realized when bubbles of a controllable size were regularly released via coalescence-induced departure. As a result, Chapter 3 shows that it is not physically likely that the bubble coverage is entirely inactivating, as currently believed, and is supported by physical modeling of the electrochemical system. This allows us to introduce and define a new metric for tracking the dynamic active area of an electrode as the Bubble-induced Electrochemically Active Surface Area (BECSA), which relies on bubble contact for its definition, rather than coverage. These results present an important new GEE design paradigm focusing on minimized bubble contact, as opposed to the conventional bubble coverage. With this perspective comes important implications for the design and fabrication of more efficient gas evolving electrodes to minimize the inactivating effects caused by adhered bubbles.

Chapter 4 demonstrates and models the enhanced absorption of CO_2 bubbles using bubble/surface interactions to spread the gas into a sheet using nanoengineered superhydrophobic bubble capture surfaces. This was shown to dramatically increase average reaction rates for the CO_2 absorption process by orders of magnitude compared to the non-spreading bubble case. The design space for the capture surfaces was also investigated to show the importance for nanoscale surface roughness to fully spread CO_2 bubbles on a timescale similar to the absorption reaction timescale. By spreading bubbles, the smallest bubbles were able to react the fastest and showed

complete absorption, as opposed to the case for non-spreading bubbles which react more slowly with decreased size and were unable to be completely absorbed. As a result, an absorption method based on the direct injection of gas bubbles into capture surfaces was envisioned to provide advantages from a capital cost perspective as compared with large-scale absorption towers. This perspective was motivated by the likely need for modular and distributed absorption applications for carbon dioxide capture that are economically feasible to enable a more sustainable future.

Finally, Chapter 5 presents experiments and mathematical modeling to accurately characterize and predict the onset of mass-transport limitations for CO2RR applications. A model to predict the depletion of the concentration of the CO_2 reactant at the electrode's surface was developed and empirically validated by electrochemical and pH data. By measuring pH to determine the timeframe to which depletion becomes an issue for the co-evolution of hydrogen, a pulsed electroreduction technique was shown to allow for improved efficiency for the generation of CO2RR products in comparison with a continuous operation mode. Taken together, the study presents a useful tool in a model to enable pH to provide a signal for the depletion of CO_2 in CO2RR systems, and underscores the importance of CO_2 delivery to the electrode's surface to be a critical design consideration for improving these systems.

Together, the work presented demonstrates the ability to effectively interrogate and improve systems that involve mass and charge transport at a chemically reacting interface by focusing on engineering of the physical interface itself. In this way, we are able to study, better understand and predict, as well as improve the physicochemical interactions occurring at interfaces that are relevant for a wide variety of industrial applications.

6.2. Proposed Future Work

For the future, work focused on translating the findings and results presented in this thesis to more practically applied systems is a next step that is already underway. By moving from lab-scale testing to more scalable embodiments of the solutions presented, relieving the bottleneck imposed by mass and charge transport at interfaces can help bring forth improvements in both the performance and cost of a variety of systems.

The findings presented in Chapter 2 and Chapter 3 have already informed work which aims to translate these findings into better performing and lower cost electrolyzer cell designs for water electrolyzers. This work aims use novel gas management systems to improve efficiency, while also minimizing capital and operational costs for the production of hydrogen from alkaline electrolyzers in the near future.

Chapter 4 has demonstrated the ability for spreading bubbles to improve the reaction with liquid absorbents which is useful in a range of applications. The engineering of systems for specific applications where gas needs to be reacted with a liquid absorbent is the next step for this work. Each particular solution, whether it is for small and modular CO_2 absorption systems like those studied explicitly, or for other gas and absorbent combinations for other applications, will require a specific and catered design for ensuring a cost effective and highly performing direct gas injection absorption system.

Finally, the work in Chapter 5 has motivated the utilization of feedback controlled electrolyzer systems which could better handle the mass transport limitations that are ultimately unavoidable to some extent for CO2RR electrolyzers. By using a signal from a sensor, like the pH proximal to

the electrode surface, feedback control of the operating conditions for the electrolyzer can be utilized to ensure maximal performance for a given system.

THIS PAGE INTENTIONALLY LEFT BLANK

7. Appendices

7.1. **Appendix A**: Electrochemical Gas Evolving Electrode Supplemental Information

7.1.1. Materials

Electrochemical Testing Materials

For all electrochemical experiments, the following electrodes were used: counter electrodes were constructed from high purity platinum wire (99.997%) of 0.5 mm diameter which were purchased from Fisher Scientific, low-profile Silver Chloride (Ag/AgCl) reference electrodes which were purchased from Pine Research Instrumentation, and working Platinum electrodes were fabricated as described herein. For all tests, an acidic electrolyte was used, purchased as a standard solution of 0.5 M sulfuric acid from Fisher Scientific.

Pt Working Electrode Fabrication Materials

Working Pt electrodes were fabricated using p-type <100> orientation silicon wafers purchased from WaferNet as the starting substrates for cleanroom processing. For metal deposition layers using sputter deposition, a Pt target (99.99%) and a Titanium target (99.995%) were used, both of which were purchased from Kurt Lesker. Glass coverslips used for shadow mask patterning of Pt electrodes were 3 mm in diameter, #1 thickness coverslips, purchased from Thomas Scientific.

7.1.2. Electrochemical Measurements

All electrochemical experiments were carried out using a three-electrode setup using a potentiostat/galvanostat, purchased from Biologic (VSP-150), to accurately measure and control current and voltage. The model electrochemical reaction used throughout this work was Pt-catalyzed HER or OER as specified in an acidic electrolyte of 0.5 M sulfuric acid. All experiments followed the same order of first cycling Pt working electrodes between -0.2 V and 1 V vs. Ag/AgCl for 16 cycles, followed by anodic cleaning of the Pt working electrode by chronoamperometry for 1 minute at an applied potential of 2.2 V vs. Ag/AgCl. For each electrode, underpotential hydrogen deposition (UPHD) was then performed via cyclic voltammetry ahead of chronoamperometric testing to characterize the electrochemically-active surface area (ECSA). Chronoamperometry testing was then performed sequentially for each applied potential tested for the electrode. Between each subsequent chronoamperometry experiment, electrolyte was replaced. All experiments were repeated independently using at minimum three different Pt electrodes fabricated separately.

Under-potential Hydrogen Deposition Measurements

Underpotential hydrogen deposition was used to measure ECSA for all electrodes tested. Cyclic voltammograms were integrated to quantify the total charge adsorbed for characteristic hydrogen under potential adsorption. This can be represented mathematically as follows,

$$Q_{ads} = \frac{1}{scan\,rate}\int_{E_1}^{E_2} i\,dE - \frac{1}{scan\,rate}\int_{E_1}^{E_2} i_{DL}\,dE \qquad \text{Equation S1}$$

where Q_{ads} represents the adsorbed charge shown in **Figure 7-1** by the blue shaded area, E is the applied potential, i is the measured current, E_1 and E_2 are the starting and ending points of the UPHD region, i_{DL} is the constant background double layer charging current, and the scan rate is

the rate at which the applied potential is constantly swept. In these experiments, a scan rate of 200 mV/s was used, while the scan was swept between -0.2 and 1.0 V vs. Ag/AgCl. Cyclic voltammetry measurements were repeated for a total of 16 cycles for each UPHD measurement to ensure a stable voltammogram was reached. The final cycle measurement was then used to integrate the charge adsorbed during UPHD, Q_{ads}, and was used to determine ECSA. The control surfaces measured for this study provide a specific charge adsorption of 210.8 ± 1.2 μC/cm^2 using their measured surface areas using optical microscopy, in good agreement with previously reported values for polycrystalline Pt UPHD charge adsorption[246,247] of approximately 210 μC/cm^2. A representative CV cycle used for UPHD measurement is shown in **Figure 7-1**, highlighting the hydrogen adsorption peaks analyzed for determining ECSA. Accordingly, this specific surface charge is then used to determine ECSA values for all microtextured samples from their measured UPHD-derived Q_{ads} values.

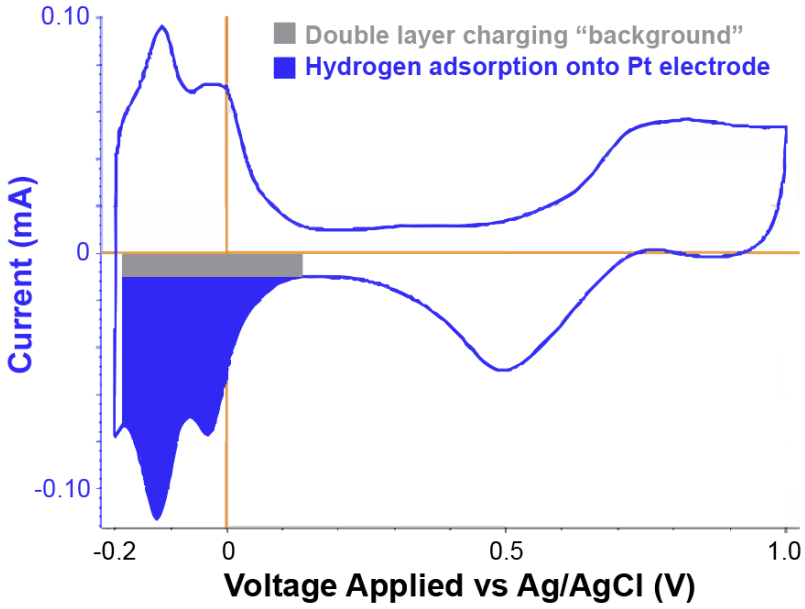

Figure 7-1. Representative cyclic voltammogram used to measure the underpotential hydrogen deposition for Pt electrode samples by integrating the charge adsorbed during cycling. Annotated plot shows the region representing the hydrogen adsorption charge, in addition to the background double layer charging current.

7.1.3. Pt Working Electrode Fabrication & Characterization

Patterning Pt Active Electrodes using Shadow Mask

For initial testing of the impacts that bubbles have on gas evolving electrode performance, and the correlation between adhered bubbles and current during chronoamperometric testing, shadow mask patterned untextured Pt electrodes were used. These shadow masked samples provided for higher bubble adhesion and lower current outputs in comparison to the same samples that were prepared using photolithographic patterned Pt electrodes (described next), likely due small amounts of the deposited silicon nitride being present onto the Pt active area. **Figure 7-2** outlines the process by which these electrodes were fabricated. First, silicon wafer substrates were deposited with a layer of Pt conformally using magnetron sputtering (AJA International). Next, a shadow mask of the geometry of the desired active area was placed on the wafer to physically mask this region during the following deposition step. For these tests, a 3 mm diameter circular glass coverslip was used. Next, a plasma enhanced chemical vapor deposition (PECVD) process was used to deposit silicon nitride on the surface (Samco PD220). Finally, once the shadow mask was removed, the patterned Pt electrodes was fabricated. This method was only used for studies in Chapter 2, and was not used for any of the testing presented in Chapter 3.

Patterning Pt Active Electrodes using Photolithography

Patterning of the microtextured arrays was accomplished using standard photolithography techniques as has been previously described[248]. A simplified process workflow is graphically shown in **Figure 7-3**. Once the desired surface morphology was achieved, photolithography was then used to pattern the active and inactive portions of the electrode. This allowed for a high degree of control of active surface area for Pt working electrodes while achieving well-inactivated regions via etching back the nitride layer to expose active Pt electrodes. This provides for better control

and repeatability in comparison to shadow mask method previously described and was used for all performance testing of both control and microtexture Pt electrodes for comparison in this work. Briefly, Pt and nitride layers were deposited via magnetron sputtering and PECVD methods, respectively. Next, photoresist is patterned to expose the regions that will become the active Pt working electrodes. Next, reactive ion etching (RIE) is used to etch through the inactivating nitride layer to expose the Pt layer beneath. Finally, the photoresist is removed and the Pt working electrodes have been successfully fabricated. This same process was used to pattern both the control and microtextured Pt working electrodes for all experiments, except for investigation of the correlation between current and adhered bubbles summarized in **Figure 2-1**E,F. A graphical workflow is shown for the photolithographic patterning of the Pt electrode active areas is shown in **Figure 7-4**.

Scanning electron microscopy was performed to characterize the surface morphology following electrode fabrication (ZEISS Gemini SEM). Representative SEM images for all the microarray textures tested for this work are shown in **Figure 7-5**. Additionally, **Figure 7-6** shows an SEM perspective where the delineation between the active Pt and inactive nitride layers is clear for a microtextured electrode.

Pt Micropost Array Electrode Surface Profilometry

Surface microtexture profile measurements were carried out using a contact stylus profilometer manufactured by Veeco (Dektak 150 Surface Profiler). While DRIE etching methods provides high repeatability for etched microtextures, minor variability did occur between samples of a given height (typically less than 10%). These differences were measured using surface profilometry. Representative data collected and used as the actual height of micropost array structures is shown

in **Figure 7-7**. For each measurement, at least 4 posts were measured to arrive at the actual height measurement used to compare against measured ECSA-based surface areas. These profilometry results allowed for individualized comparisons for each fabricated electrode's ECSA and expected surface area calculated from the idealized geometry based on the array parameters measured for a given microtextured sample.

Pt Electrode Elemental Composition Confirmation

The scanning electron microscope used for electrode characterization (ZEISS Gemini SEM) was also equipped with an X-Ray detector to perform Energy-dissipative X-ray spectroscopy (EDS) for elemental composition information of the electrode's surface. Representative EDS confirmation of both the identity and spatial arrangement of the patterned electrodes is summarized in **Figure 7-8**. Using both a line scan and surface mapping, we were able to show that our samples have a clear and sharp delineation of an active Pt area and the inactive silicon nitride surrounding region.

Increased Micropost Lateral Post Side Roughness for b5 Microposts

Scanning electron microscopy was also employed to validate the measurements derived from UPHD which indicated a higher than anticipated surface area for b5 micropost arrays if the lateral post sides were assumed to be smooth. These differences are summarized in **Figure 7-9**. This accounts for the measured UPHD derived surface area of b5 microtextured electrodes to be up to ~40% higher than would be anticipated due to this increased roughness of the lateral sides of posts, which account for the majority of the b5 microtextured electrode's surface area.

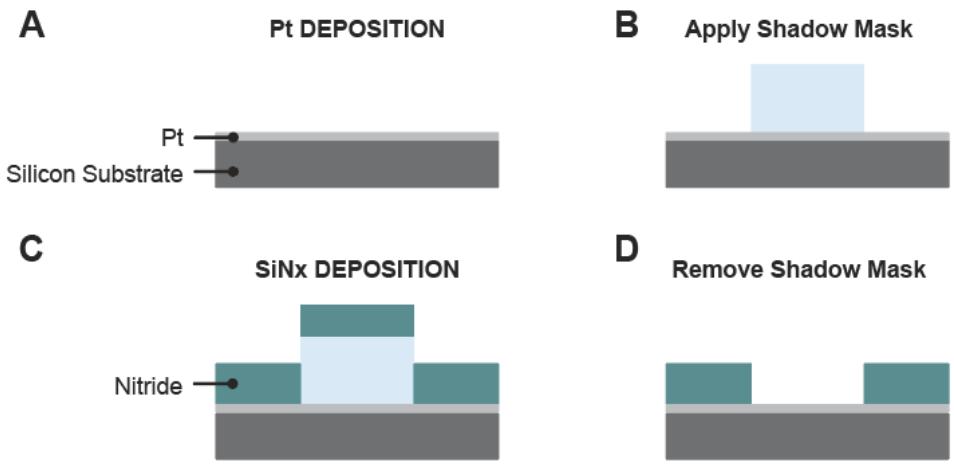

Figure 7-2. (A) Pt is conformally deposited using magnetron sputtering onto Si substrate. (B) Next, a shadow mask is applied to surface to be patterned. (C) Next, PECVD nitride is deposited on the surface. (D) Finally, the shadow mask is removed and the electrode has been fabricated.

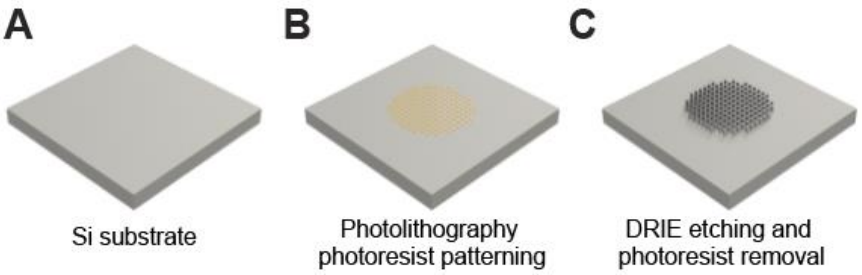

Figure 7-3. (A) Starting silicon substrate prior to any deposition is patterned with photoresist using standard photolithography processing, ending with patterned substrate to be etched as shown in (B). (C) The sample is then etched using DRIE methods and the photoresist pattern is removed, leaving the microtextured patterned substrate completed.

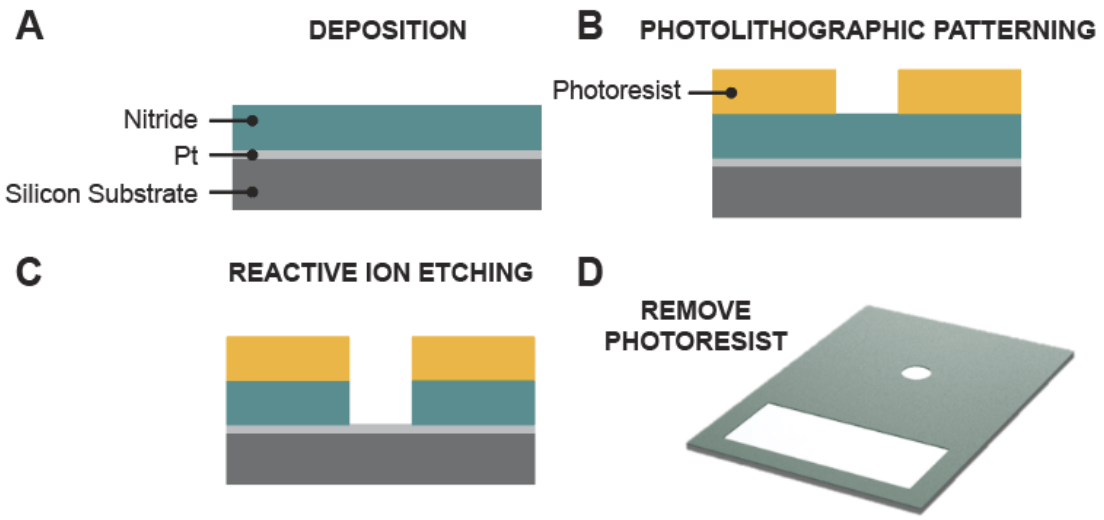

Figure 7-4. (A) First deposition of active Pt layer using magnetron sputtering, followed by inactive nitride layer via PECVD. (B) Photolithographic patterning of the regions to become the active area. (C) Reactive ion etching is used to etch through the inactivating nitride layer to expose the active Pt layer beneath. (D) After removing the photoresist, the final electrode sample with Pt patterned circular working electrode and exterior contact for connection to the potentiostat are shown.

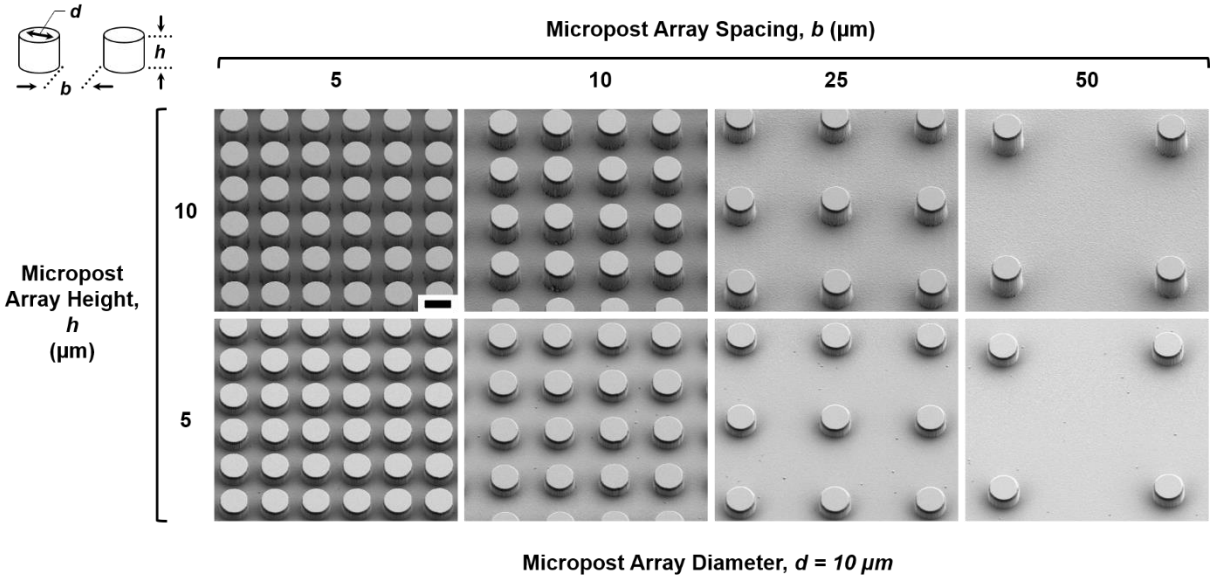

Figure 7-5. Scanning electron microscope images for all the micropost array designs tested for experiments. Scale bar is 10 μm.

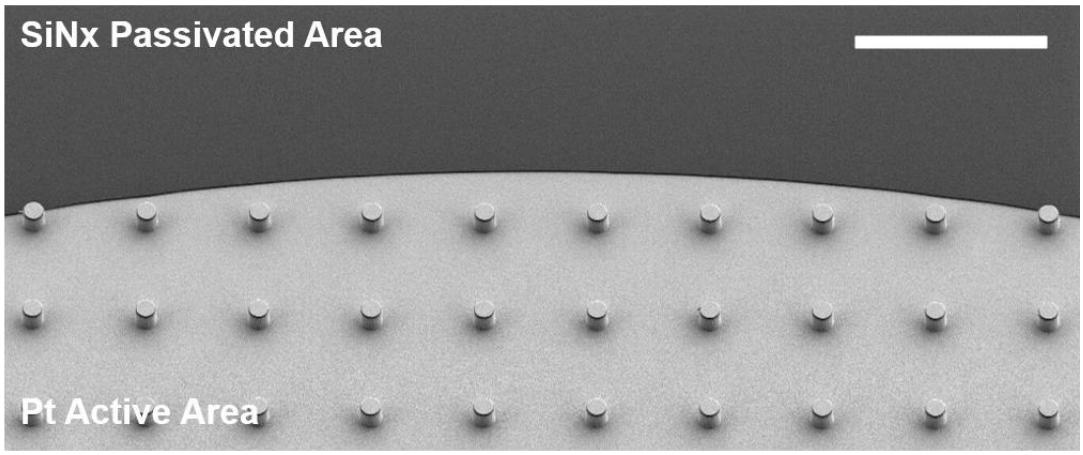

Figure 7-6. Scanning electron micrograph highlighting the different electrode regions of the Pt active area and nitride inactivated surrounding area. Here, a full height b50 microarray sample is shown. Scale bar is 100 µm.

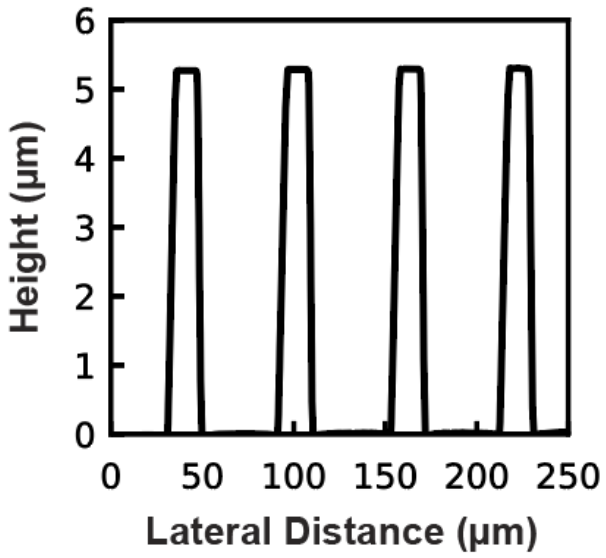

Figure 7-7. Profilometry data for height measurements of a b50 micropost array electrode sample. Successive posts are measured as the stylus tip is moved laterally along the electrode's surface.

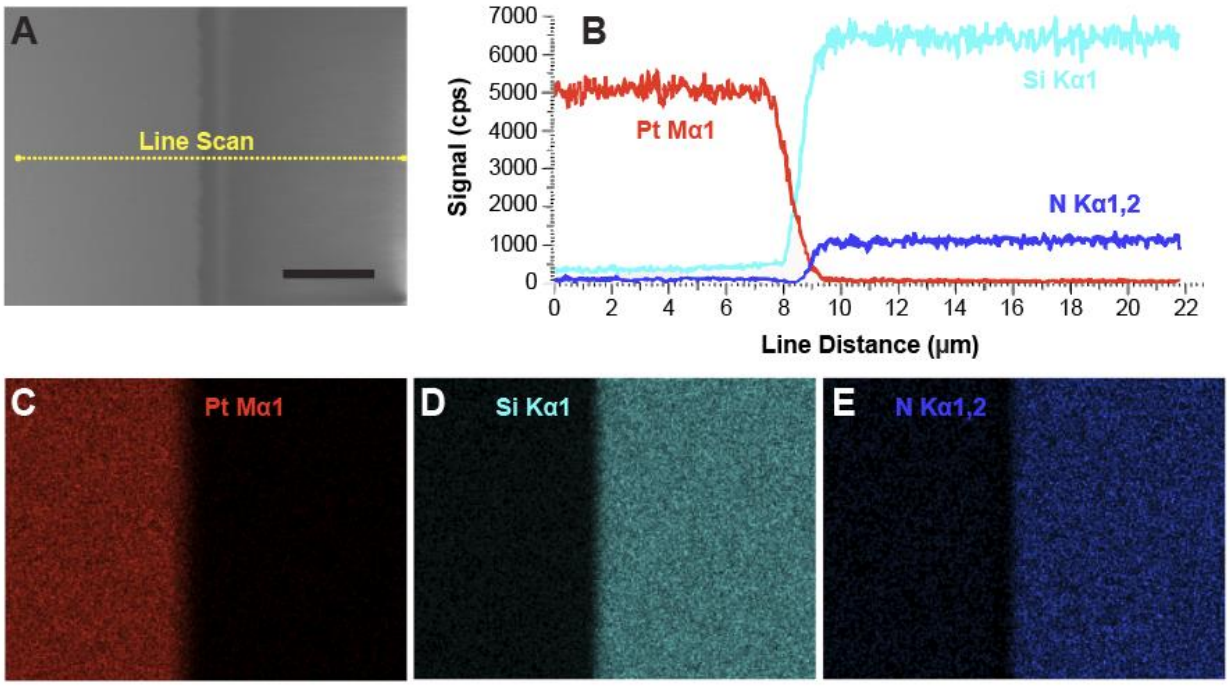

Figure 7-8. (A) Scanning electron image of the region analyzed using Energy-dispersive X-ray spectroscopy (EDS). Region on the left is the active Pt region and on the right is the inactive silicon nitride region. Annotation shown for location of line scan for spatial changes in composition of the EDS signal. Scale bar is 5 µm. (B) Line scan data for all elements measured during EDS line scan. (C-E) EDS mapping of the Pt, Si, and N characteristic EDS peaks, showing the Pt active region well-defined from the silicon nitride inactive region.

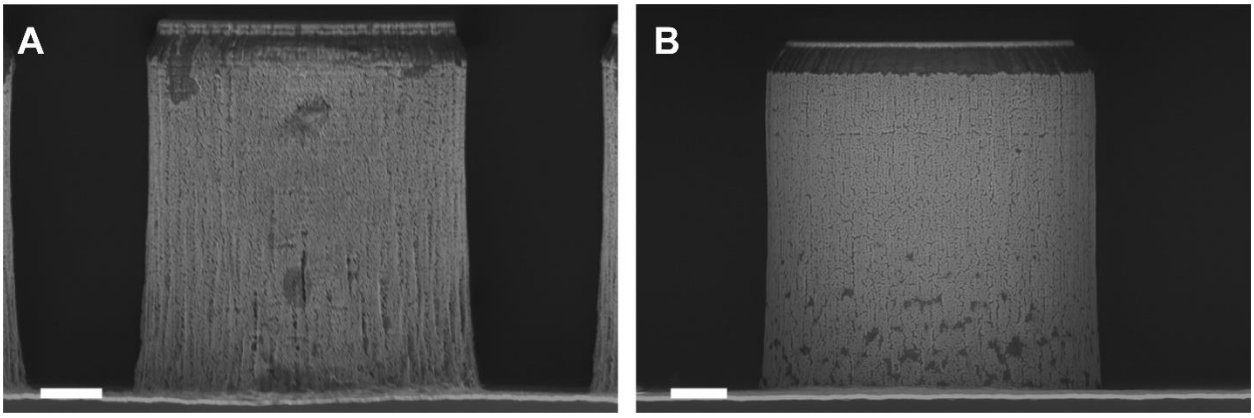

Figure 7-9. (A) SEM micrograph from a side perspective showing the increased roughness that is imparted onto the etched microposts for b5 microposts, which is not present in less densely packed micropost arrays (b10, b25 or b50). (B) SEM micrograph from a side perspective showing the less roughened lateral sides of a b50 micropost. Scale bars represent 2 μm.

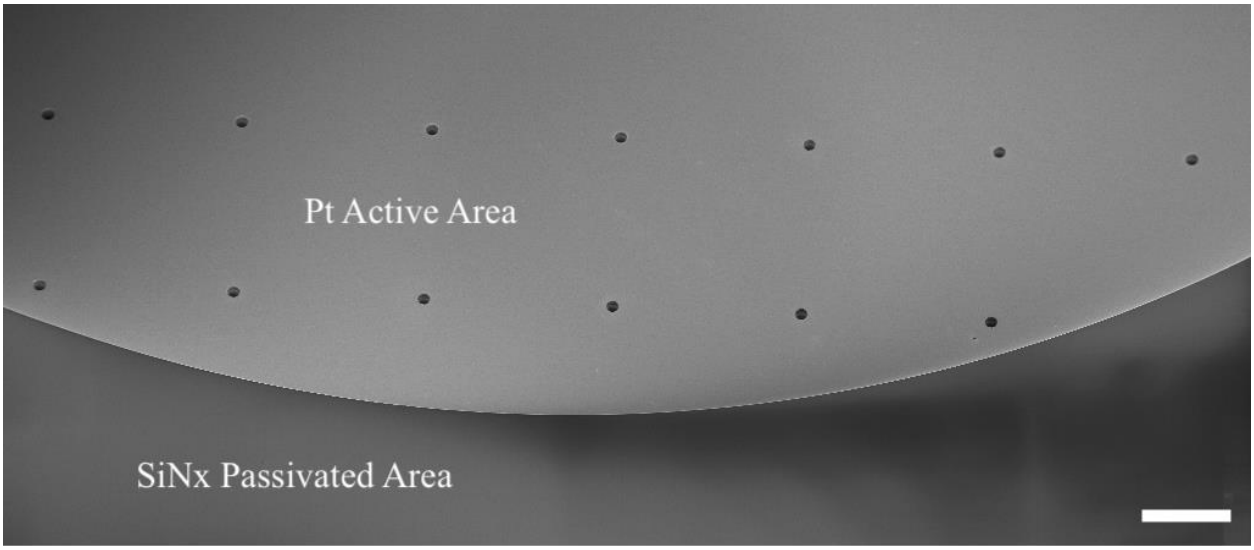

Figure 7-10: Scanning electron micrograph highlighting the different electrode regions: the Pt active area with nanospots and the nitride inactivated surrounding area. Here, the b200 surface is shown with 200μm spacings of nanospots. Scale bar is 100μm.

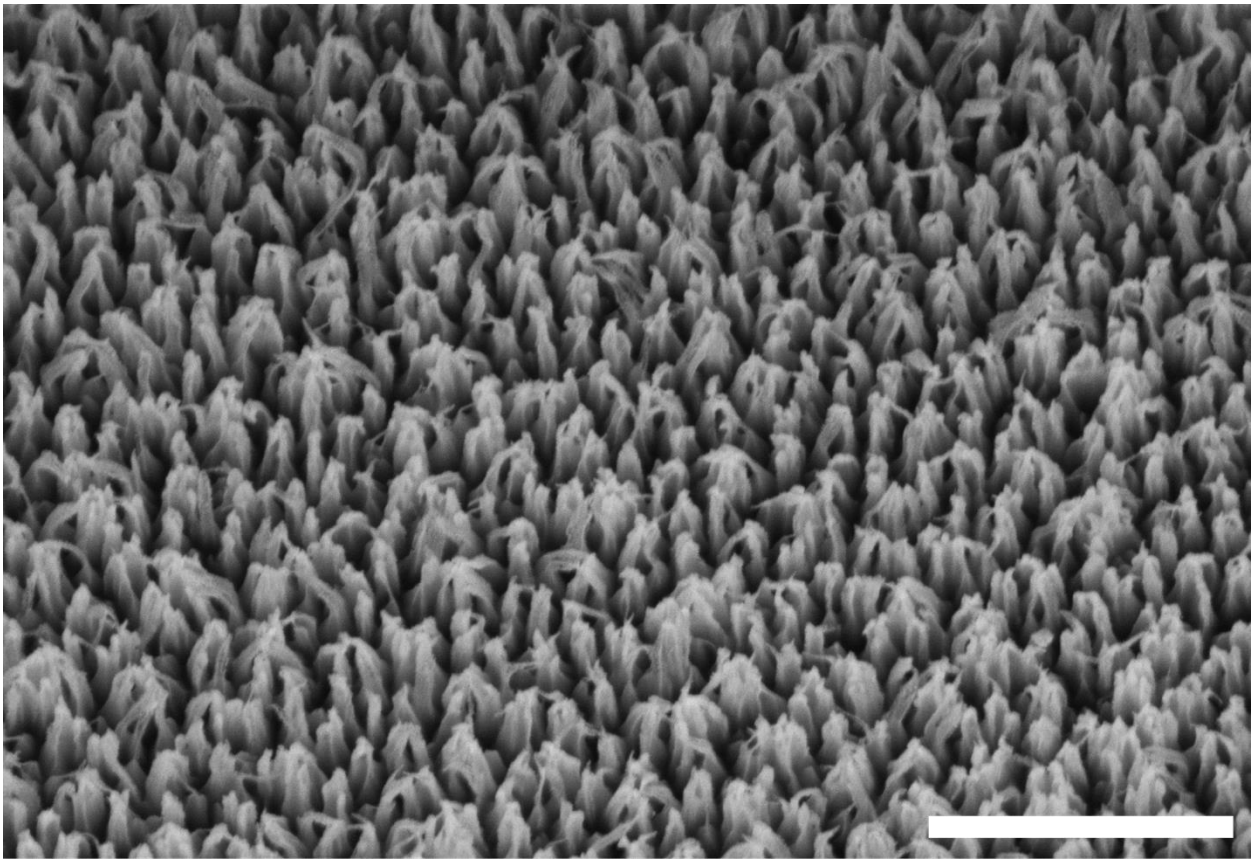

Figure 7-11: Scanning electron micrograph of the nanotextures within a nanospot. Scale bar is 1μm.

7.1.4. High-speed Imaging

High-speed imaging was performed at frame rates between 500 and 5000 frames per second (fps) using a high-speed camera purchased from Photron (Fastcam SA-Z). For top-down recordings, videos were taken via an upright microscope (Zeiss Axio Zoom) using the custom fabricated Teflon electrochemical cell used for all electrochemical testing. Side view imaging was performed separately using a high magnification lens (Navitar 12x Zoom) in a glass electrochemical cell with a flat viewing window such that imaging was clear to the surface of the electrode that was sealed so that only the inactivated region and the Pt working electrode were exposed to electrode. For high-speed imaging, the camera was triggered by external digital output from the potentiostat to ensure that image capture and electrochemical measurements were recorded as synchronously as possible. A one millisecond duration square wave output from the potentiostat was used to trigger the high-speed camera at an experiment's start, ensuring temporal alignment to within one millisecond.

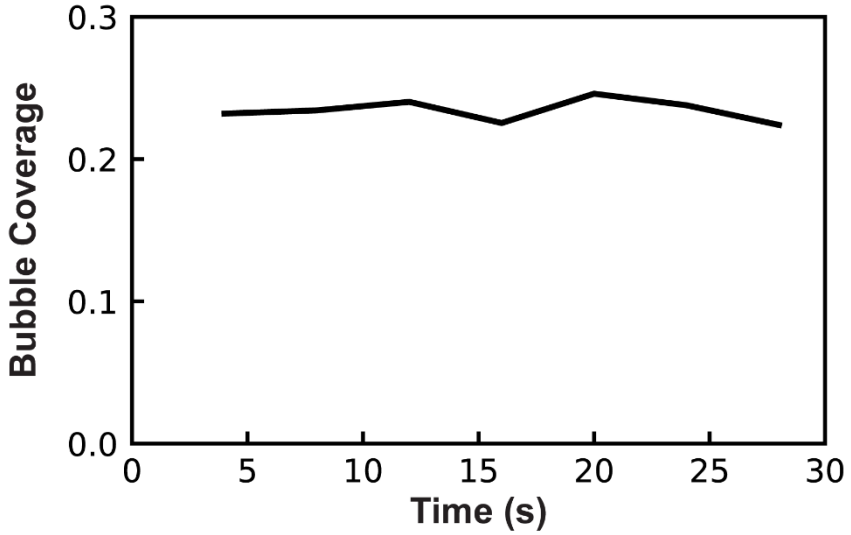

Figure 7-12. The bubble coverage measured at seven time points during the duration of a 30 second experiment to demonstrate the relative temporal stability of this metric. Experimental data shown is for a *b25* microtextured sample, but is illustrative of the general stability of the microtextured electrodes tested.

7.1.5. Computational Methods for Bubble Detection

Generating Ground Truth Data

In order to successfully train supervised deep learning networks, it is necessary first to generate a sufficient quantity of high-quality ground truth data. To this end, we employed the Darwin V7[249] platform to aid in the manual annotation of bubbles in single still frames of a video. We selected still frames randomly from all recorded videos of catalytic bubble nucleation, with the specification that still frames must contain bubbles and frames were chosen at a sufficient frame distance such that temporally-adjacent selected frames were sufficiently diverse. Presuming perfectly circular bubbles, we manually inscribed annotations on each image and recorded bubble radii and (x, y) center positions, all in units of pixels. While we assumed no maximum cutoff on bubble size, annotators loosely enforced an arbitrary minimum bubble size of a five-pixel diameter. This can be observed in the main body by the average size of a bubble at nucleation (or, more precisely, when the bubble was first observed to have nucleated). **Figure 7-13** shows one such still frame after manual annotation. Note that annotators labeled all bubbles even if they were partially clipped off the frame. In order to help minimize the subjectivity between annotators, we assigned separate reviewers to edit and adjust locations after an initial round of annotations.

In total we labelled all bubbles in 22 images on a grid-nucleated surface and 17 images on a pristine platinum surface with no nucleation. Even though this dataset of annotated images represents a great deal of manual effort, it is hardly sufficient for data-hungry deep learning network architectures. We therefore leveraged a number of routine augmentation strategies including adding a Gaussian blur, cropping, rotation, and salt-and-pepper noise.

Deep Learning Methodologies

While Hough transforms have been used for circle detection in the past[250], after preliminary testing and tuning we were able to qualitatively demonstrate that neural networks outperformed Hough. The family of networks we trained (including the networks FasterRCNN[251] and MaskRCNN[252]) all employ a similar process of down-selecting an image to a set of region proposal networks (RPNs), then refine the predictions within these RPNs to form a close bounding box around an object. These CNNs construct two sub-networks, a box classifier and a box regressor, both of which contain fully connected network (FCN) layers. In the case of MaskRCNN, there is an additional fully-connected sub-network used for masking. Running inference on an image through the RPN architecture yields a list of *k* bounding boxes that are each denoted by four Cartesian points in $\mathbb{R}^2$. The box classifier also returns a *k* sized vector, which is an *objectness* score for each box. Note that *k* is a hyperparameter denoting the maximum number of boxes per sliding window as well as the predefined box shapes (that is, the minimum and maximum size as well as aspect ratio range on a box) are also hyperparameters. Importantly, the RPN architecture shares the same weights for every sliding window, as a result of convolution. As such it is explicitly translation equivariant; that is, shifting the input image will result in a shift in the output region of interest. After the RPN sub-network has identified these *k* regions of interest (RoIs), the *k* regions are refined via a second FCN sub-network, which also performs pooling. The pooling process is somewhat different between architectures. FasterRCNN uses RoIPool, which is similar to a nearest neighbors downsampler. MaskRCNN uses RoIAlign, which acts as a bilinear interpolator and results in pixel-level translation equivariance. This pixel-level translation equivariance has been demonstrated to improve mask segmentation accuracy in most cases. In the case of MaskRCNN, the features from RoiAlign are then fed through a final FCN sub-network which up-samples the

image back to the full resolution of the input window. From this up-sampling, the final fixed-size encoding is flattened and run through FCN layers to yield class scores and a final bounding box regression.

Once bounding box locations are discerned, a final non-maximal suppression (NMS) procedure is applied. This procedure includes removing any concentric circles, removing overlapping circles based on an intersection-over-union (IoU), and additional thresholds based on confidences. Finally, we convert bounding boxes to circle predictions. Suppose one bounding box contains a bubble and has side lengths s1 and s2. We calculate the bubble center by computing the average of the four Cartesian coordinates of the box, and we calculate the bubble radius as $(s_1 + s_2)/4$.

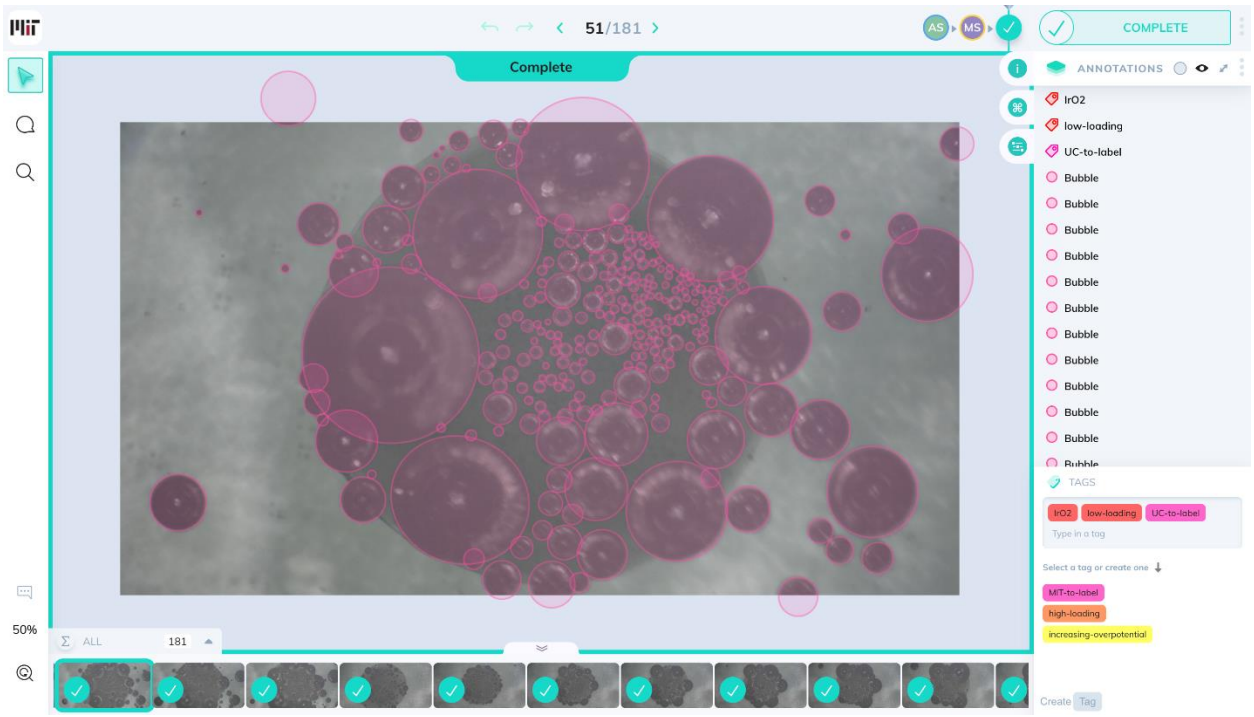

Figure 7-13: A still frame being manually annotated and reviewed within the Darwin V7 user interface.

7.2. **Appendix B**: Ultra-fast Bubble Absorption Supplemental Information

7.2.1. Materials

For all carbon dioxide absorption experiments, the following materials were used for reactants: 0.1 M KOH solution was made mixing semiconductor grade (99.99% pure) potassium hydroxide pellets purchased from Sigma-Aldrich (Cat No: 306568) with ASTM Type I deionized water (18 MΩ-cm resistivity), pure carbon dioxide gas (99.995%) used for all experiments was purchased from Airgas (Cat No: CD PC200).

7.2.2. Bubble Image Segmentation & Analysis

The *Fiji*[253] distribution of the image processing platform *ImageJ* was used for segmenting collected imaging data to arrive at binary segmented images of the bubbles from each analyzed frame. Briefly, a bounding box was drawn around the region of interest containing the full extent of the bubble to be segmented. Following this, the image area outside the relevant bounding box was cleared, and the image was binarized using *ImageJ's Make Binary* command, followed by the *ImageJ's Fill Holes* command. The resulting image was a binary image with the bubble representing the dark foreground and a white background surrounding the segmented bubble. These binary images were then processed using a MATLAB script to determine their volumes by assuming radial symmetry about the vertical midpoint of the captive bubble and revolving each radial row of radial pixels to achieve a volume. An *ImageJ* macro was recorded to make implementing this image processing workflow less time consuming, only requiring the bounding box location as an input and then being able to run on sequential images for a given sequence of data to collect time series trends for bubble volumes. Image processing was only utilized for analysis of non-spreading bubble imaging data.

7.2.3. Numerical Modeling

The following information includes additional reference information for physical constants and material properties used in modeling the results presented in Chapter 4, as well as data to highlight the fidelity of the model from a comparison with prior literature and convergence study results for temporal and spatial meshing using in MATLAB to accurately approximate spatial and temporal results.

Table 7-1: A table of physical constants and material properties used in the numerical model.

Constant	Value	Units
R	8.315	J/mol/K
T	293	K
P	101325	Pa
k	5.9	$m^3/mol/s$
D_{CO2}	1.96e-9	m^2/s
D_{OH}	6.8e-9	m^2/s
H_{CO2}	3.87e-4	$mol/m^3/Pa$
$C_{0,\,OH}$	100	mol/m^3

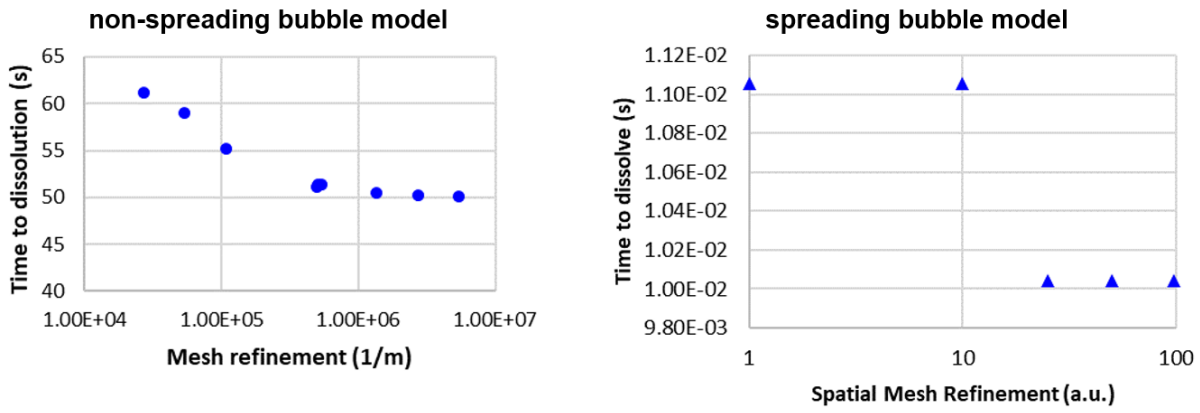

Figure 7-14: Convergence of bubble dissolution time via spatial mesh refinement was confirmed for both spherical (left, non-spreading bubble model) and planar (right, spreading bubble model) geometries

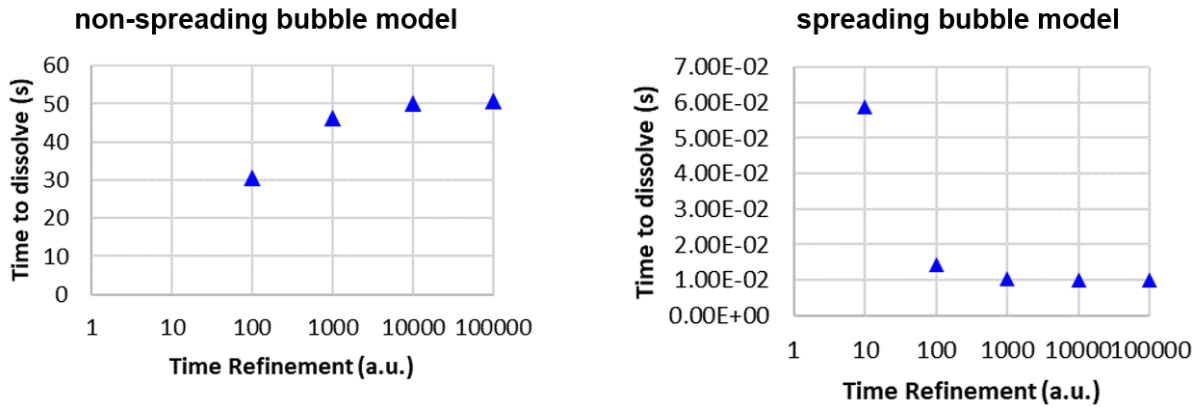

Figure 7-15: Convergence of bubble dissolution time via temporal mesh refinement was confirmed for both spherical (left, non-spreading bubble model) and planar (right, spreading bubble model) geometries

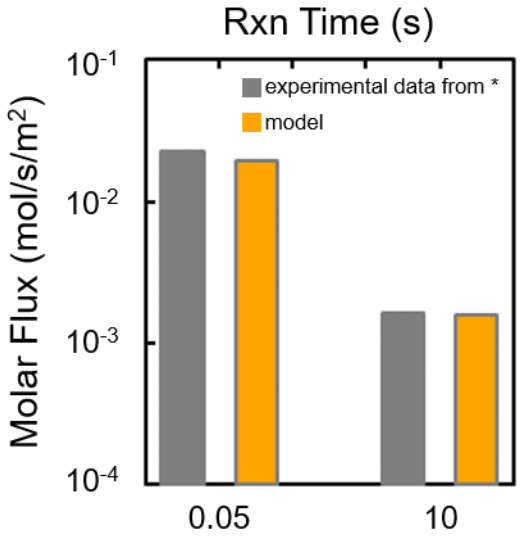

Figure 7-16: Molar flux from solution of the model developed is in high agreement with literature values from previously published textbook for short reaction times of 0.05 s and long reaction times of 10 s. Reference for data comparison from * Sherwood, T. K., Pigford, R. L., & Wilke, C. R. (1975). *Mass Transfer*. McGraw-Hill.

7.2.4. Experimental & Imaging Setup

Imaging data for non-spreading captive bubbles was collected at 30 frames per second as videos using a DSLR camera (Nikon D800) and high magnification lens (Navitar 12x Zoom). High-speed imaging data collected at higher frame rates was used to determine the average reaction rate for spreading bubbles, collected at 5,000 frames per second using a high-speed camera (Photron SA-1). For the embodiment shown of injection of the smallest bubbles tested, a higher frame of 40,000 frames per second was used to increase the temporal resolution of the data collection. The following figures show a photo of the experimental setup used to capture bubbles on a capture surface and image from the side profile, along with a schematic diagram of the setup used to enable single bubble control via using pressure regulated gas flow of CO_2 and precisely timed actuation of solenoid valves via a microcontroller to deposit a single bubble CO_2 on-demand.

Fabrication of Textured Capture Surfaces for Testing

Nanotexture, nanograss, "*ng*" capture surfaces are fabricated using a fluorine based reactive ion etching (RIE) process. Oxygen is introduced into the chamber during fluorine etching and causes for the formation of oxide precipitates which are deposited and subsequently etched to create the relatively random nanoscale features that produce the nanotexture of the "nanograss" texture that is achieved

Hierarchical "*low-phi*" capture surfaces are fabricated using a 1064 nm Nd:YAG laser (TYMKA Electrox) to ablate the surface of a polished silicon wafer. The ablation process was controlled to make a repeating raster pattern on the surface of the silicon which results in a hierarchical micro/nanotexture. The microscale pyramidal structures consisted of closely packed and reproducible pyramidal features spaced ~ 75 μm apart and 75 μm from the spacing between the raster pattern of the laser on the surface. The nanoscale roughness is created through the

thermal ablation process as the silicon is ablated from the surface, leaving a micro- / nanoscale hierarchical structure.

Microtextured "*b5*" capture surfaces were fabricated using a combination of photolithography and deep reactive ion etching processing (DRIE) to achieve a regular array of rectangular posts with a well-controlled spacing between them. In this case the microposts are 10 μm side lengths of the top square surface, 10 μm tall, and spaced 5 μm from adjacent microposts. This process is identical to the process used in Chapter 2 and summarized in the corresponding Appendix section as well.

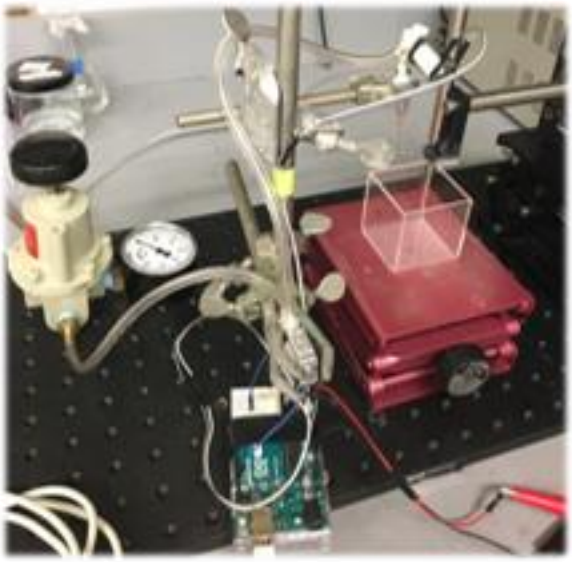

Figure 7-17: Photo of experimental setup for delivering single bubbles to capture surfaces during experiments relevant for Chapter 4 of this thesis.

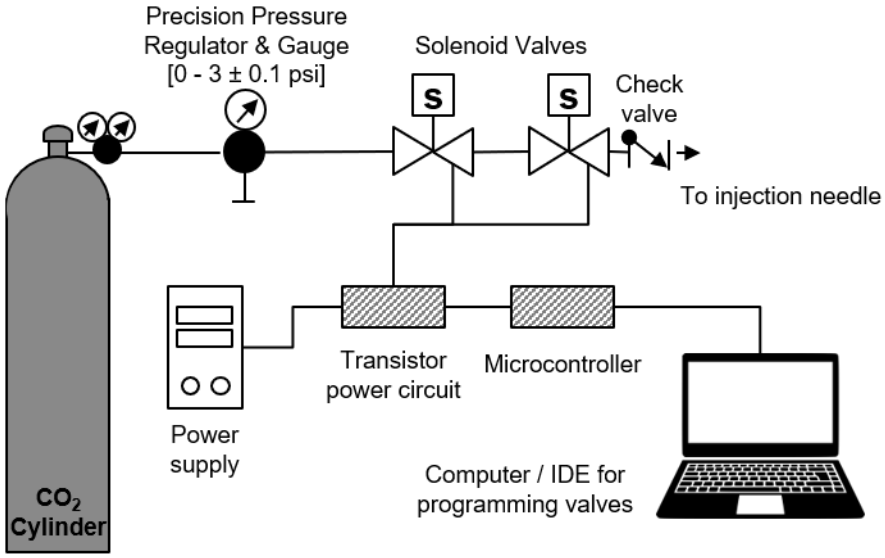

Figure 7-18: Schematic illustration of the experimental setup used to inject single bubbles via pressure driven flow through an injection needle using a pair of solenoid valves controlled via a microcontroller.

7.3. **Appendix C**: Transient Depletion of CO_2 during CO2RR Supplemental Information

7.3.1. Activation and Cleaning of Nafion Membrane

The Nafion membrane used in our experiments was purchased at Fuel Cell Store. Prior to the experiments, it needs to be activated to allow for the transmission of ions from one half of the H-cell to the other, but at the same time inhibit the passage of other species, such as gaseous and liquid products obtained from CO2RR. The following procedure, based on our experience and a combination of previously described methods from literature[254–258], indicates the steps taken to achieve a successful activation of the Nafion membrane:

1. Boiling in 3 % H_2O_2 (hydrogen peroxide) for 1 h.
2. Submersion in 0.1 M H_2SO_4 (sulfuric acid) overnight.
3. Boiling in DI water for 1 h.
4. Sonication in 0.1 M $KClO_4$ (potassium perchlorate) for 30 min.
5. Thorough rinse with DI water.

The Nafion layer should be kept submerged in DI water until necessary. To ensure that the cleaning process has been successfully accomplished, we track the appearance of bubbles on the membrane while it is resting prior to the experiments: a properly cleaned and activated membrane will lack bubbles attaching to its surface.

7.3.2. Preparation of electrocatalysts

As explained in the main text, copper, silver and gold were selected as electrocatalysts for our study due to their accessibility and selectivity to different products from CO2RR. To summarize, Ag and Au are very selective to CO whereas Cu provides a wide variety of liquid and gaseous

products, including high-carbon components (C2,3). To guarantee that the electrodes are at optimal conditions to perform CO2RR, each follows a specific preparation process due to the different ways in which each material reacts with its environment at standard conditions. To be more specific, copper spontaneously forms an oxide layer which covers its surface within minutes of being exposed to ambient air, whereas silver and gold are relatively stable and remain pure if they are kept submerged in DI water. We dedicate a specific subsection for each material used in this research.

Preparation of Cu electrodes

Cu wire of 99.999 % purity was purchased from Sigma-Aldrich. In this state, Cu is a material which is highly susceptible to oxidation, i.e. CuO appears within minutes on its surface[259]. Therefore, in order to ensure that CO2RR occurs on a Cu wire with the least experimentally achievable oxide layer blocking the access to the pure electrocatalyst, a process known as electropolishing is performed[260]. For that, we introduce the Cu coil in a phosphoric acid solution (> 85 wt. % in H_2O) and use a carbon rod as counter electrode. With a VSP potentiostat (BioLogic) and using the counter electrode also as the reference electrode, we perform a cyclic voltammogram (CV) from 0 to 3 V. At approximately 2 V (depending on the state of the Cu electrode, the amount of CuO deposited on top and the volume of electrolyte used), the current will reach a maximum and then drop (see Figure 7-19a). Afterwards, we run a chronoamperometry (CA) experiment for 10 minutes at the voltage in which the peak current occurred in the previous CV, Figure 7-19b. The electrode will be ready once it is rinsed with DI water after the CA. We have already mentioned that CuO may appear very rapidly in standard conditions, therefore CO2RR experiments were carried out immediately following the electropolishing procedure.

SEM (Scanning Electron Microscope) images of the electrode surface before and after the cleaning procedure and after experiments were done are shown in Figure 7-20. There is a significant improvement of the electrode condition after the cleaning prior to experiments, in which results from EDS (Energy Dispersive X-ray Spectroscopy) show that Figure 7-20a (before cleaning) only presents a 92 % purity (with presence of other contaminants such as oxides and silica), whereas Figure 7-20b shows indeed a purity of 99 % Cu. However, and as indicated before, copper is a very sensitive material which rapidly oxidizes, with oxidation beginning as soon as the electrode is introduced into the liquid electrolyte. After an experiment of 5 hours, Figure 7-20c, the purity of the electrode has decreased to 95 %. This is, together with the effect of gas depletion, one of the factors which contribute to the poor long-term performance of Cu electrodes as compared to other more stable materials such as silver or gold.

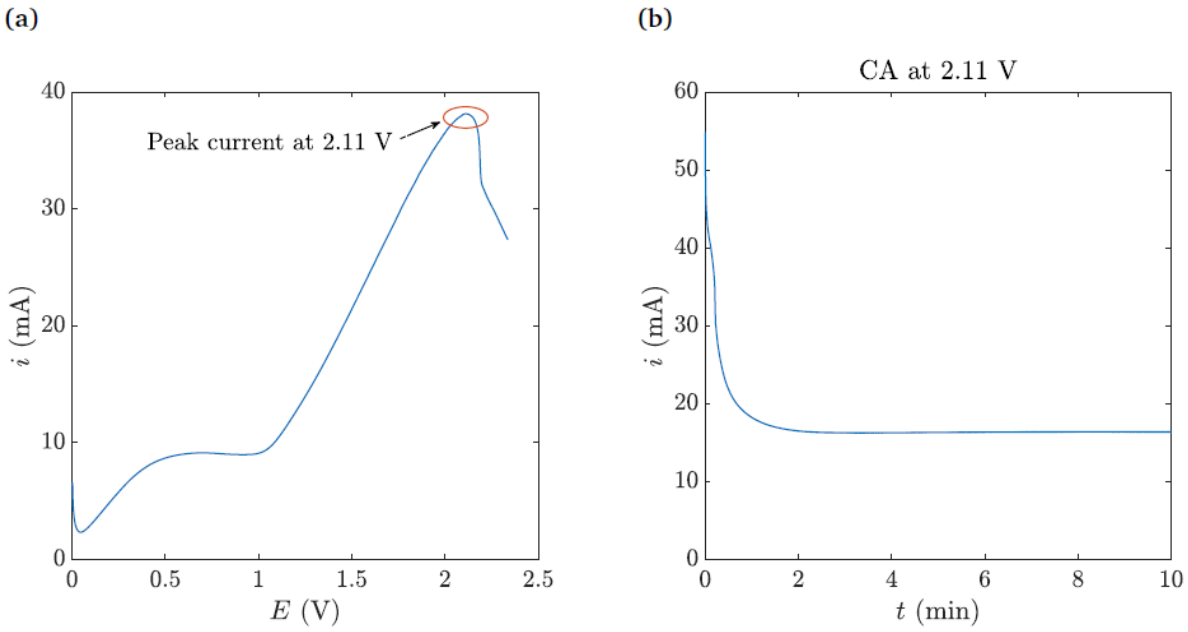

Figure 7-19: (a) CV to determine the voltage at which the peak current for the first step of the electropolishing procedure of Cu in a phosphoric acid solution occurs. (b) Final step of the electropolishing procedure: CA ran at the voltage at which the peak current in the previous CV is obtained. We can clearly see that the Cu wire has been fully electropolished after approximately 3 minutes of reaction (a steady-state condition is reached).

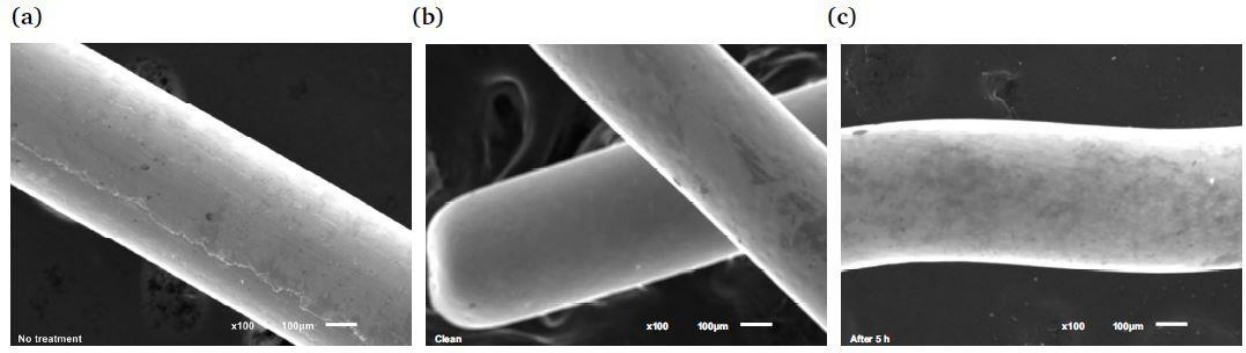

Figure 7-20: SEM images of the state of the Cu electrode (a) prior to and (b) after the cleaning process, and (c) after experiments. The magnification for the three images is 100 times and the scale bar represents 100 µm. There is clear evidence of the significant importance of the cleaning procedure to ensure an optimal CO_2 electroreduction. The detrimental effect of long-term exposure of copper to an aqueous reacting media can be observed by the visible deterioration of the electrode surface after a very long reaction.

Preparation of Ag electrodes

Ag wire of 99.999 % purity was purchased from Sigma-Aldrich. Even though silver is generally a very stable material, it can react when exposed to air and form silver sulfide (Ag_2S) and oxide (Ag_2O) [261]. While performing CO2RR, Ag is also known to absorb hydrocarbons, which may affect the electrocatalysis efficiency [262]. Therefore, active generation of hydrogen bubbles within the interstices of the Ag wire may remove the initial layer of sulfide / oxide while delaying the absorption of hydrocarbons[174,175]. The following procedure is performed accordingly to condition the electrode for CO2RR: first, the Ag wire is sonicated in ethanol for 10 minutes in order to weaken the bond between the sulfide / oxide layer to the pure electrocatalyst. This step is followed by a 5-minute sonication in DI water to facilitate the removal of that layer. Afterwards, the wire is submerged into a sulfuric acid solution (puriss. p.a., 25 %, Sigma-Aldrich) using Pt as counter electrode and an Ag/AgCl reference electrode (both from Pine Research Instrumentation). To generate a significant amount of H_2 bubbles, we run a chronopotentiometry (CP) cycle at -10 mA (the current could be ramped up to -15 mA if necessary) for 10 minutes (see Figure 7-21), followed by a 10-minute sonication in DI water. The electrode is used directly after the cleaning procedure. After the experiments, the electrode would be kept in DI water to avoid oxidation by exposing the metal surface directly to air.

Again, SEM images are presented in Figure 7-22. In this case, the electrode already comes in a very good condition directly from the manufacturer, Figure 7-22a, showing almost 99 % purity (with a very small presence of other contaminants such as silica). The cleaning process nevertheless im- proves the electrocatalyst purity to more than 99.5 %, Figure 7-22b. The long reacting time damages the surface of the electrode, Figure 7-22c, which is now contaminated by the deposition of carbon particles on its surface. Still, the purity remains higher than 98.5 %, which

is important to the stability of the long-term reaction. However, this purity may not be sufficient if the same electrode needs to be used for much longer times.

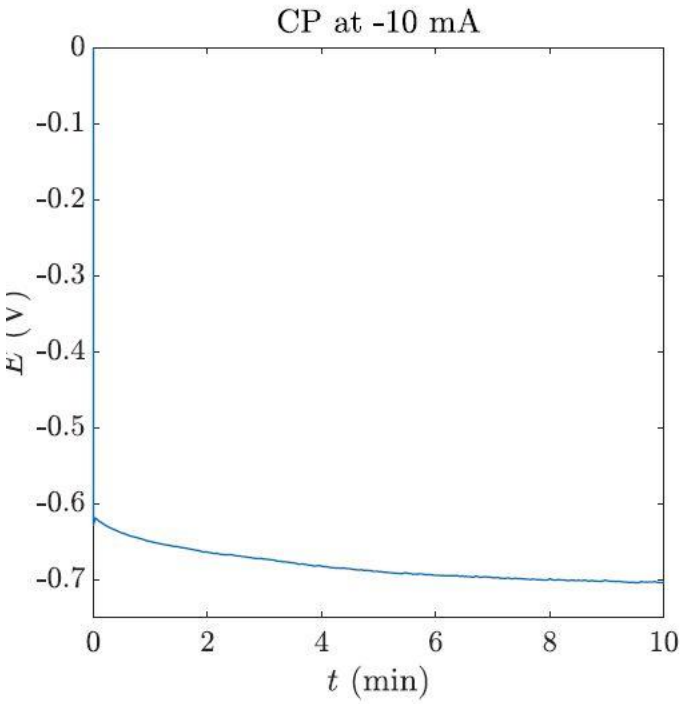

Figure 7-21: Chronopotentiometry experiment at -10 mA on an Ag wire of 2.36 cm^2 surface area in a H_2SO_4 solution using Pt and Ag/AgCl as counter and reference electrode, respectively. H_2 bubbles were vigorously generated during 10 minutes to actively remove contamination within the interstices of the electrode. The potential E is referred to an Ag/AgCl electrode.

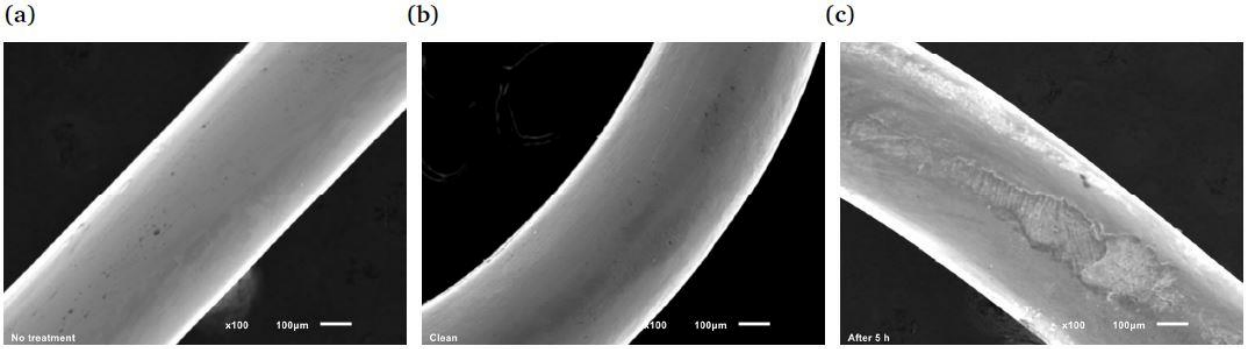

Figure 7-22: SEM images of the state of the Ag electrode (a) prior to the cleaning process, (b) after cleaning and (c) after experiments. The magnification for the three images is 100 times and the scale bar represents 100 µm. The damage caused by a long lasting CO2 electroreduction can be clearly depicted.

Preparation of Au electrodes

Gold, as well as Pt, are among the most stable materials used in chemical reactions, since they are not easily corrupted or contaminated. 99.999 %-purity gold wire from Sigma-Aldrich was used to perform CO2RR. Even though Au is very stable, the electrode needs to be preconditioned before experiments are performed, since there may be contaminating particles on its surface from its exposure to ambient air. Whereas the purpose of the cleaning procedure for Cu and Ag are dedicated to remove sulfide or oxide layers that may be deposited on the electrocatalyst, the procedure for Au only involves dirt removal and surface conditioning.

First, we sonicate the wire in DI water for 10 minutes. In order to condition the surface of the electrode[263,264], we run two subsequent CVs in different media: to adapt the gold surface to the liquid medium (electrolyte) in which CO2RR is going to take place, we implement a CV from -200 mV to -1200 mV at 50 mV s^{-1} for 10 cycles in a 0.1 M $KHCO_3$ solution[265,266], see Figure 7-23a; to adapt the electrode to the potential production of H_2 gas and to remove contaminants from within its interstices, a CV from -400 mV to 1400 mV at 100 mV/s for 10 cycles in a H_2SO_4 solution (puriss. p.a. 25 %, Sigma-Aldrich) is carried out, Figure 7-23b. The surface chemistry for this last CV shows that in the negative potential zone and moving towards more negative potential, the electrode surface adsorbs H, whereas looping back towards more positive values indicates H desorption from the Au surface [263,264]. For both CVs, a Pt and Ag/AgCl counter and reference electrode are respectively used. As a final step, we sonicate the Au wire in DI water for 10 minutes. After experiments, the Au electrode is kept in DI water to avoid contact with open air.

This cleaning procedure is critical to obtain optimal results from our CO2RR experiments. SEM images are shown in Figure 7-24 from the electrode state before and after the cleaning

procedure and after experiments are done. There is clearly a significant improvement from the electrode condition after the cleaning prior to experiments, in which results from EDS show that Figure 7-24a (before cleaning) only presents a 92% purity (with presence of other contaminants such as carbon, oxygen and calcium), whereas Figure 7-24b and Figure 7-24c present indeed more than 99% Au (without remarkable differences between the two of them). A proper cleaning process is therefore critical to obtain optimal results from our chemical process.

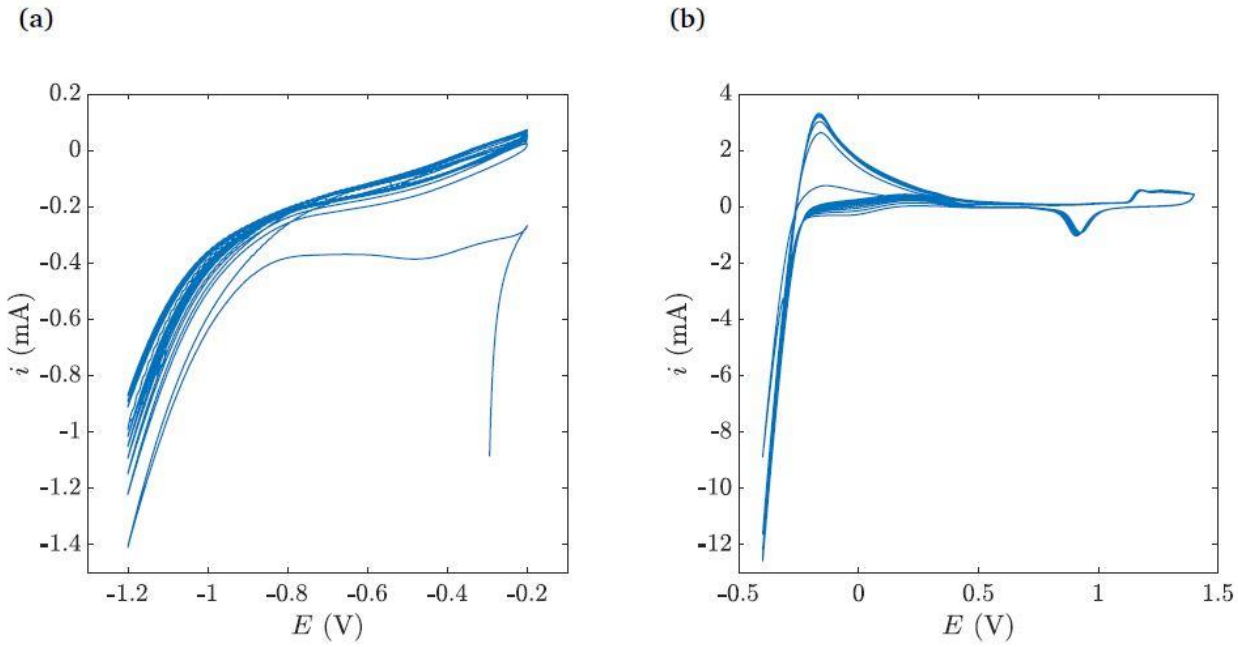

Figure 7-23: (a) First step of the conditioning procedure for gold electrodes: CV from -200 mV to -1200 mV at 50 mV s^{-1} for 10 cycles in 0.1 M $KHCO_3$. After a couple of cycles, stability is reached. (b) Second step of the conditioning procedure: CV from -400 mV to 1400 mV at 100 mV s−1 for 10 cycles in a H_2SO_4 solution. In the negative potential regime, when voltage is looping towards more negative values, H+ protons are adsorbed into the metal, whereas moving towards positive potential they are desorbed. The potential E is referred to an Ag/AgCl electrode.

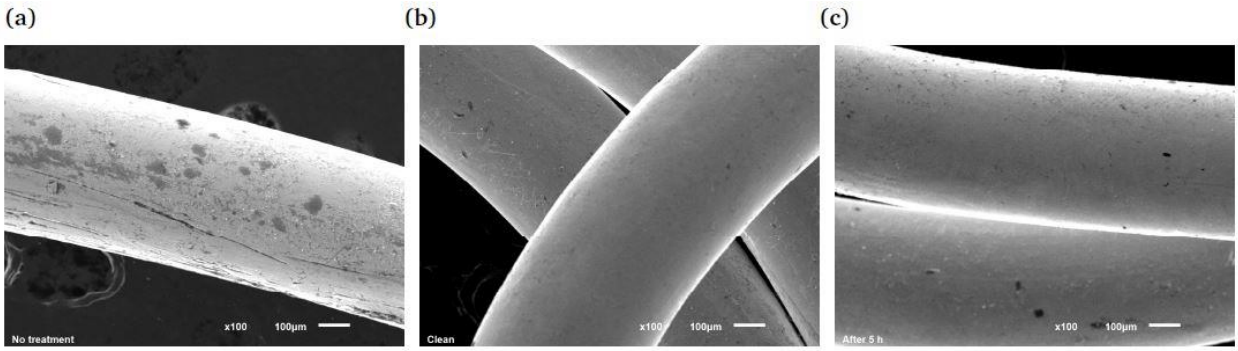

Figure 7-24: SEM images of the surface state of the Au electrode (a) prior to (b) and after the cleaning process, and (c) after experiments. The magnification for the three images is 100 times and the scale bar represents 100 µm. The cleaning procedure ensures an optimal condition to perform CO_2 electroreduction. The stability remains after the experiments due to the intrinsic properties of the material.

7.3.3. Calculation of the Different Faradaic Efficienies for CO2RR

The calculation of the Faradaic efficiencies for the different products obtained during CO2RR is based on Faraday's law of electrolysis:

$$i = \frac{mFz}{Mt} = \frac{nFz}{t} \quad (1)$$

where m is the mass of the product, F = 96485 C mol^{-1} is Faraday's constant, z is the valence of the reaction, M is the molecular weight of the product, n the corresponding number of moles and t the reaction time. By this equation, we can use the measured molar amount of each product that is generated from the chemical reaction and calculate the corresponding partial current $i_{partial}$. There is however a different methodology depending on the instruments by which the different components are measured.

The analysis of GC (Gas Chromatographer) data

The Gas Chromatographer takes a sample of gas from our H-cell every 14 minutes, and measures the molar parts per million (ppm) of each detected component following a calibration chart based on the analysis of a customized gas precision calibration mixture (Gasco and Shopcross). Those ppm values can be translated into molar fractions, i.e. $x_i = ppm_i/ppm_{total}$, where subindex i stands for the different products.

To flow the produced gas samples for analysis into the GC loop, CO_2 is flown through the working electrode side of the H-cell. The analyte gas stream passes through the GC sample loop at a constant flow rate of 20 sccm that we control via a digital flowmeter (Cole-Parmer). According to the ideal gas law, $PV = nRT$ (where P is the pressure in Pa, V the volume in m^3, R = 8.31442 J mol^{-1}K^{-1}, and T the temperature in K), at standard conditions and given the volume, the number of moles can be calculated. Indeed, the measurement of the flow rate, $\dot{V}$, can be readily used to

calculate $\dot{n}$ as $\dot{n} = P\dot{V}/(RT)$. By knowing the molar fractions xi, we can calculate the partial molar rate n˙i = n˙xi for each component of the reaction.

$$i = \frac{mFz}{Mt} = \dot{n}Fz \quad (2)$$

Finally, the faradaic efficiency for each product can be directly calculated:

$$F_{eff,i} = \frac{i_{partial,i}}{i_{total}} = \frac{\dot{n}Fz_i}{i_{total}} \quad (3)$$

The analysis of NMR (Nuclear Magnetic Resonance) data

NMR is exclusively dedicated to the analysis of liquid products. Samples of 700 µl are pipetted in NMR glass tubes and mixed with 35 µl 100 mM DMSO and 100 mM phenol in D_2O standard (for calibration purposes). The report obtained after the analysis with a Bruker 402 instrument is then interpreted with the software MestReNova. Such a file contains the frequencies where the device could detect electron vibrations within each of the liquid components. Therefore, peaks at certain frequencies correspond to the presence of a certain liquid. By knowing the exact concentration of the calibration liquid, we can compare the areas under those peaks with the areas corresponding to the calibration products. The ratio between those areas is an indicative of the concentration of a certain product *i* within the liquid sample. This ratio depends on the product, and therefore, multiple experiments had to be done to calculate the proportionality between the areas corresponding to a certain product and the calibrating components. Once those proportions are found and the calibration constants have been calculated, we can obtain the desired concentrations.

Once we have measured a certain product molar concentration and given the total volume of liquid used for the experiments (35 ml in our case), the total amount of moles produced during the

reaction can be determined. Again, we only need to input the time at which the sample was taken, the number of moles and the valence of the reaction into Faraday's law, Equation (2), to compute the partial current dedicated to generate such product. Once this is known, F_{eff} can be directly obtained by diving $i_{partial}$ by i_{total}.

7.3.4. Solution of the Equilibrium System of Equations for CO_2 Dissolution

For convenience, we write in the following the equilibrium equations for CO_2 dissolution in an aqueous solution of moderate ionic strength[231–234]:

$$CO_2(g) \leftrightarrow CO_2(aq) \text{ with } pK_0 = -2622.38/T - 0.0178471 \times T + 15.5873 \quad (4)$$

$$CO_2(aq) + H_2O \leftrightarrow H^+ + HCO_3^- \text{ with } pK_1 = 3404.71/T + 0.032786 \times T - 14.8435 \quad (5)$$

$$HCO_3^- \leftrightarrow H^+ + CO_3^{-2} \text{ with } pK_2 = 2902.39/T + 0.02379 \times T - 6.4980 \quad (6)$$

$$H_2O \leftrightarrow H^+ + OH^- \text{ with } K_w = \exp(148.9802 - 13847.26/T - 23.6521 \log(T)) \quad (7)$$

The equilibrium constants are defined both in their K and pK form, being both parameters related by $K = 10^{-pK}$. T corresponds to the absolute temperature in Kelvin. We analyze in the following each formula independently. Equation (4) corresponds to Henry's Law[228,229]:

$$[CO_2(aq)] = K_0 P \quad (8)$$

where magnitudes between brackets indicate concentration. Equation (5) can be expressed in terms of concentrations and the corresponding equilibrium constant:

$$K_1[H_2CO_3] = [H^+][HCO_3^-] \quad (9)$$

H_2CO_3 stands for the carbonic acid which is generated by the dissolution of CO_2 in water. Generally, this amount will be significantly lower than the total $CO_2(aq)$. However, under steady state conditions, it can be assumed that $CO_2(aq)$ equals the total carbonic acid in the solution, i.e. $[CO_2(aq)] = [H_2CO_3]$. Similarly, Equation (6):

$$K_2[HCO_3^-] = [H^+][CO_3^{-2}] \quad (10)$$

and finally, Equation (7):

$$K_w = [H^+][OH^-] \quad (11)$$

One more equation is needed to close the system: ion neutrality. This equation enforces neutral charge in the solution to guarantee stability in the absence of an electric field:

$$[HCO_3^-] + 2[CO_3^{-2}] + [OH^-] = [K^+] + [H^+] \quad (12)$$

Combining Equations (8) - (12), a single equation is reached:

$$[H^+]^3 + [K^+][H^+]^2 - (K_1 K_0 P + K_w)[H^+] - 2K_2 K_1 K_0 P = 0 \quad (13)$$

which corresponds to Equation (5) in the main text and that can be readily solved knowing that P = 1 atm (standard conditions), T = 293.15 K and K^+ = 0.1 M from a 0.1 M $KHCO_3$ electrolyte solution. The unknown $[H^+]$ can be directly calculated and automatically associated to pH by pH = $-\log([H^+])$. For a CO_2 saturated electrolyte, a pH level of 6.79 is determined.

7.3.5. Equilibrium State Recovery After OH^- and / or CO_2

For a carbonated solution system in equilibrium, the concentration of ions is determined by the environmental conditions (temperature T and pressure P), the salt concentration in the system (salt molarity in dissolution) and the gas saturation level. In the previous section, we described the equilibrium equations for a 0.1 M KOH solution saturated with CO_2 at standard conditions, i.e. 0.1 M $KHCO_3$ solution. In such a case, the equilibrium concentration of each carbonic derivative corresponds to:

$$[CO_2(aq)] = 0.0394\ \text{M},\ [HCO_3^-] = 0.0999\ \text{M},\ [CO_3^{-2}] = 2.563 \times 10^{-5}\ \text{M}$$
$$[OH^-] = 4.176 \times 10^{-8}\ \text{M},\quad [H^+] = 1.638 \times 10^{-7}\ \text{M} \qquad (14)$$

with the last concentration obeying $pH = -\log([H^+])$.

When a reaction starts, there is a sudden increase in the ionic concentration of OH^- originated by the release of electrons and protons, i.e. for each proton and electron consumed in the reaction to recombine and generate the CO2RR products, there is a hydroxide ion being released into the system (proton balance)[230]. Therefore, a sudden increase in that concentration triggers the compensating mechanisms to bring back the solution to an equilibrium state. This similarly occurs when CO_2 is being consumed at the electrode and therefore its concentration decreases. As the solution becomes more basic, i.e. higher $[OH^-]$ or lower $[CO_2(aq)]$, the equilibrium Equations (4 - 7) can be rewritten in their conjugated form:

$$CO_2(g) \leftrightarrow CO_2(aq) \text{ equals Equation (4)} \qquad (15)$$
$$CO_2(aq) + OH^- \leftrightarrow HCO_3^- + H_2O \text{ with } K_{b1} \qquad (16)$$
$$HCO_3^- + OH^- \leftrightarrow CO_3^{-2} + H_2O \text{ with } K_{b2} \qquad (17)$$
$$H_3O^+ + OH^- \leftrightarrow 2H_2O \text{ with } K_w \qquad (18)$$

H_3O^+ stands for the hydronium ion and is equivalent to an aqueous cation / proton. The equilibrium constants K_{b1} and K_{b2} are the conjugates of K_1 and K_2, respectively, and follow $K_w = K_iK_{bi}$.

Let's name A, B, C, D, E and F the equilibrium concentrations $[CO_2(aq)]$, $[HCO_3^-]$, $[CO_3^{-2}]$, $[OH^-]$, $[H_3O^+]$ and $[H_2O]$, respectively. When a sudden change in the concentration of hydroxide ions ΔOH^- or a decrease in reactant concentration ΔCO_2 occurs, each Equation (16 - 18) needs to equilibrate by increasing or decreasing the number of existing ions in solution. Having x_1, x_2 *and* x_3 represent the unknown concentration changes that Equations (16), (17) and (18) respectively entail, we can write the following system of equations:

$$(A - \Delta CO_2 - x_1) + (D + \Delta OH^- - x_3 - x_2 - x_1) \leftrightarrow (B - x_2 + x_1) + (F + x_3 + x_2 + x_1) \quad (19)$$

$$(B - x_2 + x_1) + (D + \Delta OH^- - x_3 - x_2 - x_1) \leftrightarrow (C + x_2) + (F + x_3 + x_2 + x_1) \quad (20)$$

$$(E - x_3) + (D + \Delta OH^- - x_3 - x_2 - x_1) \leftrightarrow 2(F + x_3 + x_2 + x_1) \quad (21)$$

By using the definition of each equilibrium constant, we reach the following relations:

$$(A - \Delta CO_2 - x_1)(D + \Delta OH^- - x_3 - x_2 - x_1) = K_{b1}(B - x_2 + x_1) \quad (22)$$

$$(B - x_2 + x_1)(D + \Delta OH^- - x_3 - x_2 - x_1) = K_{b2}(C + x_2) \quad (23)$$

$$(E - x_3)(D + \Delta OH^- - x_3 - x_2 - x_1) = K_w \quad (24)$$

The unknowns x_1, x_2 *and* x_3 are considered subtracting values of the hydroxide ion concentration since $\Delta OH-$ is positive and the system tends to a bring that concentration down to the original level. ΔCO_2 is regarded as a subtracting value since the CO_2 is only consumed and never produced. Equations (22 - 24) form a system of three equations with three unknowns, which can be directly solved to obtain the corresponding equilibrating trend of each ion due to $\Delta OH-$ and / or ΔCO_2. Results are shown in the main text in Figure 7-23.

7.3.6. Solution of the Mass Diffusion Equation for CO_2 Depletion

The diffusive mass transfer equation accounting for the CO_2 transport in the electrolyte and neglecting the ionic transfer in the system reads as follows (Equations (5.6-8) in Chapter 5):

$$\frac{\partial \Delta CO_2}{\partial t} = D\frac{1}{r^2}\frac{\partial}{\partial r}\left(r^2\frac{\partial \Delta CO_2}{\partial r}\right) \quad (25)$$

with boundary conditions:

$$\Delta CO_2(t=0,r)=0 \quad (26a)$$

$$\Delta CO_2(t,r\to\infty)=0 \quad (26b)$$

$$\lim_{\epsilon\to r_e} 2\pi\epsilon LD\frac{\partial \Delta CO_2}{\partial r}|_{r\to\epsilon} = \dot{m} \quad (26c)$$

with

$$\dot{m}=\sum\dot{m}_i=\sum\frac{i_{partial,i}M_i}{Fz_i}=\sum\frac{i_{total}F_{eff,i}M_i}{Fz_i}=\frac{i_{total}}{F}\sum\frac{F_{eff,i}M_i}{z_i} \quad (27)$$

Here, D is the diffusion coefficient of CO_2 in the 0.1 M $KHCO_3$ solution [237–239], r is the radial coordinate with origin the center of the electrocatalyst coil, r_e is the radius of the electrode wire and $\dot{m}$ is the mass consumption rate defined using Faraday's law, with i the current, F Faraday's constant, F_{eff} the Faradaic efficiency, M the molecular weight and z the valence of the reaction. Subindex i indicates the different products from CO2RR not including H_2, as specified in the main text.

By means of defining dimensionless variables:

$$X=\frac{r}{\sqrt{Dt}} \qquad Y=\frac{\Delta CO_2 Dr}{\dot{m}} \quad (28)$$

and substituting in the previous system, the partial differential equation becomes an ordinary differential equation:

$$-\frac{1}{2}X\frac{dY}{dX}=\frac{d^2X}{dX^2} \qquad (29)$$

with boundary conditions:

$$y(X\to\infty)=0 \qquad (30a)$$

$$\lim_{\epsilon\to r_e}\left(X\frac{dY}{dX}-Y\right)=\frac{r_e}{2\pi L} \qquad (30b)$$

Following the same procedure as in Moreno Soto *et al.*[235], the solution to the system is found:

$$\Delta CO_2=\frac{\sqrt{\pi}r_e\dot{m}}{2\pi LDr\left(\left(\frac{r_e}{\sqrt{Dt}}\right)\exp\left(-\frac{r_e^2}{4Dt}\right)+\sqrt{\pi}\,erfc\left(\frac{r_e}{2\sqrt{Dt}}\right)\right)}erfc\left(\frac{r}{2\sqrt{Dt}}\right) \qquad (31)$$

This equation can be further simplified by acknowledging that $r_e\sqrt{Dt}\ll 1$ within the first 5 minutes of reaction. That way, the depletion model finally reads:

$$\Delta CO_2=-\frac{r_e}{2\pi LDr}\dot{m}\,erfc\left(\frac{r}{2\sqrt{Dt}}\right) \qquad (32)$$

THIS PAGE INTENTIONALLY LEFT BLANK

8. Bibliography

(1) *Advanced Chlor-Alkali Technology*. U.S. Dept. of Energy, Office of Energy Efficiency and Renewable Energy. https://www1.eere.energy.gov/manufacturing/industries_technologies/imf/pdfs/1797_advanced_chlor-alkali.pdf (accessed 2021-12-03).

(2) Angulo, A.; van der Linde, P.; Gardeniers, H.; Modestino, M.; Fernández Rivas, D. Influence of Bubbles on the Energy Conversion Efficiency of Electrochemical Reactors. *Joule*. Cell Press March 18, 2020, pp 555–579. https://doi.org/10.1016/j.joule.2020.01.005.

(3) Zeradjanin, A. R.; Grote, J. P.; Polymeros, G.; Mayrhofer, K. J. J. A Critical Review on Hydrogen Evolution Electrocatalysis: Re-Exploring the Volcano-Relationship. *Electroanalysis* **2016**, *28* (10), 2256–2269. https://doi.org/10.1002/ELAN.201600270.

(4) Gong, M.; Wang, D. Y.; Chen, C. C.; Hwang, B. J.; Dai, H. A Mini Review on Nickel-Based Electrocatalysts for Alkaline Hydrogen Evolution Reaction. *Nano Res* **2016**, *9* (1), 28–46. https://doi.org/10.1007/s12274-015-0965-x.

(5) Voiry, D.; Shin, H. S.; Loh, K. P.; Chhowalla, M. Low-Dimensional Catalysts for Hydrogen Evolution and CO2 Reduction. *Nature Reviews Chemistry 2018 2:1* **2018**, *2* (1), 1–17. https://doi.org/10.1038/s41570-017-0105.

(6) Suen, N. T.; Hung, S. F.; Quan, Q.; Zhang, N.; Xu, Y. J.; Chen, H. M. Electrocatalysis for the Oxygen Evolution Reaction: Recent Development and Future Perspectives. *Chem Soc Rev* **2017**, *46* (2), 337–365. https://doi.org/10.1039/C6CS00328A.

(7) Song, J.; Wei, C.; Huang, Z. F.; Liu, C.; Zeng, L.; Wang, X.; Xu, Z. J. A Review on Fundamentals for Designing Oxygen Evolution Electrocatalysts. *Chem Soc Rev* **2020**, *49* (7), 2196–2214. https://doi.org/10.1039/C9CS00607A.

(8) Ahn, S. H.; Choi, I.; Park, H.-Y.; Hwang, S. J.; Yoo, S. J.; Cho, E.; Kim, H.-J.; Henkensmeier, D.; Nam, S. W.; Kim, S.-K.; Jang, J. H. Effect of Morphology of Electrodeposited Ni Catalysts on the Behavior of Bubbles Generated during the Oxygen Evolution Reaction in Alkaline Water Electrolysis. *Chemical Communications* **2013**, *49* (81), 9323. https://doi.org/10.1039/c3cc44891f.

(9) Ho, C. N.; Hwang, B. J. Effect of Hydrophobicity on the Hydrophobic-Modified Polytetrafluoroethylene/PbO2 Electrode towards Oxygen Evolution. *Journal of Electroanalytical Chemistry* **1994**, *377* (1–2), 177–190. https://doi.org/10.1016/0022-0728(94)03453-2.

(10) Dukovic, J.; Tobias, C. W. Influence of Attached Bubbles on Potential Drop and Current Distribution at Gas-Evolving Electrodes. In *Proceedings - The Electrochemical Society*; The Electrochemical Society, 1986; Vol. 86–12, pp 122–147. https://doi.org/10.1149/1.2100456.

(11) Vogt, H. Gas-Evolving Electrodes. In *Comprehensive Treatise of Electrochemistry*; Springer US: Boston, MA, 1983; pp 445–489. https://doi.org/10.1007/978-1-4615-6690-8_7.

(12) Gabrielli, C.; Huet, F.; Keddam, M.; Macias, A.; Sahar, A. Potential Drops Due to an Attached Bubble on a Gas-Evolving Electrode. *J Appl Electrochem* **1989**, *19* (5), 617–629. https://doi.org/10.1007/BF01320636.

(13) Vogt, H. The Rate of Gas Evolution at Electrodes—II. An Estimate of the Efficiency of Gas Evolution on the Basis of Bubble Growth Data. *Electrochim Acta* **1984**, *29* (2), 175–180. https://doi.org/10.1016/0013-4686(84)87044-9.

(14) Wüthrich, R.; Comninellis, Ch.; Bleuler, H. Bubble Evolution on Vertical Electrodes under Extreme Current Densities. In *Electrochimica Acta*; Pergamon, 2005; Vol. 50, pp 5242–5246. https://doi.org/10.1016/j.electacta.2004.12.052.

(15) Taqieddin, A.; Allshouse, M. R.; Alshawabkeh, A. N. Mathematical Formulations of Electrochemically Gas-Evolving Systems. *J Electrochem Soc* **2018**, *165* (13), E694–E711. https://doi.org/10.1149/2.0791813jes.

(16) Zhang, D.; Zeng, K. Evaluating the Behavior of Electrolytic Gas Bubbles and Their Effect on the Cell Voltage in Alkaline Water Electrolysis. *Ind Eng Chem Res* **2012**, *51* (42), 13825–13832. https://doi.org/10.1021/IE301029E.

(17) Zhao, X.; Ren, H.; Luo, L. Gas Bubbles in Electrochemical Gas Evolution Reactions. *Langmuir* **2019**, *35* (16), 5392–5408. https://doi.org/10.1021/acs.langmuir.9b00119.

(18) Gabrielli, C.; Huet, F.; Nogueira, R. P. Fluctuations of Concentration Overpotential Generated at Gas-Evolving Electrodes. *Electrochim Acta* **2005**, *50* (18), 3726–3736. https://doi.org/10.1016/j.electacta.2005.01.019.

(19) Peñas, P.; van der Linde, P.; Vijselaar, W.; van der Meer, D.; Lohse, D.; Huskens, J.; Gardeniers, H.; Modestino, M. A.; Rivas, D. F. Decoupling Gas Evolution from Water-Splitting Electrodes. *J Electrochem Soc* **2019**, *166* (15), H769–H776. https://doi.org/10.1149/2.1381914jes.

(20) Brussieux, C.; Viers, Ph.; Roustan, H.; Rakib, M. Controlled Electrochemical Gas Bubble Release from Electrodes Entirely and Partially Covered with Hydrophobic Materials. *Electrochim Acta* **2011**, *56* (20), 7194–7201. https://doi.org/10.1016/j.electacta.2011.04.104.

(21) Van Der Linde, P.; Peñas-López, P.; Moreno Soto, Á.; Van Der Meer, D.; Lohse, D.; Gardeniers, H.; Fernández Rivas, D. Gas Bubble Evolution on Microstructured Silicon Substrates. *Energy Environ Sci* **2018**, *11* (12), 3452–3462. https://doi.org/10.1039/c8ee02657b.

(22) Van Der Linde, P.; Moreno Soto, Á.; Peñas-López, P.; Rodríguez-Rodríguez, J.; Lohse, D.; Gardeniers, H.; Van Der Meer, D.; Fernández Rivas, D. Electrolysis-Driven and Pressure-Controlled Diffusive Growth of Successive Bubbles on Microstructured Surfaces. *Langmuir* **2017**, *33* (45), 12873–12886. https://doi.org/10.1021/acs.langmuir.7b02978.

(23) Lu, Z.; Zhang, L.; Iwata, R.; Wang, E. N.; Grossman, J. C. Transport-Based Modeling of Bubble Nucleation on Gas Evolving Electrodes. *Langmuir* **2020**, *36* (49), 15112–15118. https://doi.org/10.1021/acs.langmuir.0c02690.

(24) Long, Z.; Zhao, Y.; Zhang, C.; Zhang, Y.; Yu, C.; Wu, Y.; Ma, J.; Cao, M.; Jiang, L. A Multi-Bioinspired Dual-Gradient Electrode for Microbubble Manipulation toward Controllable Water Splitting. *Advanced Materials* **2020**, *32* (17), 1908099. https://doi.org/10.1002/adma.201908099.

(25) Hossain, S. S.; Mutschke, G.; Bashkatov, A.; Eckert, K. The Thermocapillary Effect on Gas Bubbles Growing on Electrodes of Different Sizes. *Electrochim Acta* **2020**, *353*, 136461. https://doi.org/10.1016/j.electacta.2020.136461.

(26) Yang, X.; Baczyzmalski, D.; Cierpka, C.; Mutschke, G.; Eckert, K. Marangoni Convection at Electrogenerated Hydrogen Bubbles. *Physical Chemistry Chemical Physics* **2018**, *20* (17), 11542–11548. https://doi.org/10.1039/c8cp01050a.

(27) Li, S. De; Wang, C. C.; Chen, C. Y. Water Electrolysis in the Presence of an Ultrasonic Field. *Electrochim Acta* **2009**, *54* (15), 3877–3883. https://doi.org/10.1016/J.ELECTACTA.2009.01.087.

(28) Liu, H. B.; Zhong, D.; Han, J.; Pan, L. M.; Liu, Y. Hydrogen Bubble Evolution from Magnetized Nickel Wire Electrode. *Int J Hydrogen Energy* **2019**, *44* (60), 31724–31730. https://doi.org/10.1016/j.ijhydene.2019.10.063.

(29) Liu, H. bo; Hu, Q.; Pan, L. ming; Wu, R.; Liu, Y.; Zhong, D. Electrode-Normal Magnetic Field Facilitating Neighbouring Electrochemical Bubble Release from Hydrophobic Islets. *Electrochim Acta* **2019**, *306*, 350–359. https://doi.org/10.1016/j.electacta.2019.03.140.

(30) Brandon, N. P.; Kelsall, G. H. Growth Kinetics of Bubbles Electrogenerated at Microelectrodes. *J Appl Electrochem* **1985**, *15* (4), 475–484. https://doi.org/10.1007/BF01059288.

(31) Fernández, D.; Maurer, P.; Martine, M.; Coey, J. M. D.; Möbius, M. E. Bubble Formation at a Gas-Evolving Microelectrode. *Langmuir* **2014**, *30* (43), 13065–13074. https://doi.org/10.1021/la500234r.

(32) Bashkatov, A.; Hossain, S. S.; Yang, X.; Mutschke, G.; Eckert, K. Oscillating Hydrogen Bubbles at Pt Microelectrodes. *Phys Rev Lett* **2019**, *123* (21), 214503. https://doi.org/10.1103/PhysRevLett.123.214503.

(33) Bashkatov, A.; Yang, X.; Mutschke, G.; Fritzsche, B.; Hossain, S. S.; Eckert, K. Dynamics of Single Hydrogen Bubbles at Pt Microelectrodes in Microgravity. *Physical Chemistry Chemical Physics* **2021**, *23* (20), 11818–11830. https://doi.org/10.1039/D1CP00978H.

(34) Yang, X.; Karnbach, F.; Uhlemann, M.; Odenbach, S.; Eckert, K. Dynamics of Single Hydrogen Bubbles at a Platinum Microelectrode. *Langmuir* **2015**, *31* (29), 8184–8193. https://doi.org/10.1021/acs.langmuir.5b01825.

(35) Fujimura, T.; Hikima, W.; Fukunaka, Y.; Homma, T. Analysis of the Effect of Surface Wettability on Hydrogen Evolution Reaction in Water Electrolysis Using Micro-Patterned Electrodes. *Electrochem commun* **2019**, *101*, 43–46. https://doi.org/10.1016/j.elecom.2019.02.018.

(36) Iwata, R.; Zhang, L.; Wilke, K. L.; Gong, S.; He, M.; Gallant, B. M.; Wang, E. N. Bubble Growth and Departure Modes on Wettable/Non-Wettable Porous Foams in Alkaline Water Splitting. *Joule* **2021**, *5* (4), 887–900. https://doi.org/10.1016/J.JOULE.2021.02.015.

(37) Kempler, P. A.; Coridan, R. H.; Lewis, N. S.; Lewis, N. S. Effects of Bubbles on the Electrochemical Behavior of Hydrogen-Evolving Si Microwire Arrays Oriented against Gravity. *Energy Environ Sci* **2020**, *13* (6), 1808–1817. https://doi.org/10.1039/d0ee00356e.

(38) Kempler, P. A.; Ifkovits, Z. P.; Yu, W.; Carim, A. I.; Lewis, N. S. Optical and Electrochemical Effects of H 2 and O 2 Bubbles at Upward-Facing Si Photoelectrodes. *Energy Environ Sci* **2021**, *14* (1), 414–423. https://doi.org/10.1039/D0EE02796K.

(39) Kempler, P. A.; Richter, M. H.; Cheng, W.-H.; Brunschwig, B. S.; Lewis, N. S. Si Microwire-Array Photocathodes Decorated with Cu Allow CO 2 Reduction with Minimal Parasitic Absorption of Sunlight. *ACS Energy Lett* **2020**, *4*, 2021. https://doi.org/10.1021/acsenergylett.0c01334.

(40) Oh, D.; Qi, J.; Lu, Y. C.; Zhang, Y.; Shao-Horn, Y.; Belcher, A. M. Biologically Enhanced Cathode Design for Improved Capacity and Cycle Life for Lithium-Oxygen Batteries. *Nature Communications 2013 4:1* **2013**, *4* (1), 1–8. https://doi.org/10.1038/ncomms3756.

(41) Sheberla, D.; Bachman, J. C.; Elias, J. S.; Sun, C. J.; Shao-Horn, Y.; Dincă, M. Conductive MOF Electrodes for Stable Supercapacitors with High Areal Capacitance. *Nature Materials 2016 16:2* **2016**, *16* (2), 220–224. https://doi.org/10.1038/nmat4766.

(42) Salanne, M.; Rotenberg, B.; Naoi, K.; Kaneko, K.; Taberna, P. L.; Grey, C. P.; Dunn, B.; Simon, P. Efficient Storage Mechanisms for Building Better Supercapacitors. *Nature Energy 2016 1:6* **2016**, *1* (6), 1–10. https://doi.org/10.1038/nenergy.2016.70.

(43) Lake, J. R.; Cheng, A.; Selverston, S.; Tanaka, Z.; Koehne, J.; Meyyappan, M.; Chen, B. Graphene Metal Oxide Composite Supercapacitor Electrodes. *Journal of Vacuum Science & Technology B* **2012**, *30* (3), 03D118. https://doi.org/10.1116/1.4712537.

(44) Paxson, A. T.; Varanasi, K. K. Self-Similarity of Contact Line Depinning from Textured Surfaces. *Nature Communications 2013 4:1* **2013**, *4* (1), 1–8. https://doi.org/10.1038/ncomms2482.

(45) Keçebaş, A.; Kayfeci, M.; Bayat, M. Electrochemical Hydrogen Generation. In *Solar Hydrogen Production: Processes, Systems and Technologies*; Academic Press, 2019; pp 299–317. https://doi.org/10.1016/B978-0-12-814853-2.00009-6.

(46) Vogt, H.; Balzer, R. J. The Bubble Coverage of Gas-Evolving Electrodes in Stagnant Electrolytes. *Electrochim Acta* **2005**, *50* (10), 2073–2079. https://doi.org/10.1016/J.ELECTACTA.2004.09.025.

(47) J. D. Hunter. Matplotlib: A 2D Graphics Environment. *In Computing in Science & Engineering* **2007**, *9* (3), 90–95.

(48) Liu, F.; Ghigliotti, G.; Feng, J. J.; Chen, C. H. Numerical Simulations of Self-Propelled Jumping upon Drop Coalescence on Non-Wetting Surfaces. *J Fluid Mech* **2014**, *752*, 39–65. https://doi.org/10.1017/JFM.2014.320.

(49) Lecointre, P.; Laney, S.; Michalska, M.; Li, T.; Tanguy, A.; Papakonstantinou, I.; Quéré, D. Unique and Universal Dew-Repellency of Nanocones. *Nature Communications 2021 12:1* **2021**, *12* (1), 1–9. https://doi.org/10.1038/s41467-021-23708-6.

(50) Boreyko, J. B.; Chen, C. H. Self-Propelled Dropwise Condensate on Superhydrophobic Surfaces. *Phys Rev Lett* **2009**, *103* (18), 184501. https://doi.org/10.1103/PHYSREVLETT.103.184501/FIGURES/5/MEDIUM.

(51) Moreno Soto, Á.; Maddalena, T.; Fraters, A.; van der Meer, D.; Lohse, D. Coalescence of Diffusively Growing Gas Bubbles. *J Fluid Mech* **2018**, *846*, 143–165. https://doi.org/10.1017/jfm.2018.277.

(52) Leaist, D. G. Diffusion in Aqueous Solutions of Sulfuric Acid. *Can J Chem* **1984**, *62* (9), 1692–1697. https://doi.org/10.1139/V84-290.

(53) Vogt, H. The Quantities Affecting the Bubble Coverage of Gas-Evolving Electrodes. *Electrochim Acta* **2017**, *235*, 495–499. https://doi.org/10.1016/j.electacta.2017.03.116.

(54) Vogt, H. Bubble Coverage of Gas-Evolving Electrodes in a Flowing Electrolyte. *Electrochim Acta* **2000**, *45* (27), 4449–4456. https://doi.org/10.1016/S0013-4686(00)00513-2.

(55) Vogt, H. The Actual Current Density of Gas-Evolving Electrodes—Notes on the Bubble Coverage. *Electrochim Acta* **2012**, *78*, 183–187. https://doi.org/10.1016/J.ELECTACTA.2012.05.124.

(56) Vogel, Y. B.; Evans, C. W.; Belotti, M.; Xu, L.; Russell, I. C.; Yu, L. J.; Fung, A. K. K.; Hill, N. S.; Darwish, N.; Gonçales, V. R.; Coote, M. L.; Swaminathan Iyer, K.; Ciampi, S. The Corona of a Surface Bubble Promotes Electrochemical Reactions. *Nature Communications 2020 11:1* **2020**, *11* (1), 1–8. https://doi.org/10.1038/s41467-020-20186-0.

(57) Chen, Q.; Zhao, J.; Deng, X.; Shan, Y.; Peng, Y. Single-Entity Electrochemistry of Nano- and Microbubbles in Electrolytic Gas Evolution. *J Phys Chem Lett* **2022**, *13* (26), 6153–6163. https://doi.org/10.1021/ACS.JPCLETT.2C01388.

(58) Ren, H.; German, S. R.; Edwards, M. A.; Chen, Q.; White, H. S. Electrochemical Generation of Individual O2 Nanobubbles via H2O2 Oxidation. *Journal of Physical Chemistry Letters* **2017**, *8* (11), 2450–2454. https://doi.org/10.1021/ACS.JPCLETT.7B00882/ASSET/IMAGES/LARGE/JZ-2017-00882J_0004.JPEG.

(59) Li, Z.; Hu, R.; Song, J.; Liu, L.; Qu, J.; Song, W.; Cao, C. Gas–Liquid–Solid Triphase Interfacial Chemical Reactions Associated with Gas Wettability. *Adv Mater Interfaces* **2021**, *8* (6), 2001636. https://doi.org/10.1002/ADMI.202001636.

(60) Iwata, R.; Zhang, L.; Wilke, K. L.; Gong, S.; He, M.; Gallant, B. M.; Wang, E. N. Bubble Growth and Departure Modes on Wettable/Non-Wettable Porous Foams in Alkaline Water Splitting. *Joule* **2021**, *5* (4), 887–900. https://doi.org/10.1016/J.JOULE.2021.02.015.

(61) Wu, H.; Wang, Y.; Shi, Z.; Wang, X.; Yang, J.; Xiao, M.; Ge, J.; Xing, W.; Liu, C. Recent Developments of Iridium-Based Catalysts for the Oxygen Evolution Reaction in Acidic Water Electrolysis. *J Mater Chem A Mater* **2022**, *10* (25), 13170–13189. https://doi.org/10.1039/D1TA10324E.

(62) Ismail, N.; Qin, F.; Fang, C.; Liu, D.; Liu, B.; Liu, X.; Wu, Z.; Chen, Z.; Chen, W. Electrocatalytic Acidic Oxygen Evolution Reaction: From Nanocrystals to Single Atoms. *Aggregate* **2021**, *2* (4), e106. https://doi.org/10.1002/AGT2.106.

(63) Zhang, B.; Zheng, X.; Voznyy, O.; Comin, R.; Bajdich, M.; García-Melchor, M.; Han, L.; Xu, J.; Liu, M.; Zheng, L.; de Arquer, F. P. G.; Dinh, C. T.; Fan, F.; Yuan, M.; Yassitepe, E.; Chen, N.; Regier, T.; Liu, P.; Li, Y.; de Luna, P.; Janmohamed, A.; Xin, H. L.; Yang, H.; Vojvodic, A.; Sargent, E. H. Homogeneously Dispersed Multimetal Oxygen-Evolving

Catalysts. *Science (1979)* **2016**, *352* (6283), 333–337. https://doi.org/10.1126/SCIENCE.AAF1525/SUPPL_FILE/ZHANG-SM.PDF.

(64) Xia, X.; Wang, L.; Sui, N.; Colvin, V. L.; Yu, W. W. Recent Progress in Transition Metal Selenide Electrocatalysts for Water Splitting. *Nanoscale* **2020**, *12* (23), 12249–12262. https://doi.org/10.1039/D0NR02939D.

(65) Song, J.; Wei, C.; Huang, Z. F.; Liu, C.; Zeng, L.; Wang, X.; Xu, Z. J. A Review on Fundamentals for Designing Oxygen Evolution Electrocatalysts. *Chem Soc Rev* **2020**, *49* (7), 2196–2214. https://doi.org/10.1039/C9CS00607A.

(66) Taylor, A. K.; Mou, T.; Sonea, A.; Chen, J.; Yee, B. B.; Gates, B. D. Arrays of Microscale Linear Ridges with Self-Cleaning Functionality for the Oxygen Evolution Reaction. *ACS Appl Mater Interfaces* **2021**, *13* (2), 2399–2413. https://doi.org/10.1021/ACSAMI.0C15240/SUPPL_FILE/AM0C15240_SI_007.MP4.

(67) Jamesh, M. I.; Sun, X. Recent Progress on Earth Abundant Electrocatalysts for Oxygen Evolution Reaction (OER) in Alkaline Medium to Achieve Efficient Water Splitting – A Review. *J Power Sources* **2018**, *400*, 31–68. https://doi.org/10.1016/J.JPOWSOUR.2018.07.125.

(68) Bakker, M. M.; Vermaas, D. A. Gas Bubble Removal in Alkaline Water Electrolysis with Utilization of Pressure Swings. *Electrochim Acta* **2019**, *319*, 148–157. https://doi.org/10.1016/J.ELECTACTA.2019.06.049.

(69) Zhang, K.; Jin, B.; Park, C.; Cho, Y.; Song, X.; Shi, X.; Zhang, S.; Kim, W.; Zeng, H.; Park, J. H. Black Phosphorene as a Hole Extraction Layer Boosting Solar Water Splitting of Oxygen Evolution Catalysts. *Nature Communications 2019 10:1* **2019**, *10* (1), 1–10. https://doi.org/10.1038/s41467-019-10034-1.

(70) Kim, T. W.; Choi, K. S. Nanoporous BiVO4 Photoanodes with Dual-Layer Oxygen Evolution Catalysts for Solar Water Splitting. *Science (1979)* **2014**, *343* (6174), 990–994. https://doi.org/10.1126/SCIENCE.1246913/SUPPL_FILE/KIM.SM.PDF.

(71) Li, Z.; Achenie, L. E. K.; Xin, H. An Adaptive Machine Learning Strategy for Accelerating Discovery of Perovskite Electrocatalysts. *ACS Catal* **2020**, *10* (7), 4377–4384. https://doi.org/10.1021/ACSCATAL.9B05248/ASSET/IMAGES/LARGE/CS9B05248_M013.JPEG.

(72) Jiang, X.; Wang, Y.; Jia, B.; Qu, X.; Qin, M. Prediction of Oxygen Evolution Activity for NiCoFe Oxide Catalysts via Machine Learning. *ACS Omega* **2022**, *7* (16), 14160–14164. https://doi.org/10.1021/ACSOMEGA.2C00776/ASSET/IMAGES/MEDIUM/AO2C00776_M028.GIF.

(73) Liu, J.; Luo, W.; Wang, L.; Zhang, J.; Fu, X. Z.; Luo, J. L. Toward Excellence of Electrocatalyst Design by Emerging Descriptor-Oriented Machine Learning. *Adv Funct Mater* **2022**, *32* (17), 2110748. https://doi.org/10.1002/ADFM.202110748.

(74) Ando, K.; Uchimoto, Y.; Nakajima, T. Concentration Profile of Dissolved Gas during Hydrogen Gas Evolution: An Optical Approach. *Chemical Communications* **2020**, *56* (92), 14483–14486. https://doi.org/10.1039/D0CC05695B.

(75) Kempler, P. A.; Ifkovits, Z. P.; Yu, W.; Carim, A. I.; Lewis, N. S. Optical and Electrochemical Effects of H 2 and O 2 Bubbles at Upward-Facing Si Photoelectrodes. *Energy Environ Sci* **2021**, *14* (1), 414–423. https://doi.org/10.1039/D0EE02796K.

(76) Suvira, M.; Zhang, B. Effect of Surfactant on Electrochemically Generated Surface Nanobubbles. *Anal Chem* **2021**, *93* (12), 5170–5176. https://doi.org/10.1021/ACS.ANALCHEM.0C05067/ASSET/IMAGES/LARGE/AC0C05067_0005.JPEG.

(77) Davis, J. T.; Brown, D. E.; Pang, X.; Esposito, D. v. High Speed Video Investigation of Bubble Dynamics and Current Density Distributions in Membraneless Electrolyzers. *J Electrochem Soc* **2019**, *166* (4), F312–F321. https://doi.org/10.1149/2.0961904JES/XML.

(78) Yang, X.; Karnbach, F.; Uhlemann, M.; Odenbach, S.; Eckert, K. Dynamics of Single Hydrogen Bubbles at a Platinum Microelectrode. *Langmuir* **2015**, *31* (29), 8184–8193. https://doi.org/10.1021/ACS.LANGMUIR.5B01825/SUPPL_FILE/LA5B01825_SI_001.PDF.

(79) Suh, Y.; Bostanabad, R.; Won, Y. Deep Learning Predicts Boiling Heat Transfer. *Scientific Reports 2021 11:1* **2021**, *11* (1), 1–10. https://doi.org/10.1038/s41598-021-85150-4.

(80) Hobold, G. M.; da Silva, A. K. Visualization-Based Nucleate Boiling Heat Flux Quantification Using Machine Learning. *Int J Heat Mass Transf* **2019**, *134*, 511–520. https://doi.org/10.1016/J.IJHEATMASSTRANSFER.2018.12.170.

(81) Hobold, G. M.; da Silva, A. K. Machine Learning Classification of Boiling Regimes with Low Speed, Direct and Indirect Visualization. *Int J Heat Mass Transf* **2018**, *125*, 1296–1309. https://doi.org/10.1016/J.IJHEATMASSTRANSFER.2018.04.156.

(82) Godlieb, W.; Deen, N. G.; Kuipers, J. A. M. Bubble Behaviour in Fluidised Beds at Elevated Pressures. *Macromol Mater Eng* **2011**, *296* (3–4), 270–277. https://doi.org/10.1002/MAME.201000323.

(83) Sadr-Kazemi, N.; Cilliers, J. J. An Image Processing Algorithm for Measurement of Flotation Froth Bubble Size and Shape Distributions. *Miner Eng* **1997**, *10* (10), 1075–1083. https://doi.org/10.1016/S0892-6875(97)00094-0.

(84) Chan, W. H. R.; Dodd, M. S.; Johnson, P. L.; Moin, P. Identifying and Tracking Bubbles and Drops in Simulations: A Toolbox for Obtaining Sizes, Lineages, and Breakup and Coalescence Statistics. *J Comput Phys* **2021**, *432*, 110156. https://doi.org/10.1016/J.JCP.2021.110156.

(85) Vogt, H. The Actual Current Density of Gas-Evolving Electrodes—Notes on the Bubble Coverage. *Electrochim Acta* **2012**, *78*, 183–187. https://doi.org/10.1016/J.ELECTACTA.2012.05.124.

(86) Dukovic, J.; Tobias, C. W. The Influence of Attached Bubbles on Potential Drop and Current Distribution at Gas-Evolving Electrodes. *J Electrochem Soc* **1987**, *134* (2), 331–343. https://doi.org/10.1149/1.2100456.

(87) Lake, J. R.; Soto, Á. M.; Varanasi, K. K. Impact of Bubbles on Electrochemically Active Surface Area of Microtextured Gas-Evolving Electrodes. *Langmuir* **2022**, *38* (10), 3276–3283. https://doi.org/10.1021/acs.langmuir.2c00035.

(88) Reza, A. M. Realization of the Contrast Limited Adaptive Histogram Equalization (CLAHE) for Real-Time Image Enhancement. *Journal of VLSI signal processing systems for signal, image and video technology 2004 38:1* **2004**, *38* (1), 35–44. https://doi.org/10.1023/B:VLSI.0000028532.53893.82.

(89) Pisano, E. D.; Zong, S.; Hemminger, B. M.; DeLuca, M.; Johnston, R. E.; Muller, K.; Braeuning, M. P.; Pizer, S. M. Contrast Limited Adaptive Histogram Equalization Image Processing to Improve the Detection of Simulated Spiculations in Dense Mammograms. *Journal of Digital Imaging 1998 11:4* **1998**, *11* (4), 193–200. https://doi.org/10.1007/BF03178082.

(90) He, K.; Gkioxari, G.; Dollár, P.; Girshick, R. Mask R-CNN.

(91) Sun, X.; Wu, P.; Hoi, S. C. H. Face Detection Using Deep Learning: An Improved Faster RCNN Approach. *Neurocomputing* **2018**, *299*, 42–50. https://doi.org/10.1016/J.NEUCOM.2018.03.030.

(92) Hung, J.; Carpenter, A. Applying Faster R-CNN for Object Detection on Malaria Images. *Proceedings of the IEEE Conference on Computer Vision and Pattern Recognition (CVPR) Workshops* **2017**, 56–61.

(93) Li, X.; Shang, M.; Qin, H.; Chen, L. Fast Accurate Fish Detection and Recognition of Underwater Images with Fast R-CNN. *OCEANS 2015 - MTS/IEEE Washington* **2016**. https://doi.org/10.23919/OCEANS.2015.7404464.

(94) Li, J.; Liang, X.; Shen, S.; Xu, T.; Feng, J.; Yan, S. Scale-Aware Fast R-CNN for Pedestrian Detection. *IEEE Trans Multimedia* **2018**, *20* (4), 985–996. https://doi.org/10.1109/TMM.2017.2759508.

(95) Li, Y.; Xie, S.; Chen, X.; Dollar, P.; He, K.; Girshick, R. Benchmarking Detection Transfer Learning with Vision Transformers. **2021**. https://doi.org/10.48550/arxiv.2111.11429.

(96) Lin, T. Y.; Maire, M.; Belongie, S.; Hays, J.; Perona, P.; Ramanan, D.; Dollár, P.; Zitnick, C. L. Microsoft COCO: Common Objects in Context. *Lecture Notes in Computer Science (including subseries Lecture Notes in Artificial Intelligence and Lecture Notes in Bioinformatics)* **2014**, *8693 LNCS* (PART 5), 740–755. https://doi.org/10.1007/978-3-319-10602-1_48/COVER.

(97) Yuen, H.; Princen, J.; Illingworth, J.; Kittler, J. Comparative Study of Hough Transform Methods for Circle Finding. *Image Vis Comput* **1990**, *8* (1), 71–77. https://doi.org/10.1016/0262-8856(90)90059-E.

(98) Li, L.; Jamieson, K.; Rostamizadeh, A.; Gonina, E.; Ben-tzur, J.; Hardt, M.; Recht, B.; Talwalkar, A. A System for Massively Parallel Hyperparameter Tuning. *Proceedings of Machine Learning and Systems* **2020**, *2*, 230–246.

(99) Moreno Soto, Á.; Maddalena, T.; Fraters, A.; van der Meer, D.; Lohse, D. Coalescence of Diffusively Growing Gas Bubbles. *J Fluid Mech* **2018**, *846*, 143–165. https://doi.org/10.1017/jfm.2018.277.

(100) Bockris, M.; Shamshul Huq, A. K. M. The Mechanism of the Electrolytic Evolution of Oxygen on Platinum. *Source: Proceedings of the Royal Society of London. Series A, Mathematical and Physical Sciences* **1956**, *237* (1209), 277–296.

(101) Yildirim, Ö.; Kiss, A. A.; Hüser, N.; Leßmann, K.; Kenig, E. Y. Reactive Absorption in Chemical Process Industry: A Review on Current Activities. *Chemical Engineering Journal* **2012**, *213*, 371–391. https://doi.org/10.1016/J.CEJ.2012.09.121.

(102) Chen, L.; Lin, J. W.; Yang, C. L. Absorption of NO2 in a Packed Tower with Na2SO3 Aqueous Solution. *Environmental Progress* **2002**, *21* (4), 225–230. https://doi.org/10.1002/EP.670210411.

(103) Lin, C.-C.; Liu, W.-T.; Tan, C.-S. Removal of Carbon Dioxide by Absorption in a Rotating Packed Bed. **2003**. https://doi.org/10.1021/IE020669.

(104) Spedding, P. L.; Munro, P. A.; Jones, M. T. Ammonia Absorption into Water in a Packed Tower I: Characterization of Packing and Liquid Distribution. *The Chemical Engineering Journal* **1986**, *32* (2), 65–76. https://doi.org/10.1016/0300-9467(86)80053-3.

(105) Zarzycki, R.; Chacuk, A. *Absorption: Fundamentals & Applications*; 2013.

(106) F Delvigne; JP Lecomte. *Encyclopedia on Industrial Biotechnology: Bioprocess, Bioseparation and Cell Technologies. Foam Formation and Control in Bioreactors*; Wiley: New York, NY, 2010.

(107) Chalmers, J. J.; Bavarian, F. Microscopic Visualization of Insect Cell-Bubble Interactions. II: The Bubble Film and Bubble Rupture. *Biotechnol Prog* **1991**, *7* (2), 151–158. https://doi.org/10.1021/BP00008A010.

(108) Cherry, R. S.; Hulle, C. T. Cell Death in the Thin Films of Bursting Bubbles. *Biotechnol Prog* **1992**, *8* (1), 11–18. https://doi.org/10.1021/BP00013A003.

(109) Betts, J. I.; Baganz, F. Miniature Bioreactors: Current Practices and Future Opportunities. *Microb Cell Fact* **2006**, *5* (1), 1–14. https://doi.org/10.1186/1475-2859-5-21/FIGURES/3.

(110) Gupta, P. L.; Lee, S. M.; Choi, H. J. A Mini Review: Photobioreactors for Large Scale Algal Cultivation. *World J Microbiol Biotechnol* **2015**, *31* (9), 1409–1417. https://doi.org/10.1007/S11274-015-1892-4/FIGURES/5.

(111) Langley, N. M.; Harrison, S. T. L.; van Hille, R. P. A Critical Evaluation of CO2 Supplementation to Algal Systems by Direct Injection. *Biochem Eng J* **2012**, *68*, 70–75. https://doi.org/10.1016/J.BEJ.2012.07.013.

(112) *Global Defoamers Market Size & Share Report, 2030*. https://www.grandviewresearch.com/industry-analysis/defoamers-market (accessed 2022-09-27).

(113) Deotale, S.; Dutta, S.; Moses, J. A.; Balasubramaniam, V. M.; Anandharamakrishnan, C. Foaming Characteristics of Beverages and Its Relevance to Food Processing. *Food Engineering Reviews* **2020**, *12* (2), 229–250. https://doi.org/10.1007/S12393-020-09213-4/FIGURES/10.

(114) Wang, L. K. Humanitarian Engineering Education of the Lenox Institute of Water Technology and Its New Potable Water Flotation Processes. **2021**, 1–72. https://doi.org/10.1007/978-3-030-54642-7_1.

(115) Li, P.; Wu, Q.; Wu, H.; Wen, S.; Wang, L.; Li, S. Flocculation-Air Flotation Treatment of Wastewater from Paper-Making Reconstituted Tobacco Sheet. *IOP Conf. Series: Earth and Environmental Science* **2018**, *170* (032082). https://doi.org/10.1088/1755-1315/170/3/032082.

(116) Lim, K.; Evans, P. J.; Parameswaran, P. Long-Term Performance of a Pilot-Scale Gas-Sparged Anaerobic Membrane Bioreactor under Ambient Temperatures for Holistic Wastewater Treatment. *Environ Sci Technol* **2019**, *53* (13), 7347–7354. https://doi.org/10.1021/ACS.EST.8B06198/ASSET/IMAGES/LARGE/ES-2018-061989_0004.JPEG.

(117) Vyrides, I.; Stuckey, D. C. Saline Sewage Treatment Using a Submerged Anaerobic Membrane Reactor (SAMBR): Effects of Activated Carbon Addition and Biogas-Sparging Time. *Water Res* **2009**, *43* (4), 933–942. https://doi.org/10.1016/J.WATRES.2008.11.054.

(118) Takemura, F.; Matsumoto, Y. Dissolution Rate of Spherical Carbon Dioxide Bubbles in Strong Alkaline Solutions. *Chem Eng Sci* **2000**, *55* (18), 3907–3917. https://doi.org/10.1016/S0009-2509(00)00022-1.

(119) Sherwood, T. K. *Absorption and Extraction*, 1st ed.; McGraw-Hill Book Co.: New York, NY, 1937.

(120) Sherwood, T. K.; Pigford, R. L.; Wilke, C. R. *Mass Transfer*; McGraw-Hill: New York, NY, 1975.

(121) Abanades, J. C.; Arias, B.; Lyngfelt, A.; Mattisson, T.; Wiley, D. E.; Li, H.; Ho, M. T.; Mangano, E.; Brandani, S. Emerging CO2 Capture Systems. *International Journal of Greenhouse Gas Control* **2015**, *40*, 126–166. https://doi.org/10.1016/J.IJGGC.2015.04.018.

(122) Keith, D. W.; Holmes, G.; st. Angelo, D.; Heidel, K. A Process for Capturing CO2 from the Atmosphere. *Joule* **2018**, *2* (8), 1573–1594. https://doi.org/10.1016/J.JOULE.2018.05.006.

(123) Bushuyev, O. S.; de Luna, P.; Dinh, C. T.; Tao, L.; Saur, G.; van de Lagemaat, J.; Kelley, S. O.; Sargent, E. H. What Should We Make with CO2 and How Can We Make It? *Joule* **2018**, *2* (5), 825–832. https://doi.org/10.1016/j.joule.2017.09.003.

(124) Rahman, F. A.; Aziz, M. M. A.; Saidur, R.; Bakar, W. A. W. A.; Hainin, M. R.; Putrajaya, R.; Hassan, N. A. Pollution to Solution: Capture and Sequestration of Carbon Dioxide (CO2) and Its Utilization as a Renewable Energy Source for a Sustainable Future. *Renewable and Sustainable Energy Reviews* **2017**, *71*, 112–126. https://doi.org/10.1016/J.RSER.2017.01.011.

(125) Yu, C. H.; Huang, C. H.; Tan, C. S. A Review of CO2 Capture by Absorption and Adsorption. *Aerosol Air Qual Res* **2012**, *12* (5), 745–769. https://doi.org/10.4209/AAQR.2012.05.0132.

(126) Diederichsen, K. M.; Sharifian, R.; Kang, J. S.; Liu, Y.; Kim, S.; Gallant, B. M.; Vermaas, D.; Hatton, T. A. Electrochemical Methods for Carbon Dioxide Separations. *Nature Reviews Methods Primers 2022 2:1* **2022**, *2* (1), 1–20. https://doi.org/10.1038/s43586-022-00148-0.

(127) Naraharisetti, P. K.; Yeo, T. Y.; Bu, J. New Classification of CO2 Mineralization Processes and Economic Evaluation. *Renewable and Sustainable Energy Reviews* **2019**, *99*, 220–233. https://doi.org/10.1016/J.RSER.2018.10.008.

(128) Geerlings, H.; Zevenhoven, R. CO2 Mineralization—Bridge Between Storage and Utilization of CO2. *http://dx.doi.org/10.1146/annurev-chembioeng-062011-080951* **2013**, *4*, 103–117. https://doi.org/10.1146/ANNUREV-CHEMBIOENG-062011-080951.

(129) Pan, S. Y.; Chen, Y. H.; Fan, L. S.; Kim, H.; Gao, X.; Ling, T. C.; Chiang, P. C.; Pei, S. L.; Gu, G. CO2 Mineralization and Utilization by Alkaline Solid Wastes for Potential Carbon Reduction. *Nature Sustainability 2020 3:5* **2020**, *3* (5), 399–405. https://doi.org/10.1038/s41893-020-0486-9.

(130) Xie, H.; Yue, H.; Zhu, J.; Liang, B.; Li, C.; Wang, Y.; Xie, L.; Zhou, X. Scientific and Engineering Progress in CO2 Mineralization Using Industrial Waste and Natural Minerals. *Engineering* **2015**, *1* (1), 150–157. https://doi.org/10.15302/J-ENG-2015017.

(131) la Plante, E. C.; Simonetti, D. A.; Wang, J.; Al-Turki, A.; Chen, X.; Jassby, D.; Sant, G. N. Saline Water-Based Mineralization Pathway for Gigatonne-Scale CO2 Management. *ACS Sustain Chem Eng* **2021**, *9* (3), 1073–1089. https://doi.org/10.1021/ACSSUSCHEMENG.0C08561/ASSET/IMAGES/LARGE/SC0C08561_0007.JPEG.

(132) Zhang, S.; DePaolo, D. J. Rates of CO2 Mineralization in Geological Carbon Storage. *Acc Chem Res* **2017**, *50* (9), 2075–2084. https://doi.org/10.1021/ACS.ACCOUNTS.7B00334/ASSET/IMAGES/AR-2017-00334D_M007.GIF.

(133) Rubino, J. G.; Velis, D. R.; Sacchi, M. D. Numerical Analysis of Wave-Induced Fluid Flow Effects on Seismic Data: Application to Monitoring of CO2 Storage at the Sleipner Field. *J Geophys Res Solid Earth* **2011**, *116* (B3), 3306. https://doi.org/10.1029/2010JB007997.

(134) Trias, R.; Ménez, B.; le Campion, P.; Zivanovic, Y.; Lecourt, L.; Lecoeuvre, A.; Schmitt-Kopplin, P.; Uhl, J.; Gislason, S. R.; Alfreosson, H. A.; Mesfin, K. G.; Snæbjörnsdóttir, S. O.; Aradóttir, E. S.; Gunnarsson, I.; Matter, J. M.; Stute, M.; Oelkers, E. H.; Gérard, E. High Reactivity of Deep Biota under Anthropogenic CO2 Injection into Basalt. *Nature Communications 2017 8:1* **2017**, *8* (1), 1–14. https://doi.org/10.1038/s41467-017-01288-8.

(135) Pogge von Strandmann, P. A. E.; Burton, K. W.; Snæbjörnsdóttir, S. O.; Sigfússon, B.; Aradóttir, E. S.; Gunnarsson, I.; Alfredsson, H. A.; Mesfin, K. G.; Oelkers, E. H.; Gislason, S. R. Rapid CO2 Mineralisation into Calcite at the CarbFix Storage Site Quantified Using Calcium Isotopes. *Nature Communications 2019 10:1* **2019**, *10* (1), 1–7. https://doi.org/10.1038/s41467-019-10003-8.

(136) Snæbjörnsdóttir, S.; Sigfússon, B.; Marieni, C.; Goldberg, D.; Gislason, S. R.; Oelkers, E. H. Carbon Dioxide Storage through Mineral Carbonation. *Nature Reviews Earth & Environment 2020 1:2* **2020**, *1* (2), 90–102. https://doi.org/10.1038/s43017-019-0011-8.

(137) Matter, J. M.; Stute, M.; Snæbjörnsdottir, S.; Oelkers, E. H.; Gislason, S. R.; Aradottir, E. S.; Sigfusson, B.; Gunnarsson, I.; Sigurdardottir, H.; Gunnlaugsson, E.; Axelsson, G.; Alfredsson, H. A.; Wolff-Boenisch, D.; Mesfin, K.; Taya, D. F. D. L. R.; Hall, J.; Dideriksen, K.; Broecker, W. S. Rapid Carbon Mineralization for Permanent Disposal of Anthropogenic Carbon Dioxide Emissions. *Science (1979)* **2016**, *352* (6291), 1312–1314.

https://doi.org/10.1126/SCIENCE.AAD8132/SUPPL_FILE/AAD8132-MATTER-SM.PDF.

(138) Shojai Kaveh, N.; Rudolph, E. S. J.; van Hemert, P.; Rossen, W. R.; Wolf, K. H. Wettability Evaluation of a CO2/Water/Bentheimer Sandstone System: Contact Angle, Dissolution, and Bubble Size. *Energy and Fuels* **2014**, *28* (6), 4002–4020. https://doi.org/10.1021/EF500034J/ASSET/IMAGES/EF-2014-00034J_M028.GIF.

(139) de Maleprade, H.; Clanet, C.; Quéré, D. Spreading of Bubbles after Contacting the Lower Side of an Aerophilic Slide Immersed in Water. *Phys Rev Lett* **2016**, *117* (9), 094501. https://doi.org/10.1103/PHYSREVLETT.117.094501/FIGURES/4/MEDIUM.

(140) Rapoport, L.; Emmerich, T.; Varanasi, K. K.; Rapoport, L.; Emmerich, T.; Varanasi, K. K. Capturing Bubbles and Preventing Foam Using Aerophilic Surfaces. *Adv Mater Interfaces* **2020**, *7* (6), 1901599. https://doi.org/10.1002/ADMI.201901599.

(141) Davis, H. S.; Crandall, G. S. The Role of the Liquid Stationary Film in Batch Absorptions of Gases. II. Absorptions Involving Irreversible Chemical Reactions. *The Liquid Stationary Film in Gas Absorptions* **1930**, *52*, 3769.

(142) Hitchcock, L. B. Rate of Absorption of Carbon Dioxide Effect of Concentration and Viscosity of Caustic Solutions. *Ind Eng Chem* **1934**, *25* (11), 1158–1167.

(143) Vassilatos, G.; Trass, O.; Johnson, A. I. Simultaneous Gas Absorption and Liquid Phase Chemical Reaction in an Agitated Vessel. *Can J Chem Eng* **1962**, *40* (5), 210–214. https://doi.org/10.1002/CJCE.5450400507.

(144) Schennetten, K.; Meier, M. M.; Scheibinger, M. Non-Sticking Drops. *Reports on Progress in Physics* **2005**, *68* (11), 2495. https://doi.org/10.1088/0034-4885/68/11/R01.

(145) NRG Energy Inc. *NRG Investor Presentation*. https://investors.nrg.com/static-files/5959d26c-3a5f-4fe6-9cdb-f7c07bf1d4b7 (accessed 2022-09-28).

(146) *Health Organization, W. UN Sustainable Development Summit 2015*. https://www.who.int/ mediacentre/events/meetings/2015/ un-sustainable-development-summit/ en/.

(147) Wilkinson, P.; Smith, K. R.; Davies, M.; Adair, H.; Armstrong, B. G.; Barrett, M.; Bruce, N.; Haines, A.; Hamilton, I.; Oreszczyn, T.; Ridley, I.; Tonne, C.; Chalabi, Z. Public Health Benefits of Strategies to Reduce Greenhouse-Gas Emissions: Household Energy. *The Lancet* **2009**, *374* (9705), 1917–1929. https://doi.org/10.1016/S0140-6736(09)61713-X.

(148) Friedlingstein, P.; Andrew, R. M.; Rogelj, J.; Peters, G. P.; Canadell, J. G.; Knutti, R.; Luderer, G.; Raupach, M. R.; Schaeffer, M.; van Vuuren, D. P.; le Quéré, C. Persistent Growth of CO2 Emissions and Implications for Reaching Climate Targets. *Nat Geosci* **2014**, *7* (10), 709–715. https://doi.org/10.1038/ngeo2248.

(149) Bouman, E. A.; Lindstad, E.; Rialland, A. I.; Strømman, A. H. State-of-the-Art Technologies, Measures, and Potential for Reducing GHG Emissions from Shipping – A Review. *Transp Res D Transp Environ* **2017**, *52* (A), 408–421. https://doi.org/10.1016/j.trd.2017.03.022.

(150) Steeneveldt, R.; Berger, B.; Torp, T. A. CO2 Capture and Storage. *Chemical Engineering Research and Design* **2006**, *84* (9), 739–763. https://doi.org/10.1205/cherd05049.

(151) Koytsoumpa, E. I.; Bergins, C.; Kakaras, E. The CO2 Economy: Review of CO2 Capture and Reuse Technologies. *J Supercrit Fluids* **2018**, *132* (SI), 3–16. https://doi.org/10.1016/j.supflu.2017.07.029.

(152) RAVEN, J. A.; FALKOWSKI, P. G. Oceanic Sinks for Atmospheric CO $_2$. *Plant Cell Environ* **1999**, *22* (6), 741–755. https://doi.org/10.1046/j.1365-3040.1999.00419.x.

(153) Doney, S. C.; Fabry, V. J.; Feely, R. A.; Kleypas, J. A. Ocean Acidification: The Other CO $_2$ Problem. *Ann Rev Mar Sci* **2009**, *1* (1), 169–192. https://doi.org/10.1146/annurev.marine.010908.163834.

(154) Turley, C.; Findlay, H. S. Chapter 18 - Ocean Acidification. In *Climate change: observed impacts on planet Earth*; Letcher, T. M., Ed.; Elsevier B.V., 2015; pp 271–293.

(155) Song, C. Global Challenges and Strategies for Control, Conversion and Utilization of CO2 for Sustainable Development Involving Energy, Catalysis, Adsorption and Chemical Processing. *Catal Today* **2006**, *115* (1–4), 2–32. https://doi.org/10.1016/j.cattod.2006.02.029.

(156) Kondratenko, E. v.; Mul, G.; Baltrusaitis, J.; Larrazábal, G. O.; Pérez-Ramírez, J. Status and Perspectives of CO2 Conversion into Fuels and Chemicals by Catalytic, Photocatalytic and Electrocatalytic Processes. *Energy Environ Sci* **2013**, *6* (11), 3112. https://doi.org/10.1039/c3ee41272e.

(157) Alper, E.; Yuksel Orhan, O. CO 2 Utilization: Developments in Conversion Processes. **2017**. https://doi.org/10.1016/j.petlm.2016.11.003.

(158) Thorson, M. R.; Siil, K. I.; Kenis, P. J. A. Effect of Cations on the Electrochemical Conversion of CO $_2$ to CO. *J Electrochem Soc* **2013**, *160* (1), F69–F74. https://doi.org/10.1149/2.052301jes.

(159) Zhu, W.; Zhang, Y.-J.; Zhang, H.; Lv, H.; Li, Q.; Michalsky, R.; Peterson, A. A.; Sun, S. Active and Selective Conversion of CO $_2$ to CO on Ultrathin Au Nanowires. *J Am Chem Soc* **2014**, *136* (46), 16132–16135. https://doi.org/10.1021/ja5095099.

(160) Ulmer, U.; Dingle, T.; Duchesne, P. N.; Morris, R. H.; Tavasoli, A.; Wood, T.; Ozin, G. A. Fundamentals and Applications of Photocatalytic CO2 Methanation. *Nat Commun* **2019**, *10* (1), 3169. https://doi.org/10.1038/s41467-019-10996-2.

(161) Arai, T.; Sato, S.; Morikawa, T. A Monolithic Device for CO_2 Photoreduction to Generate Liquid Organic Substances in a Single-Compartment Reactor. *Energy Environ Sci* **2015**, *8* (7), 1998–2002. https://doi.org/10.1039/C5EE01314C.

(162) Bai, S.; Shao, Q.; Wang, P.; Dai, Q.; Wang, X.; Huang, X. Highly Active and Selective Hydrogenation of CO_2 to Ethanol by Ordered Pd–Cu Nanoparticles. *J Am Chem Soc* **2017**, *139* (20), 6827–6830. https://doi.org/10.1021/jacs.7b03101.

(163) Kim, D.; Kley, C. S.; Li, Y.; Yang, P. Copper Nanoparticle Ensembles for Selective Electroreduction of CO_2 to C_2–C_3 Products. *Proceedings of the National Academy of Sciences* **2017**, *114* (40), 10560–10565. https://doi.org/10.1073/pnas.1711493114.

(164) Kuhl, K. P.; Cave, E. R.; Abram, D. N.; Jaramillo, T. F. New Insights into the Electrochemical Reduction of Carbon Dioxide on Metallic Copper Surfaces. *Energy Environ Sci* **2012**, *5* (5), 7050. https://doi.org/10.1039/c2ee21234j.

(165) Ullmann, F. *Ullmann's Encyclopedia of Industrial Chemistry*, 7th ed.; Wiley-VCH Verlag GmbH& Co., 2000.

(166) Qiao, J.; Liu, Y.; Hong, F.; Zhang, J. A Review of Catalysts for the Electroreduction of Carbon Dioxide to Produce Low-Carbon Fuels. *Chem. Soc. Rev.* **2014**, *43* (2), 631–675. https://doi.org/10.1039/C3CS60323G.

(167) Todoroki, M.; Hara, K.; Kudo, A.; Sakata, T. Electrochemical Reduction of High Pressure CO2 at Pb, Hg and In Electrodes in an Aqueous KHCO3 Solution. *Journal of Electroanalytical Chemistry* **1995**, *394* (1–2), 199–203. https://doi.org/10.1016/0022-0728(95)04010-L.

(168) Lee, C. H.; Kanan, M. W. Controlling H^+ vs CO_2 Reduction Selectivity on Pb Electrodes. *ACS Catal* **2015**, *5* (1), 465–469. https://doi.org/10.1021/cs5017672.

(169) Pander, J. E.; Baruch, M. F.; Bocarsly, A. B. Probing the Mechanism of Aqueous CO_2 Reduction on Post-Transition-Metal Electrodes Using ATR-IR Spectroelectrochemistry. *ACS Catal* **2016**, *6* (11), 7824–7833. https://doi.org/10.1021/acscatal.6b01879.

(170) Paik, W.; Andersen, T. N.; Eyring, H. Kinetic Studies of the Electrolytic Reduction of Carbon Dioxide on the Mercury Electrode. *Electrochim Acta* **1969**, *14* (12), 1217–1232. https://doi.org/10.1016/0013-4686(69)87019-2.

(171) Wang, Q.; Dong, H.; Yu, H.; Yu, H. Enhanced Performance of Gas Diffusion Electrode for Electrochemical Reduction of Carbon Dioxide to Formate by Adding

Polytetrafluoroethylene into Catalyst Layer. *J Power Sources* **2015**, *279*, 1–5. https://doi.org/10.1016/j.jpowsour.2014.12.118.

(172) Chen, Y.; Li, C. W.; Kanan, M. W. Aqueous CO 2 Reduction at Very Low Overpotential on Oxide-Derived Au Nanoparticles. *J Am Chem Soc* **2012**, *134* (49), 19969–19972. https://doi.org/10.1021/ja309317u.

(173) Zhu, W.; Michalsky, R.; Metin, Ö.; Lv, H.; Guo, S.; Wright, C. J.; Sun, X.; Peterson, A. A.; Sun, S. Monodisperse Au Nanoparticles for Selective Electrocatalytic Reduction of CO 2 to CO. *J Am Chem Soc* **2013**, *135* (45), 16833–16836. https://doi.org/10.1021/ja409445p.

(174) Singh, M. R.; Kwon, Y.; Lum, Y.; Ager, J. W.; Bell, A. T. Hydrolysis of Electrolyte Cations Enhances the Electrochemical Reduction of CO 2 over Ag and Cu. *J Am Chem Soc* **2016**, *138* (39), 13006–13012. https://doi.org/10.1021/jacs.6b07612.

(175) Ham, Y. S.; Choe, S.; Kim, M. J.; Lim, T.; Kim, S.-K.; Kim, J. J. Electrodeposited Ag Catalysts for the Electrochemical Reduction of CO 2 to CO. *Appl Catal B* **2017**, *208*, 35–43. https://doi.org/10.1016/j.apcatb.2017.02.040.

(176) Rosen, J.; Hutchings, G. S.; Lu, Q.; Forest, R. v.; Moore, A.; Jiao, F. Electrodeposited Zn Dendrites with Enhanced CO Selectivity for Electrocatalytic CO 2 Reduction. *ACS Catal* **2015**, *5* (8), 4586–4591. https://doi.org/10.1021/acscatal.5b00922.

(177) Zhang, T.; Li, X.; Qiu, Y.; Su, P.; Xu, W.; Zhong, H.; Zhang, H. Multilayered Zn Nanosheets as an Electrocatalyst for Efficient Electrochemical Reduction of CO2. *J Catal* **2018**, *357*, 154–162. https://doi.org/10.1016/j.jcat.2017.11.003.

(178) Hori, Y.; Murata, A.; Takahashi, R. Formation of Hydrocarbons in the Electrochemical Reduction of Carbon Dioxide at a Copper Electrode in Aqueous Solution. *Journal of the Chemical Society, Faraday Transactions 1: Physical Chemistry in Condensed Phases* **1989**, *85* (8), 2309. https://doi.org/10.1039/f19898502309.

(179) Nitopi, S.; Bertheussen, E.; Scott, S. B.; Liu, X.; Engstfeld, A. K.; Horch, S.; Seger, B.; Stephens, I. E. L.; Chan, K.; Hahn, C.; Nørskov, J. K.; Jaramillo, T. F.; Chorkendorff, I. Progress and Perspectives of Electrochemical CO 2 Reduction on Copper in Aqueous Electrolyte. *Chem Rev* **2019**, *119* (12), 7610–7672. https://doi.org/10.1021/acs.chemrev.8b00705.

(180) Hori, Y.; Konishi, H.; Futamura, T.; Murata, A.; Koga, O.; Sakurai, H.; Oguma, K. "Deactivation of Copper Electrode" in Electrochemical Reduction of CO2. *Electrochim Acta* **2005**, *50* (27), 5354–5369. https://doi.org/10.1016/j.electacta.2005.03.015.

(181) Shi, C.; O'Grady, C. P.; Peterson, A. A.; Hansen, H. A.; Nørskov, J. K. Modeling CO2 Reduction on Pt(111). *Physical Chemistry Chemical Physics* **2013**, *15* (19), 7114. https://doi.org/10.1039/c3cp50645b.

(182) Wang, D.; Huang, R.; Liu, W.; Sun, D.; Li, Z. Fe-Based MOFs for Photocatalytic CO_2 Reduction: Role of Coordination Unsaturated Sites and Dual Excitation Pathways. *ACS Catal* **2014**, *4* (12), 4254–4260. https://doi.org/10.1021/cs501169t.

(183) Ooka, H.; Figueiredo, M. C.; Koper, M. T. M. Competition between Hydrogen Evolution and Carbon Dioxide Reduction on Copper Electrodes in Mildly Acidic Media. *Langmuir* **2017**, *33* (37), 9307–9313. https://doi.org/10.1021/acs.langmuir.7b00696.

(184) Dunwell, M.; Yang, X.; Setzler, B. P.; Anibal, J.; Yan, Y.; Xu, B. Examination of Near-Electrode Concentration Gradients and Kinetic Impacts on the Electrochemical Reduction of CO_2 Using Surface-Enhanced Infrared Spectroscopy. *ACS Catal* **2018**, *8* (5), 3999–4008. https://doi.org/10.1021/acscatal.8b01032.

(185) Liu, X.; Schlexer, P.; Xiao, J.; Ji, Y.; Wang, L.; Sandberg, R. B.; Tang, M.; Brown, K. S.; Peng, H.; Ringe, S.; Hahn, C.; Jaramillo, T. F.; Nørskov, J. K.; Chan, K. PH Effects on the Electrochemical Reduction of CO(2) towards C2 Products on Stepped Copper. *Nat Commun* **2019**, *10* (1), 32. https://doi.org/10.1038/s41467-018-07970-9.

(186) Rozanski, K.; Froehlich, K.; Mook, W. G. Environmental Isotopes in the Hydrological Cycle: Principles and Applications. *Technical Documents in Hydrology* **2001**, *1* (39).

(187) Kuhn, A. T.; Chan, C. Y. PH Changes at Near-Electrode Surfaces. *J Appl Electrochem* **1983**, *13* (2), 189–207. https://doi.org/10.1007/BF00612481.

(188) Schouten, K. J. P.; Pérez Gallent, E.; Koper, M. T. M. The Influence of PH on the Reduction of CO and <math Altimg="si29.Gif" Overflow="scroll"> <mrow> <msub> <mrow> <mtext>CO</Mtext> </Mrow> <mrow> <mn>2</Mn> </Mrow> </Msub> </Mrow> </Math> to Hydrocarbons on Copper Electrodes. *Journal of Electroanalytical Chemistry* **2014**, *716* (SI), 53–57. https://doi.org/10.1016/j.jelechem.2013.08.033.

(189) Bumroongsakulsawat, P.; Kelsall, G. H. Effect of Solution PH on CO: Formate Formation Rates during Electrochemical Reduction of Aqueous CO2 at Sn Cathodes. *Electrochim Acta* **2014**, *141*, 216–225. https://doi.org/10.1016/j.electacta.2014.07.057.

(190) de Luna, P.; Quintero-Bermudez, R.; Dinh, C.-T.; Ross, M. B.; Bushuyev, O. S.; Todorović, P.; Regier, T.; Kelley, S. O.; Yang, P.; Sargent, E. H. Catalyst Electro-Redeposition Controls Morphology and Oxidation State for Selective Carbon Dioxide Reduction. *Nat Catal* **2018**, *1* (2), 103–110. https://doi.org/10.1038/s41929-017-0018-9.

(191) Lu, Q.; Rosen, J.; Zhou, Y.; Hutchings, G. S.; Kimmel, Y. C.; Chen, J. G.; Jiao, F. A Selective and Efficient Electrocatalyst for Carbon Dioxide Reduction. *Nat Commun* **2014**, *5* (1), 3242. https://doi.org/10.1038/ncomms4242.

(192) Kim, C.; Jeon, H. S.; Eom, T.; Jee, M. S.; Kim, H.; Friend, C. M.; Min, B. K.; Hwang, Y. J. Achieving Selective and Efficient Electrocatalytic Activity for CO_2 Reduction Using

Immobilized Silver Nanoparticles. *J Am Chem Soc* **2015**, *137* (43), 13844–13850. https://doi.org/10.1021/jacs.5b06568.

(193) Liu, S.; Tao, H.; Zeng, L.; Liu, Q.; Xu, Z.; Liu, Q.; Luo, J.-L. Shape-Dependent Electrocatalytic Reduction of CO_2 to CO on Triangular Silver Nanoplates. *J Am Chem Soc* **2017**, *139* (6), 2160–2163. https://doi.org/10.1021/jacs.6b12103.

(194) Liu, M.; Pang, Y.; Zhang, B.; de Luna, P.; Voznyy, O.; Xu, J.; Zheng, X.; Dinh, C. T.; Fan, F.; Cao, C.; de Arquer, F. P. G.; Safaei, T. S.; Mepham, A.; Klinkova, A.; Kumacheva, E.; Filleter, T.; Sinton, D.; Kelley, S. O.; Sargent, E. H. Enhanced Electrocatalytic CO2 Reduction via Field-Induced Reagent Concentration. *Nature* **2016**, *537* (7620), 382–386. https://doi.org/10.1038/nature19060.

(195) Burdyny, T.; Graham, P. J.; Pang, Y.; Dinh, C.-T.; Liu, M.; Sargent, E. H.; Sinton, D. Nanomorphology-Enhanced Gas-Evolution Intensifies CO_2 Reduction Electrochemistry. *ACS Sustain Chem Eng* **2017**, *5* (5), 4031–4040. https://doi.org/10.1021/acssuschemeng.7b00023.

(196) Higgins, D.; Hahn, C.; Xiang, C.; Jaramillo, T. F.; Weber, A. Z. Gas-Diffusion Electrodes for Carbon Dioxide Reduction: A New Paradigm. *ACS Energy Lett* **2019**, *4* (1), 317–324. https://doi.org/10.1021/acsenergylett.8b02035.

(197) König, M.; Vaes, J.; Klemm, E.; Pant, D. Solvents and Supporting Electrolytes in the Electrocatalytic Reduction of CO2. *iScience* **2019**, *19*, 135–160. https://doi.org/10.1016/j.isci.2019.07.014.

(198) Zhang, J.; Luo, W.; Züttel, A. Self-Supported Copper-Based Gas Diffusion Electrodes for CO_2 Electrochemical Reduction. *J Mater Chem A Mater* **2019**, *7* (46), 26285–26292. https://doi.org/10.1039/C9TA06736A.

(199) Luo, W.; Zhang, J.; Li, M.; Züttel, A. Boosting CO Production in Electrocatalytic CO_2 Reduction on Highly Porous Zn Catalysts. *ACS Catal* **2019**, *9* (5), 3783–3791. https://doi.org/10.1021/acscatal.8b05109.

(200) García de Arquer, F. P.; Dinh, C. T.; Ozden, A.; Wicks, J.; McCallum, C.; Kirmani, A. R.; Nam, D. H.; Gabardo, C.; Seifitokaldani, A.; Wang, X.; Li, Y. C.; Li, F.; Edwards, J.; Richter, L. J.; Thorpe, S. J.; Sinton, D.; Sargent, E. H. CO2 Electrolysis to Multicarbon Products at Activities Greater than 1 A Cm−2. *Science (1979)* **2020**, *367* (6478), 661–666. https://doi.org/10.1126/SCIENCE.AAY4217/SUPPL_FILE/AAY4217_GARCIADEARQUER_SM.PDF.

(201) Tan, Y. C.; Lee, K. B.; Song, H.; Oh, J. Modulating Local CO2 Concentration as a General Strategy for Enhancing C−C Coupling in CO2 Electroreduction. *Joule* **2020**, *4* (5), 1104–1120. https://doi.org/10.1016/j.joule.2020.03.013.

(202) Gabardo, C. M.; O'Brien, C. P.; Edwards, J. P.; McCallum, C.; Xu, Y.; Dinh, C.-T.; Li, J.; Sargent, E. H.; Sinton, D. Continuous Carbon Dioxide Electroreduction to Concentrated Multi-Carbon Products Using a Membrane Electrode Assembly. *Joule* **2019**, *3* (11), 2777–2791. https://doi.org/10.1016/j.joule.2019.07.021.

(203) Wang, Y.; Hu, X.; Cao, Z.; Guo, L. Investigations on Bubble Growth Mechanism during Photoelectrochemical and Electrochemical Conversions. *Colloids Surf A Physicochem Eng Asp* **2016**, *505*, 86–92. https://doi.org/10.1016/j.colsurfa.2016.01.004.

(204) Burdyny, T.; Smith, W. A. CO_2 Reduction on Gas-Diffusion Electrodes and Why Catalytic Performance Must Be Assessed at Commercially-Relevant Conditions. *Energy Environ Sci* **2019**, *12* (5), 1442–1453. https://doi.org/10.1039/C8EE03134G.

(205) Chen, C. S.; Handoko, A. D.; Wan, J. H.; Ma, L.; Ren, D.; Yeo, B. S. Stable and Selective Electrochemical Reduction of Carbon Dioxide to Ethylene on Copper Mesocrystals. *Catal Sci Technol* **2015**, *5* (1), 161–168. https://doi.org/10.1039/C4CY00906A.

(206) Kas, R.; Kortlever, R.; Milbrat, A.; Koper, M. T. M.; Mul, G.; Baltrusaitis, J. Electrochemical CO_2 Reduction on Cu_2O-Derived Copper Nanoparticles: Controlling the Catalytic Selectivity of Hydrocarbons. *Phys. Chem. Chem. Phys.* **2014**, *16* (24), 12194–12201. https://doi.org/10.1039/C4CP01520G.

(207) Raciti, D.; Livi, K. J.; Wang, C. Highly Dense Cu Nanowires for Low-Overpotential CO_2 Reduction. *Nano Lett* **2015**, *15* (10), 6829–6835. https://doi.org/10.1021/acs.nanolett.5b03298.

(208) Ren, D.; Deng, Y.; Handoko, A. D.; Chen, C. S.; Malkhandi, S.; Yeo, B. S. Selective Electrochemical Reduction of Carbon Dioxide to Ethylene and Ethanol on Copper(I) Oxide Catalysts. *ACS Catal* **2015**, *5* (5), 2814–2821. https://doi.org/10.1021/cs502128q.

(209) Handoko, A. D.; Ong, C. W.; Huang, Y.; Lee, Z. G.; Lin, L.; Panetti, G. B.; Yeo, B. S. Mechanistic Insights into the Selective Electroreduction of Carbon Dioxide to Ethylene on Cu_2O-Derived Copper Catalysts. *The Journal of Physical Chemistry C* **2016**, *120* (36), 20058–20067. https://doi.org/10.1021/acs.jpcc.6b07128.

(210) Ma, M.; Djanashvili, K.; Smith, W. A. Controllable Hydrocarbon Formation from the Electrochemical Reduction of CO_2 over Cu Nanowire Arrays. *Angewandte Chemie International Edition* **2016**, *55* (23), 6680–6684. https://doi.org/10.1002/anie.201601282.

(211) Han, Z.; Kortlever, R.; Chen, H.-Y.; Peters, J. C.; Agapie, T. CO_2 Reduction Selective for $C_{\geq 2}$ Products on Polycrystalline Copper with N-Substituted Pyridinium Additives. *ACS Cent Sci* **2017**, *3* (8), 853–859. https://doi.org/10.1021/acscentsci.7b00180.

(212) Dinh, C. T.; Burdyny, T.; Kibria, G.; Seifitokaldani, A.; Gabardo, C. M.; Pelayo García De Arquer, F.; Kiani, A.; Edwards, J. P.; de Luna, P.; Bushuyev, O. S.; Zou, C.; Quintero-

Bermudez, R.; Pang, Y.; Sinton, D.; Sargent, E. H. CO2 Electroreduction to Ethylene via Hydroxide-Mediated Copper Catalysis at an Abrupt Interface. *Science (1979)* **2018**, *360* (6390), 783–787. https://doi.org/10.1126/SCIENCE.AAS9100/SUPPL_FILE/AAS9100-DINH-SM.PDF.

(213) Wang, Y.; Shen, H.; Livi, K. J. T.; Raciti, D.; Zong, H.; Gregg, J.; Onadeko, M.; Wan, Y.; Watson, A.; Wang, C. Copper Nanocubes for CO_2 Reduction in Gas Diffusion Electrodes. *Nano Lett* **2019**, *19* (12), 8461–8468. https://doi.org/10.1021/acs.nanolett.9b02748.

(214) Hori, Y.; Wakebe, H.; Tsukamoto, T.; Koga, O. Electrocatalytic Process of CO Selectivity in Electrochemical Reduction of CO2 at Metal Electrodes in Aqueous Media. *Electrochim Acta* **1994**, *39* (11–12), 1833–1839. https://doi.org/10.1016/0013-4686(94)85172-7.

(215) Shiratsuchi, R.; Nogami, G. Pulsed Electroreduction of CO_2 on Silver Electrodes. *J Electrochem Soc* **1996**, *143* (2), 582–586. https://doi.org/10.1149/1.1836484.

(216) Yano, H.; Shirai, F.; Nakayama, M.; Ogura, K. Electrochemical Reduction of CO2 at Three-Phase (Gas|liquid|solid) and Two-Phase (Liquid|solid) Interfaces on Ag Electrodes. *Journal of Electroanalytical Chemistry* **2002**, *533* (1–2), 113–118. https://doi.org/10.1016/S0022-0728(02)01078-1.

(217) Dufek, E. J.; Lister, T. E.; Stone, S. G.; McIlwain, M. E. Operation of a Pressurized System for Continuous Reduction of CO_2. *J Electrochem Soc* **2012**, *159* (9), F514–F517. https://doi.org/10.1149/2.011209jes.

(218) Kim, B.; Ma, S.; Molly Jhong, H.-R.; Kenis, P. J. A. Influence of Dilute Feed and PH on Electrochemical Reduction of CO2 to CO on Ag in a Continuous Flow Electrolyzer. *Electrochim Acta* **2015**, *166*, 271–276. https://doi.org/10.1016/j.electacta.2015.03.064.

(219) Endrődi, B.; Bencsik, G.; Darvas, F.; Jones, R.; Rajeshwar, K.; Janáky, C. Continuous-Flow Electroreduction of Carbon Dioxide. *Prog Energy Combust Sci* **2017**, *62*, 133–154. https://doi.org/10.1016/j.pecs.2017.05.005.

(220) Mariano, R. G.; McKelvey, K.; White, H. S.; Kanan, M. W. Selective Increase in CO_2 Electroreduction Activity at Grain-Boundary Surface Terminations. *Science (1979)* **2017**, *358* (6367), 1187–1192. https://doi.org/10.1126/science.aao3691.

(221) Verma, S.; Hamasaki, Y.; Kim, C.; Huang, W.; Lu, S.; Jhong, H.-R. M.; Gewirth, A. A.; Fujigaya, T.; Nakashima, N.; Kenis, P. J. A. Insights into the Low Overpotential Electroreduction of CO_2 to CO on a Supported Gold Catalyst in an Alkaline Flow Electrolyzer. *ACS Energy Lett* **2018**, *3* (1), 193–198. https://doi.org/10.1021/acsenergylett.7b01096.

(222) *Handbook of Reference Electrodes*; Inzelt, G., Lewenstem, A., Scholtz, F., Eds.; Springer: Berlin, 2013.

(223) Smith, T. J.; Stevenson, K. J. Reference Electrodes. In *Handbook of Electrochemistry*; Zoski, C. G., Ed.; Elsevier: SARA BURGERHARTSTRAAT 25, PO BOX 211, 1000 AE AMSTERDAM, NETHERLANDS, 2007; pp 73–110. https://doi.org/10.1016/B978-044451958-0.50005-7.

(224) Wang, L.; Lee, C.-Y.; Schmuki, P. Solar Water Splitting: Preserving the Beneficial Small Feature Size in Porous α-Fe $_2$ O $_3$ Photoelectrodes during Annealing. *J. Mater. Chem. A* **2013**, *1* (2), 212–215. https://doi.org/10.1039/C2TA00431C.

(225) Weisenberger, S.; Schumpe, A. Estimation of Gas Solubilities in Salt Solutions at Temperatures from 273 K to 363 K. *AIChE Journal* **1996**, *42* (1), 298–300. https://doi.org/10.1002/aic.690420130.

(226) Faraday, M. I. Experimental Researches in Electricity. *Philos. Trans. R. Soc.* **1834**, *124*, 77–122.

(227) Romero Cuellar, N. S.; Scherer, C.; Kaçkar, B.; Eisenreich, W.; Huber, C.; Wiesner-Fleischer, K.; Fleischer, M.; Hinrichsen, O. Two-Step Electrochemical Reduction of CO2 towards Multi-Carbon Products at High Current Densities. *Journal of CO2 Utilization* **2020**, *36*, 263–275. https://doi.org/10.1016/j.jcou.2019.10.016.

(228) Bejan, A. *Heat Transfer*, 1st ed.; John Wiley & Sons Inc, 1993.

(229) Henry, W. Experiments on the Quantity of Gases Absorbed by Water, at Different Temperatures, and under Different Pressures. *Philos. Trans. R. Soc. London* **1803**, *93*, 29–42.

(230) Peñas, P.; van der Linde, P.; Vijselaar, W.; van der Meer, D.; Lohse, D.; Huskens, J.; Gardeniers, H.; Modestino, M. A.; Rivas, D. F. Decoupling Gas Evolution from Water-Splitting Electrodes. *J Electrochem Soc* **2019**, *166* (15), H769–H776. https://doi.org/10.1149/2.1381914jes.

(231) Harned, H. S.; Davis, R. The Ionization Constant of Carbonic Acid in Water and the Solubility of Carbon Dioxide in Water and Aqueous Salt Solutions from 0 to 50°. *J Am Chem Soc* **1943**, *65* (10), 2030–2037. https://doi.org/10.1021/ja01250a059.

(232) Dickson, A. G.; Millero, F. J. A Comparison of the Equilibrium Constants for the Dissociation of Carbonic Acid in Seawater Media. *Deep Sea Research Part A. Oceanographic Research Papers* **1987**, *34* (10), 1733–1743. https://doi.org/10.1016/0198-0149(87)90021-5.

(233) Millero, F. J.; Roy, R. N. A Chemical Equilibrium Model for the Carbonate System in Natural Waters. *CROATICA CHEMICA ACTA* **1997**, *70* (1), 1–38.

(234) Harned, H. S.; Scholes, S. R. The Ionization Constant of HCO3- from 0 to 50°. *J Am Chem Soc* **1941**, *63* (6), 1706–1709. https://doi.org/10.1021/JA01851A058/ASSET/JA01851A058.FP.PNG_V03.

(235) Moreno Soto, Á.; Prosperetti, A.; Lohse, D.; van der Meer, D. Gas Depletion through Single Gas Bubble Diffusive Growth and Its Effect on Subsequent Bubbles. *J Fluid Mech* **2017**, *831*, 474–490. https://doi.org/10.1017/jfm.2017.623.

(236) Soto, Á. M.; Lohse, D.; van der Meer, D. Diffusive Growth of Successive Bubbles in Confinement. *J Fluid Mech* **2020**, *882*, A6. https://doi.org/10.1017/JFM.2019.806.

(237) Wilke, C. R.; Chang, P. Correlation of Diffusion Coefficients in Dilute Solutions. *AIChE Journal* **1955**, *1* (2), 264–270. https://doi.org/10.1002/aic.690010222.

(238) Frank, M. J. W.; Kuipers, J. A. M.; van Swaaij, W. P. M. Diffusion Coefficients and Viscosities of $CO_2 + H_2O$, $CO_2 + CH_3OH$, $NH_3 + H_2O$, and $NH_3 + CH_3OH$ Liquid Mixtures. *J Chem Eng Data* **1996**, *41* (2), 297–302. https://doi.org/10.1021/je950157k.

(239) Liger-Belair, G.; Prost, E.; Parmentier, M.; Jeandet, P.; Nuzillard, J.-M. Diffusion Coefficient of CO_2 Molecules as Determined by ^{13}C NMR in Various Carbonated Beverages. *J Agric Food Chem* **2003**, *51* (26), 7560–7563. https://doi.org/10.1021/jf034693p.

(240) GILLIAM, R.; GRAYDON, J.; KIRK, D.; THORPE, S. A Review of Specific Conductivities of Potassium Hydroxide Solutions for Various Concentrations and Temperatures. *Int J Hydrogen Energy* **2007**, *32* (3), 359–364. https://doi.org/10.1016/j.ijhydene.2006.10.062.

(241) Ellison, W.; Balana, A.; Delbos, G.; Lamkaouchi, K.; Eymard L and Guillou, C.; Prigent, C. New Permittivity Measurements of Seawater. *Radio Sci* **1998**, *33* (3), 639–648. https://doi.org/10.1029/97RS02223.

(242) Popov, I.; Ishai, P. ben; Khamzin, A.; Feldman, Y. The Mechanism of the Dielectric Relaxation in Water. *Physical Chemistry Chemical Physics* **2016**, *18* (20), 13941–13953. https://doi.org/10.1039/C6CP02195F.

(243) Khan, S.; Hwang, J.; Horn, Y.-S.; Varanasi, K. K. Catalyst-Proximal Plastrons Enhance Activity and Selectivity of Carbon Dioxide Electroreduction. *Cell Rep Phys Sci* **2021**, *2* (2), 100318. https://doi.org/10.1016/j.xcrp.2020.100318.

(244) Shiratsuchi, R.; Aikoh, Y.; Nogami, G. Pulsed Electroreduction of CO_2 on Copper Electrodes. *J Electrochem Soc* **1993**, *140* (12), 3479–3482. https://doi.org/10.1149/1.2221113.

(245) Nogami, G.; Itagaki, H.; Shiratsuchi, R. Pulsed Electroreduction of CO_2 on Copper Electrodes- II. *J Electrochem Soc* **1994**, *141* (5), 1138–1142. https://doi.org/10.1149/1.2054886.

(246) Biegler, T.; Rand, D. A. J.; Woods, R. Limiting Oxygen Coverage on Platinized Platinum; Relevance to Determination of Real Platinum Area by Hydrogen Adsorption. *J Electroanal Chem Interfacial Electrochem* **1971**, *29* (2), 269–277. https://doi.org/10.1016/S0022-0728(71)80089-X.

(247) Brummer, S. B. The Use of Large Anodic Galvanostatic Transients to Evaluate the Maximum Adsorption on Platinum from Formic Acid Solutions. *Journal of Physical Chemistry* **2002**, *69* (2), 562–571. https://doi.org/10.1021/J100886A034.

(248) Dhillon, N. S.; Buongiorno, J.; Varanasi, K. K. Critical Heat Flux Maxima during Boiling Crisis on Textured Surfaces. *Nature Communications 2015 6:1* **2015**, *6* (1), 1–12. https://doi.org/10.1038/ncomms9247.

(249) *V7 Labs*. https://www.v7labs.com/.

(250) Illingworth, J.; Kittler, J. The Adaptive Hough Transform. *IEEE Trans Pattern Anal Mach Intell* **1987**, *PAMI-9* (5), 690–698. https://doi.org/10.1109/TPAMI.1987.4767964.

(251) Ren, S.; He, K.; Girshick, R.; Sun, J. Faster R-CNN: Towards Real-Time Object Detection with Region Proposal Networks. *Adv Neural Inf Process Syst* **2015**, *28*.

(252) He, K.; Gkioxari, G.; Dollár, P.; Girshick, R. Mask R-CNN. *Proceedings of the IEEE international conference on computer vision*, **2017**, 2961–2969.

(253) Schindelin, J.; Arganda-Carreras, I.; Frise, E.; Kaynig, V.; Longair, M.; Pietzsch, T.; Preibisch, S.; Rueden, C.; Saalfeld, S.; Schmid, B.; Tinevez, J. Y.; White, D. J.; Hartenstein, V.; Eliceiri, K.; Tomancak, P.; Cardona, A. Fiji: An Open-Source Platform for Biological-Image Analysis. *Nature Methods 2012 9:7* **2012**, *9* (7), 676–682. https://doi.org/10.1038/nmeth.2019.

(254) Silva, R. F.; de Francesco, M.; Pozio, A. Solution-Cast Nafion® Ionomer Membranes: Preparation and Characterization. *Electrochim Acta* **2004**, *49* (19), 3211–3219. https://doi.org/10.1016/J.ELECTACTA.2004.02.035.

(255) Cho, K. Y.; Jung, H. Y.; Sung, K. A.; Kim, W. K.; Sung, S. J.; Park, J. K.; Choi, J. H.; Sung, Y. E. Preparation and Charateristics of Nafion Membrane Coated with a PVdF Copolymer/Recast Nafion Blend for Direct Methanol Fuel Cell. *J Power Sources* **2006**, *159* (1), 524–528. https://doi.org/10.1016/J.JPOWSOUR.2005.10.106.

(256) Luo, Q.; Zhang, H.; Chen, J.; You, D.; Sun, C.; Zhang, Y. Preparation and Characterization of Nafion/SPEEK Layered Composite Membrane and Its Application in Vanadium Redox

Flow Battery. *J Memb Sci* **2008**, *325* (2), 553–558. https://doi.org/10.1016/J.MEMSCI.2008.08.025.

(257) Gloukhovski, R.; Freger, V.; Tsur, Y. Understanding Methods of Preparation and Characterization of Pore-Filling Polymer Composites for Proton Exchange Membranes: A Beginner's Guide. *Reviews in Chemical Engineering* **2018**, *34* (4), 455–479. https://doi.org/10.1515/REVCE-2016-0065/ASSET/GRAPHIC/J_REVCE-2016-0065_FIG_004.JPG.

(258) Alipour Moghaddam, J.; Parnian, M. J.; Rowshanzamir, S. Preparation, Characterization, and Electrochemical Properties Investigation of Recycled Proton Exchange Membrane for Fuel Cell Applications. *Energy* **2018**, *161*, 699–709. https://doi.org/10.1016/J.ENERGY.2018.07.123.

(259) Lum, Y.; Yue, B.; Lobaccaro, P.; Bell, A. T.; Ager, J. W. Optimizing C-C Coupling on Oxide-Derived Copper Catalysts for Electrochemical CO2 Reduction. *Journal of Physical Chemistry C* **2017**, *121* (26), 14191–14203. https://doi.org/10.1021/ACS.JPCC.7B03673/ASSET/IMAGES/LARGE/JP-2017-03673M_0006.JPEG.

(260) PIRCHER, E.; RUIZ MARTINEZ, M.; HANSAL, S.; HANSAL, W. Electropolishing of Copper Alloys in Phosphoric Acid Solutions with Alcohols. *Plating and surface finishing* **2003**, *90* (5), 74–79.

(261) Matikainen, A.; Nuutinen, T.; Itkonen, T.; Heinilehto, S.; Puustinen, J.; Hiltunen, J.; Lappalainen, J.; Karioja, P.; Vahimaa, P. Atmospheric Oxidation and Carbon Contamination of Silver and Its Effect on Surface-Enhanced Raman Spectroscopy (SERS). *Scientific Reports 2016 6:1* **2016**, *6* (1), 1–6. https://doi.org/10.1038/srep37192.

(262) Qiu, J.; Tang, J.; Shen, J.; Wu, C.; Qian, M.; He, Z.; Chen, J.; Shuang, S. Preparation of a Silver Electrode with a Three-Dimensional Surface and Its Performance in the Electrochemical Reduction of Carbon Dioxide. *Electrochim Acta* **2016**, *203*, 99–108. https://doi.org/10.1016/J.ELECTACTA.2016.03.182.

(263) Soto, Á. M.; German, S. R.; Ren, H.; van der Meer, D.; Lohse, D.; Edwards, M. A.; White, H. S. The Nucleation Rate of Single O2 Nanobubbles at Pt Nanoelectrodes. *Langmuir* **2018**, *34* (25), 7309–7318. https://doi.org/10.1021/ACS.LANGMUIR.8B01372/ASSET/IMAGES/LARGE/LA-2018-01372F_0011.JPEG.

(264) Katsounaros, I.; Schneider, W. B.; Meier, J. C.; Benedikt, U.; Biedermann, P. U.; Auer, A. A.; Mayrhofer, K. J. J. Hydrogen Peroxide Electrochemistry on Platinum: Towards Understanding the Oxygen Reduction Reaction Mechanism. *Physical Chemistry Chemical Physics* **2012**, *14* (20), 7384–7391. https://doi.org/10.1039/C2CP40616K.

(265) Burke, L. D.; Nugent, P. F. The Electrochemistry of Gold: I the Redox Behaviour of the Metal in Aqueous Media. *Gold Bulletin 1997 30:2* **1997**, *30* (2), 43–53. https://doi.org/10.1007/BF03214756.

(266) Burke, L. D.; Nugent, P. F. The Electrochemistry of Gold: II the Electrocatalytic Behaviour of the Metal in Aqueous Media. *Gold Bulletin 1998 31:2* **1998**, *31* (2), 39–50. https://doi.org/10.1007/BF03214760.